898

A STUDY ON DUCTILE FRACTURE

A STUDY ON DUCTILE FRACTURE

PROEFSCHRIFT

TER VERKRIJGING VAN DE GRAAD VAN DOCTOR IN DE
TECHNISCHE WETENSCHAPPEN AAN DE TECHNISCHE HOGESCHOOL DELFT,
OP GEZAG VAN DE RECTOR MAGNIFICUS IR. H.R. VAN NAUTA LEMKE,
HOOGLERAAR IN DE AFDELING DER ELEKTROTECHNIEK,
VOOR EEN COMMISSIE UIT DE SENAAT
TE VERDEDIGEN OP
WOENSDAG 10 FEBRUARI 1971 TE 14 UUR

door

DAVID BROEK

VLIEGTUIGBOUWKUNDIG INGENIEUR
GEBOREN TE KAMPEN

NEDERLANDSE BOEKDRUK INDUSTRIE N.V., – 'S-HERTOGENBOSCH

DIT PROEFSCHRIFT IS GOEDGEKEURD
DOOR DE PROMOTOR
PROF. IR. P. JONGENBURGER

Aan mijn ouders
Aan Marga
Aan Titus, Marieke en Ilse

De schrijver betuigt gaarne zijn dank aan de directie van het Nationaal Lucht- en Ruimtevaartlaboratorium voor de hem verleende vrijheid, de resultaten van hem opgedragen onderzoekingen te rapporteren in dit proefschrift.

SUMMARY

Electron microscopical examination of fracture surfaces and micro-structure of thirteen different aluminium alloys revealed that ductile rupture is initiated at small inclusions. The average dimple spacing is equal to the average inclusion distance.

Void initiation is probably the critical event in ductile fracture; it is immediately followed by spontaneous growth and coalescence of the voids. A dislocation model is developed compatible with this point of view. Evaluation of this dislocation model yields a relation between the fracture strain and the volume fraction of the inclusions. The analysis also leads to a relation between the fracture toughness and the structural parameters.

CONTENTS

LIST OF SYMBOLS

Note: a few symbols have a double meaning because it was considered desirable to comply with the nomenclature generally used in the literature; e.g. γ is used for surface energy and for shear strain. Where this occurs sufficient notice is given in order to avoid confusion.

Several symbols are used only once in the text, where their meaning is explained; such symbols are not encountered in the present list.

The parameters σ and τ are used with a variety of indices. Indices with a trivial meaning are not presented in the list of symbols.

a	diameter of spherical inclusion, hole diameter
A	area; sectional area
A_o	original cross section
A_n	cross section at onset of necking
A_f	cross section in necked area after fracture
$\boldsymbol{b}$	Burgers vector
c_o	crack opening displacement
C	constant (used in various equations)
d	dimple size
d^*	apparent dimple size
E	modulus of elasticity
E_i	modulus of inclusion material
E_m	modulus of matrix material
f	volume fraction of particles
k_ε	strain concentration factor
K	stress intensity factor
K_{Ic}	fracture toughness
l	half-crack length
L	dislocation pile-up length
m	strain hardening exponent
n	number of dislocations in a pile-up
N_a	number of particles per unit area
N_l	number of particles per unit length
N_v	number of particles per unit volume
p	dimple depth
p^*	apparent dimple depth
r	polar coordinate, radius of cylindrical inclusion
s	inclusion spacing, hole spacing

t	time
u	displacement
V	volume
α, β	factor, constant, used in various relations
γ	shear strain, surface energy
γ_f	shear strain at fracture
ε	strain
ε_f	true fracture strain
λ	particle length, distance between dislocation and center of particle
μ	shear modulus
μ_m	modulus of matrix material
μ_p	modulus of material of particle
ν	Poisson's ratio
ν_m, ν_p	Poisson's ratio for matrix and particle
σ_0	flow stress at $\varepsilon = 1$
$\sigma_{0.2}$	0.2% off-set yield stress
σ_a	applied stress
σ_f	true fracture stress
σ_n	nett section stress
σ_u	ultimate tensile strength
σ_y	yield stress
τ	shear stress
τ_a	applied shear stress
τ_i	lattice friction stress
τ_0	flow stress at $\gamma = 1$

“This field of study is at present one of the weakest in metallurgy”.

D. McLean (1962).

CHAPTER 2

RELEVANCE AND SCOPE OF THE PRESENT WORK

The primary aim of the present investigation was to supply factual support to the incomplete picture of ductile fracture. Ductile fracture is the result of initiation, growth and coalescence of microvoids. The evidence already available (chapter 1) suggests that the so called voids observed under the optical microscope are cracks rather than microvoids. Since dimples generally have a size of the order of a micron, particles responsible for void initiation must be in the order of a tenth of a micron. With this relationship in mind it was tried to obtain answers to the following questions:

(a) Can the initiation of voids be observed in common aluminium alloys; does it occur by particle failure or interface failure?
(b) Does a direct correlation exist between dimples and particles; in other words is the average dimple size equal to the average particle spacing?
(c) How does void initiation depend on stress and strain and on particle size, shape and composition?

On the basis of the evidence obtained it was tried to:

(d) Obtain a phenomenological picture of void initiation, growth and coalescence.
(e) Construct a physical model for void growth and coalescence, compatible with the observations.
(f) Establish criteria for void initiation and coalescence.

This scope is broad and decisive answers on all these questions cannot be expected. Yet, conclusive evidence was obtained on items (a) and (b). As far as item (c) is concerned some trends can certainly be established from the present work. Some ideas on void growth and coalescence [item (d)] emerge from the stereoscopic measurements. A model of void growth and coalescence could be constructed [item (e)], but only speculative results concerning item (f) were obtained.

Generally speaking, some new light was shed on the problem of ductile fracture. It will be tried to ascertain whether the new evidence can be of help in solving such problems as ductility and fracture toughness. Finally an inventory will be made of pertinent questions which need an answer before the problem of ductile fracture is brought to a preliminary solution.

CHAPTER 3

SURVEY OF EXPERIMENTS

In this chapter a concise summary will be given of the experiments carried out during this investigation. Ample information on experimental techniques is presented in the appendix (Chapter 10).

In the first part of the study the fracture surfaces and structures of thirteen different aluminium alloys were studied. Four materials were of the Al–Zn–Mg type, namely three 7075 materials of different manufacturers and a 7079 alloy. Five materials were of the Al–Cu–Mg type, namely three commercial 2024 alloys of different producers, one 2014 alloy, one experimental 2024 alloy with an extra low content of secondary alloying elements and one Al–Cu alloy with small additions of lead and bismuth, which will be denoted henceforth by 2024 (Pb, Bi). One Al–Mn alloy was chosen and two Al–Mg–Si (a 6061 and a 6151 type) alloys. Finally some observations were also made on a dispersion strengthened material, namely the Al-Al_2O_3 alloy SAP 895. Most materials were in sheet form, except for the 7079, which was a forging, the 6061, the 2024 (Pb, Bi) and the SAP 895, which were extruded bars and one 2024 and one 7075 alloy, which were thick plates. The chemical composition of all materials was determined by X-ray spectrometry. Information on chemical composition and mechanical properties is presented in Table 1.

Normal size tensile specimens were made of all materials, with the exception of the clean 2024 alloy, where lack of sufficient material necessitated a smaller specimen size. Extensive electron fractography was carried out on two stage carbon replicas of the fracture surfaces. Thin foils of all materials were made for transmission electron microscopy. A correlation between average inclusion distance and average dimple size was determined; for this purpose counts of some 10.000 voids and some 10.000 inclusions were made from about 200 electron micrographs.

Further study of void development and coalescence was carried out by making stereoscopic measurements to determine dimple profiles. Dimple profiles were also studied directly by examining cross sections of fracture surface replicas in the electron microscope. These cross sections were prepared by the technique developed by Broek and Bowles [10] which is amplified in the appendix (sect. 10.2). Finally it was considered necessary to get an idea of how the two halves of a dimple match. For this purpose

TABLE 1. Materials

Material	Condition	Chemical composition (wt. % determined by X-ray spectrometry)											Mechanical properties		
		Cu	Zn	Mg	Mn	Si	Fe	Ti	Cr	Pb	Bi	Al_2O_3	ultimate tensile stength σ_u (kg/mm^2)	0.2% yield strength $\sigma_{0.2}$ (kg/mm^2)	elongation % on 50 mm gauge length
2014	quenched and aged	4.25	0.13	0.84	0.79	0.42	0.45	0.03	0.06	–	–	–	47.9	43.2	10
2024(PbBi)	quenched and aged	5.25	0.09	–	–	0.22	0.22	–	0.02	0.5*	0.5*	–	37.4	30.5	15
2024(Clean)	quenched and aged	4.35	0.01	1.50	0.54	0.17	–	–	–	–	–	–	43.3	29.8	18
2024(1)	quenched and aged	4.30	0.13	1.50	0.61	0.18	0.32	–	–	–	–	–	48.5	37.1	–
2024(2)	quenched and aged	4.45	0.13	1.54	0.66	–	0.28	0.03	0.03	–	–	–	43.3	29.8	18
2024(3)	quenched and aged	4.52	–	1.58	0.53	0.02	0.26	–	0.03	–	–	–	49.3	36.0	18
3003	cold rolled	0.20	0.05	–	1.21	0.26	0.63	0.01	0.01	–	–	–	16.5	15.5	5
6061	quenched and aged	0.35	0.07	0.76	0.13	0.30	0.36	0.01	0.24	–	–	–	26.1	17.8	19
6151	quenched and aged	0.12	–	0.52	–	0.77	0.25	–	–	–	–	–	30.9	26.8	21
7075(1)	quenched and aged	1.48	5.30	3.10	0.11	0.06	0.27	–	0.20	–	–	–	54.7	50.0	–
7075(2)	annealed	1.70	5.43	2.02	0.10	–	0.26	0.03	0.19	–	–	–	21.1	9.3	15
7075(3)	quenched and aged	1.37	5.33	2.64	0.07	–	0.27	–	0.19	–	–	–	56.4	50.9	12
7079	quenched, not aged	0.67	4.60	3.37	0.17	0.17	0.22	0.05	0.19	–	–	–	47.6	29.8	–
SAP 895	as extruded	–	–	–	–	–	0.3	–	–	–	–	8–10*	32.6	21.0	12

* According to producer.

stereo picures had to be made of precisely matching points of the two opposing fracture surfaces. After many failures this was finally accomplished in the way described in the appendix (sect. 10.3). In order to obtain some extra information a number of fracture surfaces were examined also in a scanning electron microscope. This work led to a phenomenological picture of void growth and coalescence.

The study of void initiation was started with testing small tensile specimens (3 mm width, 25 mm length) in a special tensile device that could be manipulated under the optical microscope. This technique allowed the observation of nucleation and development of voids at large inclusions (10 microns and larger). Subsequently, thin foil micro-specimens were pulled in the straining device of the electron microscope allowing fracture to be observed directly in the microscope. The objective was to study the development of voids at the small inclusions (500–2000 Ångstrøms). However, the method proved unsuccessful, because the fracture process of foils as thin as 1000–1500 Ångstrøms is not governed by void initiation, as will be shown later.

It was finally found that void formation at these small inclusions could be observed in some cases in thin foils prepared from normal tensile specimens. The specimens were pulled to a predetermined strain (different for each specimen) and then thin foils for transmission electron microscopy were made from these specimens. In this way voids initiated by interface decohesion and by particle failures could be observed.

Supplementary testing with special tensile specimens of brass sheet was done to illustrate certain results. These specimens, containing up to 50 randomly distributed holes, are discussed in detail in the appendix (sect. 10.7).

CHAPTER 4

EXPERIMENTAL RESULTS

In order to facilitate comprehension, only a limited survey of experimental results will be presented in this chapter, which serves as a basis for the discussion of the fracture mechanism in the following chapters. Detailed experimental results will be presented where they are relevant to the discussion.

The initiation of voids at large particles (of the order of 10 microns) could be observed in the specimens pulled under the optical microscope. Various stages in the process of void growth are shown in fig. 1. The specimens were left unetched in order to avoid misleading observations, since an etched away inclusion or an ordinary etch pit might erroneously be considered as a void. Because the surface was unetched the inclusions are only poorly visible in the early stages of the test. At larger strains they are better delineated because of their relative flatness as compared to the surrounding yielding material (sliplines). When comparing the distance between two particular inclusions (e.g. A and K in fig. 1 in the three successive stages shown) one obtains a good impression of the increasing strain.

Fig. 1 indicates that voids may be initiated already at small strains at the larger particles, as a result of cleavage fracture of these particles. Although in some cases interface failure seems to take place, it should be borne in mind that the inclusions may have fractured such that this separation appears interfacial at the viewing surface. Similar reasoning leads to the conclusion that from experiments like these one can hardly determine a relation between the size of particles and their fracture strain. A further objection is that the tests supply information about inclusions at the surface only. Due to triaxiality of the stress system the inclusion fracture strain may be different in the interior of the specimen.

Nevertheless some interesting observations were made during these experiments. When fracture is still remote and strains are still low, relatively large voids can be initiated as a result of cleavage fracture of the large inclusions. Large cleaved inclusions can also be observed in replicas of the fracture surface as in the examples in fig. 2. The early occurrence of these voids apparently is not essential for the fracture process, although it must be of importance for ductility, because plastic deformation will

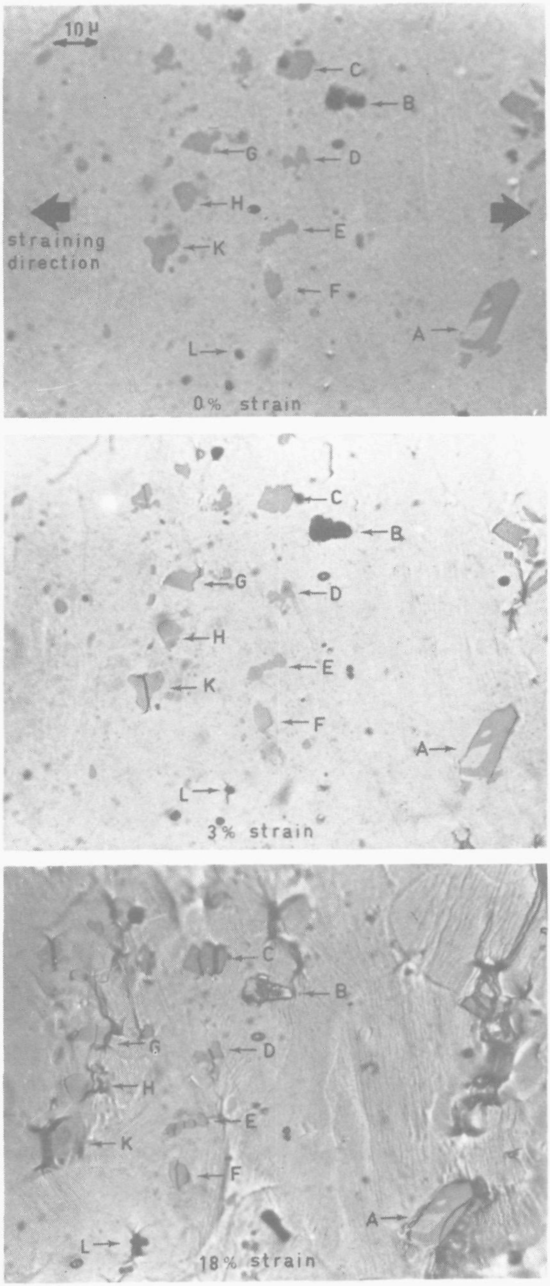

Fig. 1. Void initiation at large particles as observed under the optical microscope (note development at identical points). 2024 T3 material. Direction of tension was horizontal.

concentrate at these voids. Due to this strain concentration the void may grow (fig. 1, K and fig. 2). Also microvoids may later initiate in the vicinity of this highly strained area. Summarizing, one can say that cracking of large inclusions is certainly not the critical event for fracture, but it may affect microvoid initiation in a later stage.

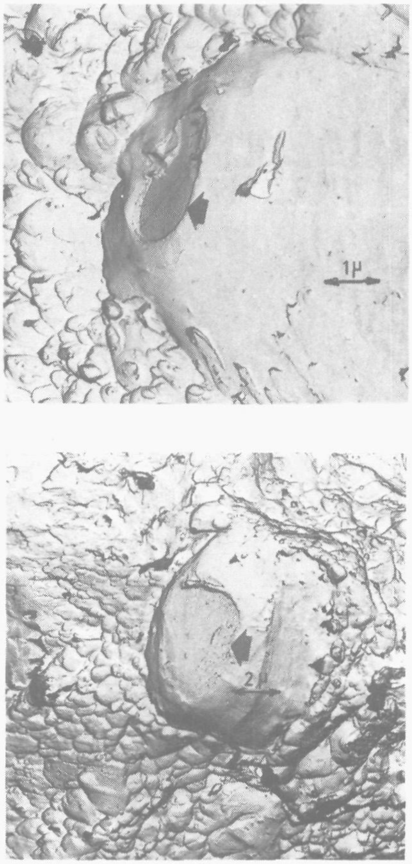

Fig. 2. Cleaved inclusions of large size visible on the fracture surface (solid arrow) which introduced large voids. 2024-T3 material.

As can be observed in fig. 2, many small dimples occur on the fracture surface as well as large voids. Generally the greater part of the fracture surface consists of such small dimples, leading to suspect that the initiation, growth and coalescence of these microvoids is the critical event for ductile fracture. A larger area is shown in fig. 3, where small dents can be observed

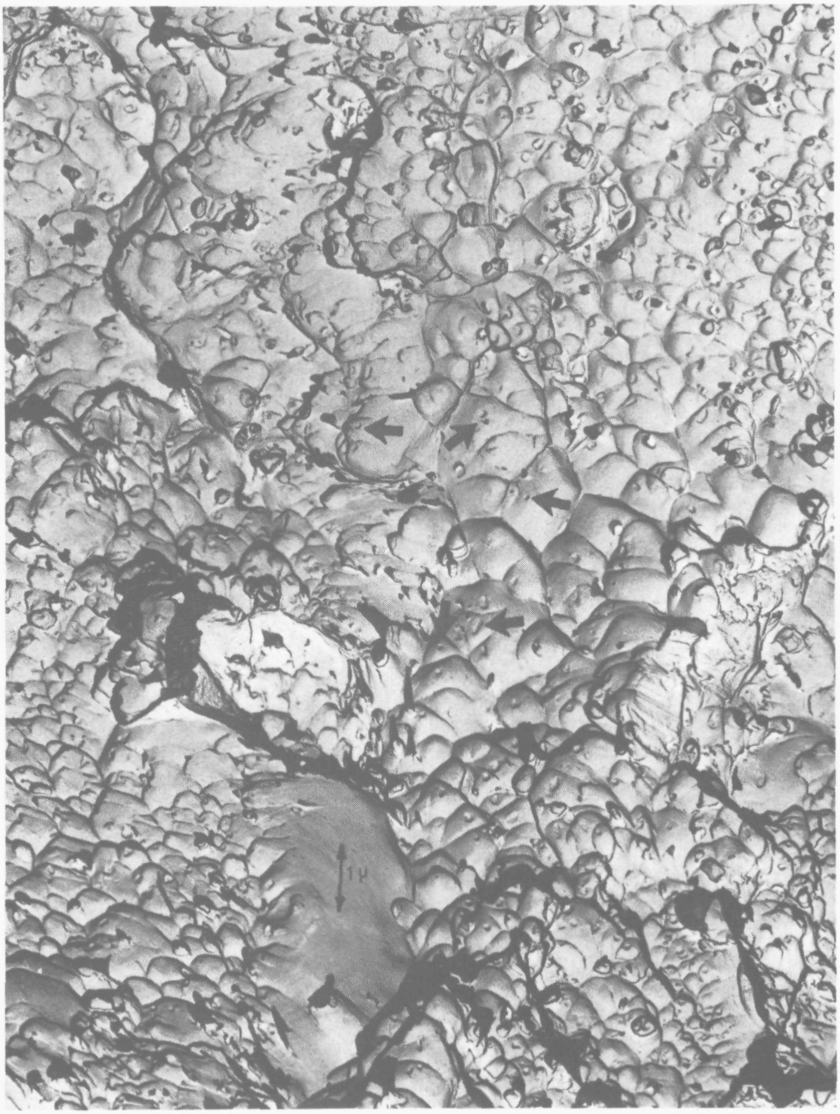

Fig. 3. Fracture surface area with dimples. Imprints of inclusions visible at arrows. Note that dimples have no uniform size. 7075-T6 material.

in many dimples (arrows). These dents are assumed to be small inclusions that initiated the dimples. Examples of such small inclusions are shown in the transmission electron micrographs of fig. 4. If these inclusions initiated the small dimples, then the dimple size should equal the spacing

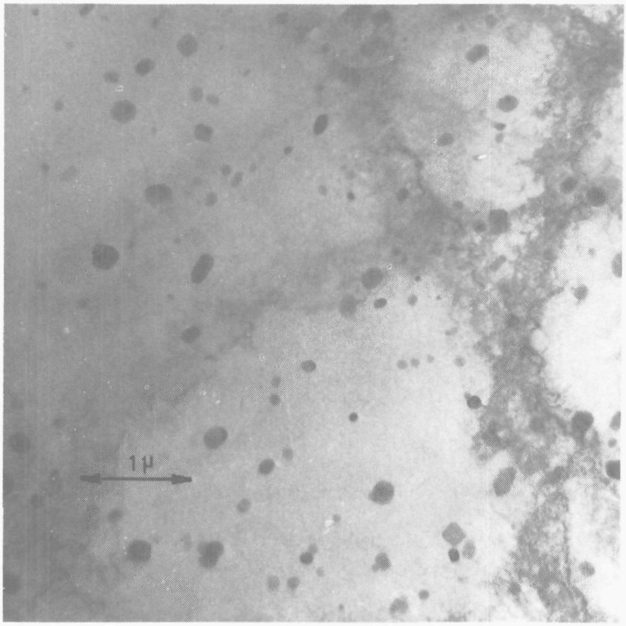

(a) More or less spherical inclusions in 6061 material.

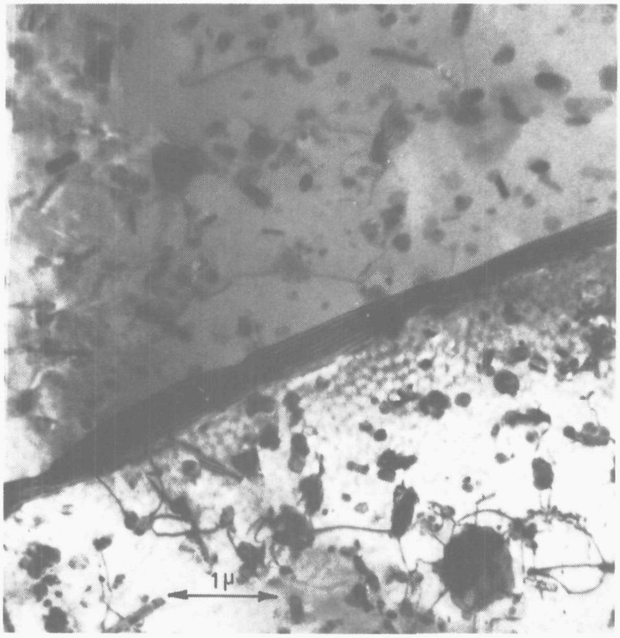

(b) Inclusions of various shapes in 7075 material.

of this type of inclusions. It is readily seen from fig. 3 that the dimple size is by no means uniform, nor is the inclusion distribution (fig. 4). Hence, a proof of the expected correlation between dimple size and inclusion distance can only be obtained from counts of large numbers of these features. Since an automatic counting device to be used in combination with an electron microscope is not yet available, the counts had to be made by visual inspection of micrographs.

In order to have some confidence in the results the correlation should be checked for a sufficiently large number of different materials. In this

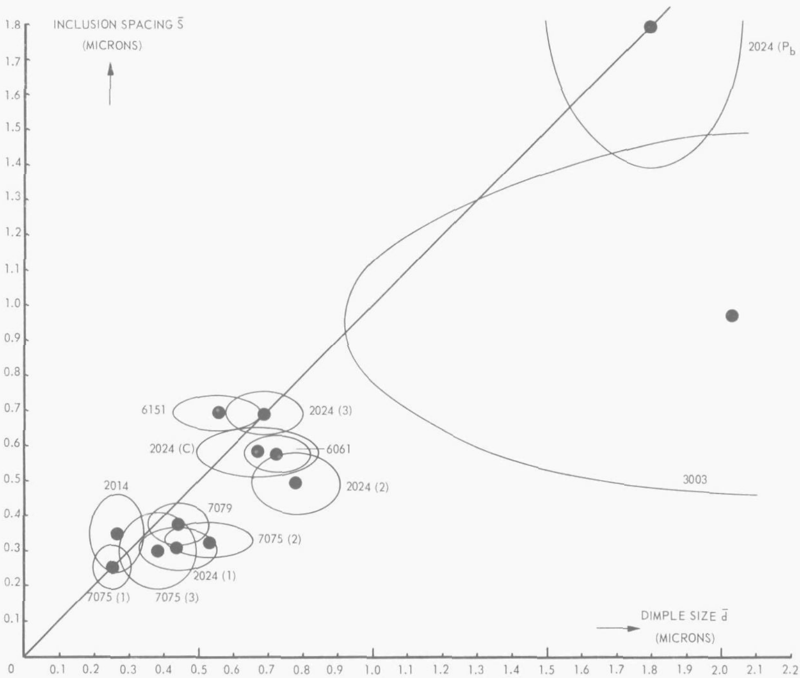

Fig. 5. Measured relation between dimple size and inclusion spacing. (Scatter indicated, see text)

case 13 different aluminium alloys were used. For each material the average size of about 1000 dimples and the average spacing of about 1000 inclusions were measured. Magnifications in the microscope were adjusted to give about 100 dimples or inclusions in one micrograph. Thus over 200 micrographs were required for the thirteen materials. The measuring procedure is briefly described in the appendix (sect. 10.9).

The average dimple size as measured from the fractographs is plotted *versus* the average inclusion spacing in fig. 5. These averages were obtained by taking the mean of the results of all photographs (the result obtained from each photograph is in itself already an average value). The haloes around the data points indicate the standard deviation in the results of the various photographs; hence they do not give the real standard deviations of dimple size and inclusion spacing.

The straight line drawn in fig. 5 indicates the theoretical one–to–one relationship between dimple size and the spacing of the small inclusions considered here. It is felt that the data points are close enough to this line to conclude that these small inclusions are indeed responsible for void initiation and fracture. The trend in fig. 4 is that the dimple size is generally slightly larger than the inclusion spacing. Such a discrepancy might be expected if void initiation does not take place from every inclusion.

After having indirectly established which type of inclusion was responsible for ductile fracture, the next step was to try to give direct evidence of void initiation at small inclusions. Thin foils made from the area very close to the fracture surface of tensile specimens did indeed reveal some voids. It has been reported [7, 8, 9] that at more or less

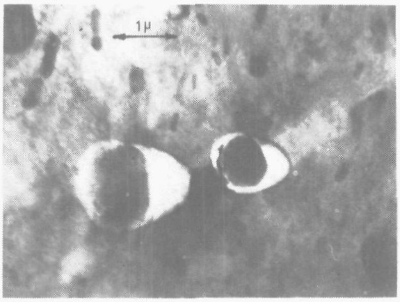

(a) 2024 material.

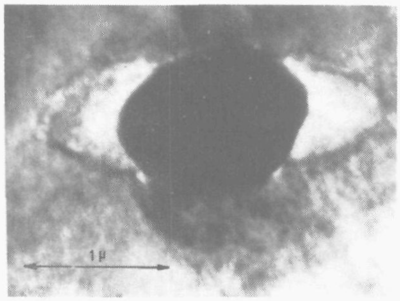

(b) 2024 material.

Fig. 6. Voids initiated at particle-matrix interface. Stress direction unknown.

spherical inclusions void formation often occurs as a result of decohesion of the matrix particle interface in particular for oxide particles. In the present study void formation at the matrix-particle interface was found only occasionally. Examples of such voids are presented in fig. 6.

In two materials void initiation occurred by fracture of the elongated particles. This phenomenon is illustrated in fig. 7, which shows only a single example of decohesion at the interface. However, it cannot be stated that void formation in materials with elongated particles will be caused primarily by particle failure. This can be appreciated from fig. 8, where in a 2024 material with mainly elongated particles many voids have occurred at the interface.

The voids shown in figs 6, 7 and 8 occurred close to the fracture surface. Since it was not known where final perforation took place during prepara-

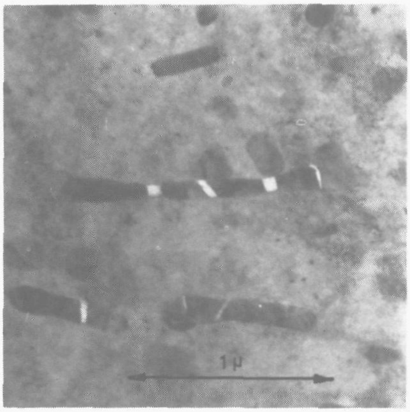

(a) 7079.

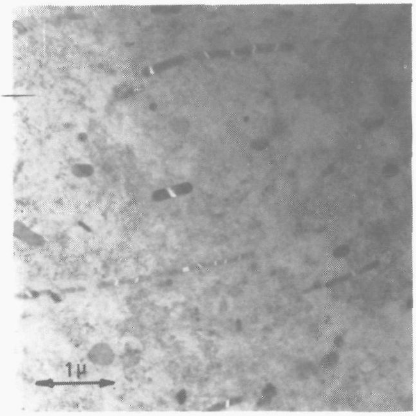

(b) 7079.

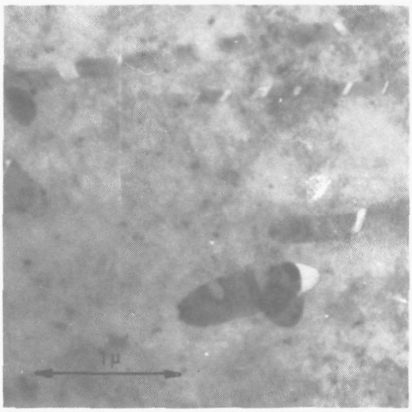

(c) 7079.

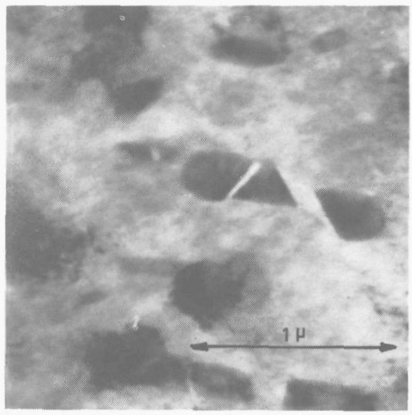

(d) Shear deformation after particle failure.

Fig. 7. Void formation by particle failure (Note interface decohesion in (c)). Stress probably in length direction of particles.

tion of the foils (i.e. the location of the electron-transmitting part), the distance from the fracture surface is unknown, and so is the strain. Since it would be interesting to know how fracture of particles and interface decohesion depends upon strain and particle size, some specimens were subjected to a predetermined high strain, either by bending or by pulling them in a very hard tensile machine and stopping the machine as late as possible during necking. Neither procedure enabled a dependence to be determined: in some specimens many voids were observed, but in others isolated voids or no voids at all were found, even at higher strains.

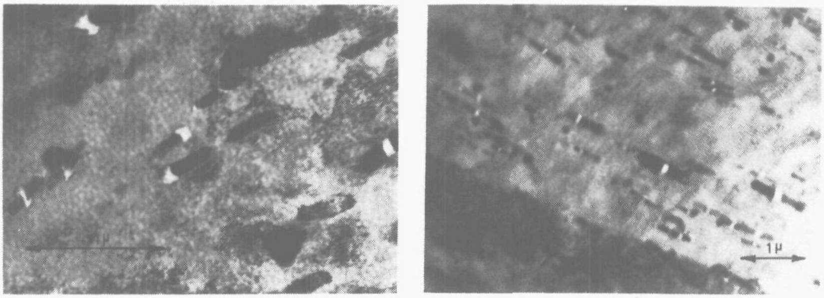

(a) 2024. Decohesion at interface. (b) 2024. Particle failure.

Fig. 8. Void initiation by particle failure and interface decohesion in the same material. Stress probably in length direction of particles.

An impression of the process of void growth and coalescence can be obtained from the study of dimple profiles. The cross sections of the replicas give a good idea of the topography of the fracture surface. This is illustrated in fig. 9a, which gives many examples at various magnifications. Generally the cut will not go through the middle of a particular dimple. However, if it is assumed that the dimples are hemispheres the dimple size d^* in the cross sections is simply related to the actual average dimple size d by the expression

$$d = \frac{\pi}{4} d^* \tag{1}$$

which is derived in the appendix (sect. 10.2). Similarly, the relation between the average dimple depth p^* in the cross section is related to the actual average dimple depth p by

$$p = \frac{\pi}{4} p^* . \tag{2}$$

Combining equations (1) and (2) shows that the depth to width ratio of the dimples can be derived from

$$\frac{p}{d} = \frac{p^*}{d^*} \tag{3}$$

i.e. the actual depth to width ratio is equal to the apparent depth to width ratio in the cross sections. Thus it is possible to assert from fig. 9a that the depth to width ratio is low and that dimples are relatively shallow holes. This is confirmed by stereographic measurements of dimple topo-

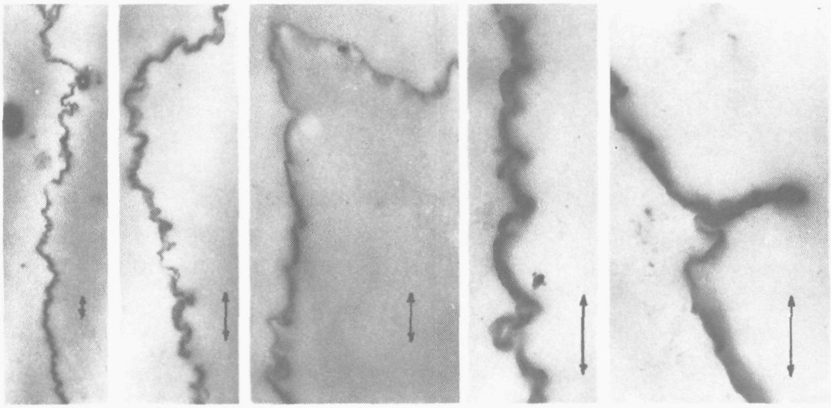

(a) Cross sections of replicas at various magnifications. 7079 material
Length arrows indicate 1 micron.

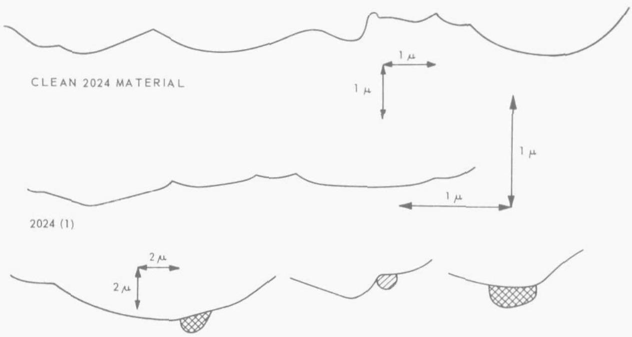

(b) Dimple topography following from stereographic measurents.

Fig. 9. Dimple profiles.

graphies which are presented in fig. 9b. Of course the picture of dimple topography is stilll incomplete until both halves of the voids can be examined. This can be done from stereographic measurements of precisely matching areas of the fracture surface. Fractographs of matching areas are presented in figs 10a and b, while fig. 10c shows the cross section along

The criterion for cavity formation proposed by Gurland and Plateau is that the strain energy relief due to void formation must be sufficient to produce the required surface energy to create the new free surfaces. On the assumptions made the result is

$$\frac{(\alpha\sigma)^2}{E}\,a^3 = \gamma a^2$$

or (4)

$$\sigma_{\text{void}} = \frac{1}{\alpha}\left(\frac{E\gamma}{a}\right)^{\frac{1}{2}}.$$

In this equation σ is the stress in the matrix (nominal stress), γ is the surface energy and α is a factor taking into account the stress concentrations around the particle. According to eq. (4) the stress for cavity formation is inversely proportional to the square root of the particle diameter. This is a direct result of the assumed relation between void size and strained volume.

Rosenfield [3] has pointed out that the value of γ in eq. (4) will depend upon the surface energy of the matrix (γ_m), the surface energy of the particle (γ_p) and the interface energy (γ_{mp}), such that the following conditions hold

$$\begin{aligned} &\gamma = \gamma_m + \gamma_p - \gamma_{mp} && \text{for interface decohesion} \\ &\gamma = 2\gamma_p && \text{for particle fracture} \end{aligned} \tag{5}$$

In an elastic matrix of stiffness μ_m and Poisson's ratio ν_m under tensile load, the stress at the pole of a particle of stiffness μ_p and Poisson's ratio ν_p is, according to Goodier [11]

$$\sigma_{\text{pole}} = (1 + W - QR)$$

with

$$W = \frac{\left[(1-\nu_m)\dfrac{1+\nu_p}{1+\nu_m} - \nu_m\right] - (1-2\nu_p)\rho}{4(1-2\nu_p)\rho + 2(1+\nu_p)};$$

$$Q = \frac{\rho - 1}{2(7-5\nu_m)\rho + (8-10\nu_m)} \tag{6}$$

$$P = \frac{2(1-2\nu_p)(7-5\nu_m)\rho + (4+20\nu_p+\nu_m\nu_p)}{2(1-2\nu_p)\rho + (1+\nu_p)}; \quad \rho = \mu_m/\mu_p.$$

Similar expressions exist for the general equation for stresses around the particle. Eqs (6) show that the stress concentration is

$$k_{\text{pole}} = 1 + W - QP = f(\rho, \nu_p, \nu_m)\,. \tag{7}$$

According to eq. (7) the factor α in eq. (4) depends in a very complicated way upon the elastic constants of the particle and the matrix.

Ashby [13] has proposed a mechanism and criterion specifically for cavity formation at the interface between the matrix and a spherical inclusion in a shear band. In Ashby's model, which was developed especially to explain strain hardening properties of dispersion strengthened materials, plastic deformation of the matrix is essential, but the particle is

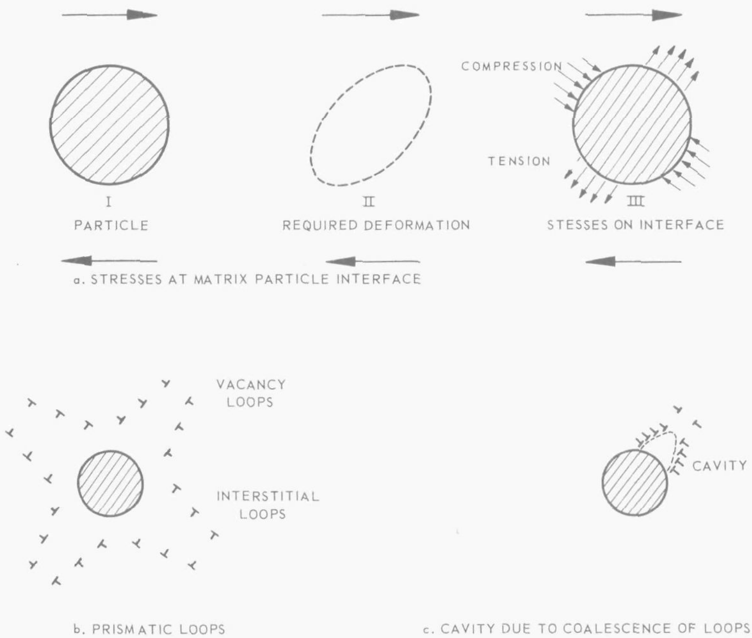

Fig. 11. Void initiation according to Ashby.

considered to be of infinite stiffness. Due to its presence in a shear band the particle will exert stresses on the surrounding matrix, because deformation of the hole will be constrained by the particle. This is shown diagrammatically in fig. 11a.

The stresses exerted by the particle ultimately become so high that they exceed the yield stress. Ashby considers the plastic flow induced by these secondary stresses to be secondary slip, which tries to relieve the stresses exerted by the particle. This can be accomplished by the mechanism proposed by Ashby: condensed-vacancy loops are punched into the matrix in the area of compressive stresses, and interstitial loops are punched into the matrix in the area of tensile stresses, as illustrated in fig. 11b. Ultimately vacancy loops can coalesce at the matrix-particle interface, thus introducing a cavity or void (fig. 11c). In his quantitative analysis Ashby assumed that the strain varied linearly through the shear band, the number n of punched out loops being

$$n = \alpha \frac{\varepsilon a}{\boldsymbol{b}} \tag{8}$$

where ε is the matrix strain, a the particle size, $\boldsymbol{b}$ the Burgers vector and α some constant. The stress exerted on the interface is given by

$$\sigma = \beta \frac{n}{L} \tag{9}$$

where L is the pile-up size and β is another constant.

Cavitation will occur if the stress on the interface exceeds a critical value σ_v: hence, from eqs (8) and (9)

$$\sigma = \frac{\beta n}{k} = \alpha\beta \frac{\varepsilon a}{\boldsymbol{b}L} = \sigma_{\mathrm{void}} \, .$$

Thus a void will be initiated if the matrix strain is

$$\varepsilon_{\mathrm{void}} = \frac{1}{\alpha\beta} \frac{\boldsymbol{b}L}{a} \sigma_v \, . \tag{10}$$

Eq. (10) predicts the strain for void initiations to vary inversely with a, whereas eq. (4) predicted a variation with $a^{-\frac{1}{2}}$. However, this discrepancy might be due to a dependence of L upon particle size.

An objection to the mechanism of Ashby is that it requires slip by prismatic loops, which are essentially sessile. As it requires a high stress to move a prismatic loop in its glide cylinder it may be expected that the first vacancy loop formed, will stick to the interface and create the required void. If really prismatic loops are punched out, they should be visible in electron micrographs. Indeed, prismatic loops are sometimes observed in quenched material: although these are generally considered to be the consequence of vacancy condensation, Barnes and Mazey [14] attribute pile-up groups of prismatic loops in quenched copper, to stresses exerted by precipitates during their growth. However, prismatic loops are not usually observed in deformed metals.

A slight modification of Ashby's model can be applied to aluminium alloys with high stacking fault energy if based on cross slip. Consider an edge dislocation moving against a particle as in fig. 12a. After its passage a loop will be left around the particle. Now the screw parts of the loop may cross slip out of their slip plane, as proposed by Hirsch [15] and Ashby [16]. A comparable model has been developed by Gleiter [17] under the assumption that the inclusion can be represented solely by a stress field through which the dislocation can pass in principle. This model is thought to be irrelevant for the present case. After cross slip has occurred slip may be resumed in a primary slip plane, in which case the screw parts will

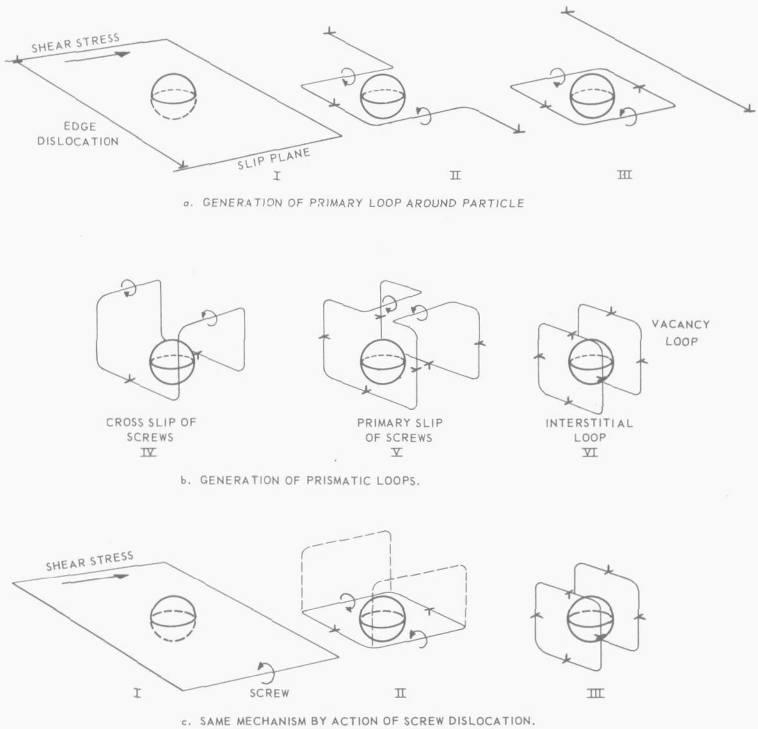

Fig. 12. Generation of vacancy loops at particles.

attract and annihilate each other. The result is the generation of two prismatic loops (fig. 12b). This result is also obtained if a screw dislocation moves in the slip plane according to the procedure in fig. 12c. One of the prismatic loops is a vacancy loop, which is able to initiate a cavity.

The event in fig. 12b will probably not occur until a number of loops of the type in fig. 12a are formed. The strain fields of these loops will overlap and include that of the particle. Loops of this type will probably not be visible in the electron microscope because the greater portions of them will be etched away during foil preparation. When the strain on the inner loop is high enough the cross slip mechanism of fig. 12b may occur. The stress field of surrounding glissile loops will push the generated vacancy loop to the interface, where it generates the void.

5.3 *Void initiation at elongated particles*

The condition for cavity formation as proposed by Gurland and Plateau [12] may also be applied to elongated particles. The energy equation will then take the form

$$\frac{q\sigma^2}{E}\,a^2\lambda = \gamma a^2$$

and eq. (4) becomes

$$\sigma_{\text{void}} = \frac{1}{q}\left(\frac{E\gamma}{\lambda}\right)^{\frac{1}{2}} \tag{11}$$

where λ is the particle length and a its diameter.

According to eq. (11) the stress for void initiation would not depend on the length to width ratio of the particle, but solely on the length.

Generally it is assumed that fracture of a particle is caused by cleavage as a result of stresses exerted by dislocations piling-up against the particles. An indirect proof for this is given in fig. 7d, which shows shear deformation after particle failure. This shear may be due to the release of a

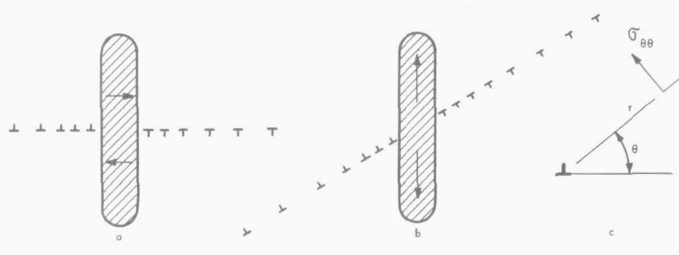

Fig. 13. Fracture of elongated particle due to stresses exerted by pile-up.

dislocation pile-up. An analysis of particle fracture by the shear stress from a pile-up group (fig. 13a) has been presented by Gurland [18]. This analysis may also be obtained from a treatment by Barnby [19]. Near the head of a pile-up of n dislocations the group exerts in its glideplane a shear stress

$$\tau = n\tau_a$$

where τ_a is the applied shear stress. The number of dislocation in the pile-up can be given approximately by

$$n \simeq \frac{2L}{\mu \boldsymbol{b}} \tau_a$$

where L is the length of the pile-up. Then it follows that the shear stress exerted on the particle is

$$\tau = \frac{2L}{\mu \boldsymbol{b}} \tau_a^2 .$$

If the inclusion fractures when this stress exceeds the critical value τ_{cr}, the condition for void initiation is

$$\tau_a = \left(\frac{\mu \boldsymbol{b} \tau_{cr}}{2L}\right)^{\frac{1}{2}} . \qquad (12)$$

The stress τ_a in eq. (12) is independent of particle size. Barnby claims that the fracture stress τ_{cr} of the inclusion varies as the square root of the particle diameter, which would imply that small particles would fail at lower stresses than large particles: this is not realistic. Gurland introduces particle size in eq. (12) by proposing that there is a relation between the pile-up size and the particle dimensions and spacing. A variation of eq. (12) can be obtained by assuming that $n \simeq C\varepsilon/\boldsymbol{b}$. Then

$$\tau = \frac{C\varepsilon}{\boldsymbol{b}} \tau_a = \tau_{cr} . \qquad (13)$$

It seems more realistic to consider that cleavage failure of a particle occurs as a result of tensile stresses rather than by shear. A dislocation pile-up could exert tensile stresses on the particle if the plane of the pile-up were inclined to the axis of the particle as in fig. 13 b, c. This would lead to an equation similar to eq. (13), with the geometrical parameter θ incorporated in C.

In most cases the observations of cleaved inclusions mentioned in the literature concern non-metallic inclusions of a size visible in the optical microscope. Some examples are: MnS inclusions in steel [20], carbides in steel [21], carbides in stainless steel [19], sulphides [22, 23], and hydrides in zircaloy [24]. Examples in the present work are shown in figs 1 and 2.

However, the present study is concerned with very small inclusions of a metallic nature. They are believed to be complicated intermetallic compounds of alloying elements such as iron, manganese, copper, magnesium and zinc. Cleavage fracture in these constituents cannot be excluded; but these metallic compounds must have a reasonable ductility. An indirect proof for this statement is the fact that many particles of the type as in figs 7 and 8 did not crack until subjected to strains of the order of 25 %. If the particles have sufficient length they will undergo the same strain as the matrix. An elastic strain of 25 % would require stresses of $E/4$, which is of the order of the theoretical strength. Although particles as in figs 7 and 8 resemble whiskers, with inherent high strength, it must be assumed that

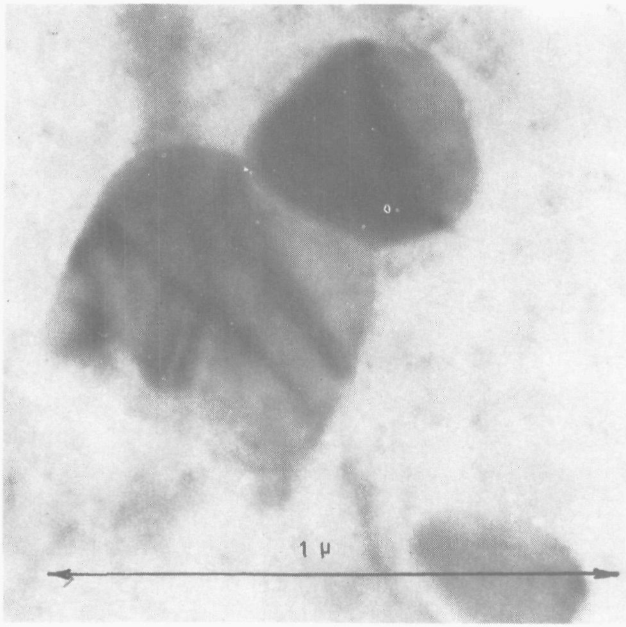

Fig. 14. Contrast in particles, which may be due to dislocations. 7075 material.

the particles undergo some plastic deformation. A direct proof of this cannot be presented, although the contrast in the inclusion in fig. 14 could be due to deformations. The occurrence of plastic deformation in non-metallic inclusions, such as sulphides [24] and cementite [25] suggests that plastic deformation in metallic particles must be a possibility.

Based on the foregoing discussion, another criterion can be proposed for the fracture of inclusions. It is suggested that the particles undergo plastic deformation in tension during straining of the matrix until the ductility of the inclusion is exhausted and fracture results. When the inclusions have higher stiffness than the matrix the same deformation will require higher stresses in the particles than in the matrix. Due to this stress concentrating effect the particles might fail at relatively low strains. Unfortunately, an elastic-plastic treatment of this problem will be difficult, and is premature as long as our knowledge of ductile fracture is so limited. From elastic considerations, however, a reasonable idea can be obtained of the consequences of the assumptions: if the modulus of an elongated particle is twice that of the matrix the stresses in the particle will reach values about twice as high as the matrix stresses; in an equiaxed particle the stress will not reach this ultimate value. The conclusion is that the fracture stress must depend upon the length to thickness ratio of the

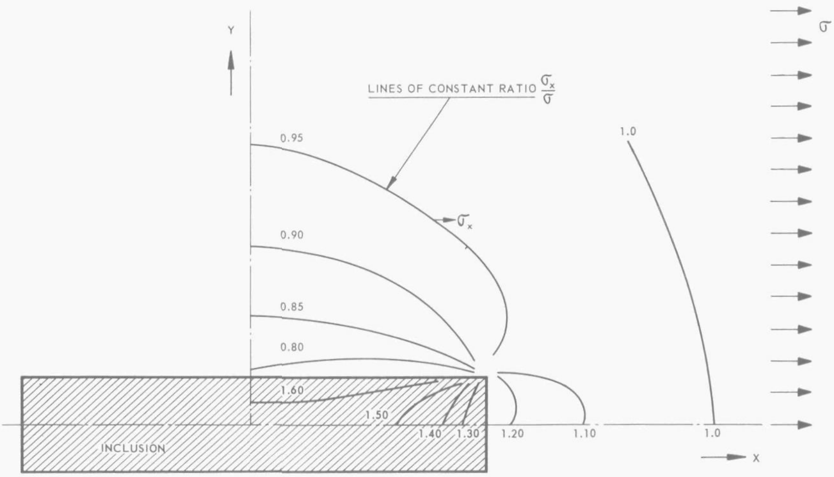

Fig. 15. Stress distribution around elongated (2-dimensional)particle under plane stress as calculated by Ottens* using finite element methods.

inclusion. An approximate elastic treatment of the problem was considered worthwhile and has been carried out in the present investigation as follows.

The stress field around an elongated particle of unit thickness in a sheet of unit thickness was determined approximately from a finite element analysis. The calculation was made for the special case where the ratio between the moduli of the particle and the matrix equals 2 and the particle length to width is 5. The computed stresses have been plotted in fig. 15, which shows that the maximum tensile stress in the particle does indeed approach the value of the ratio E_i/E_m. Further, it can be concluded that the effect of the particle on the stresses in the matrix has vanished at distances of the order of the particle size. On the assumption that this observation

* Private communication.

can be generalized, the problem of an elastic inclusion in an elastic matrix can be treated analytically in a very simple, though approximate, way.

For an element dx of the cylindrical particle in fig. 16 the equilibrium equation can be written as

$$\frac{dN_i}{dx}\,dx = -2\pi r\tau\,dx\,, \tag{14}$$

N_i being the normal force in the inclusion. Also shown in fig. 16 is the derivation that the shear strain γ is: $\gamma=(u_m-u_i)/2r$, where u_m and u_i are

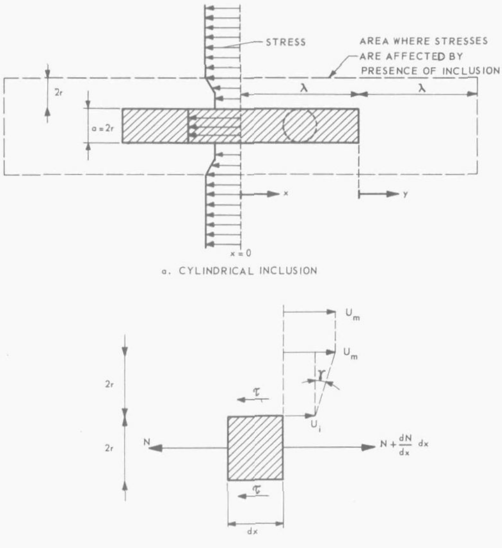

Fig. 16. Elastic cylindrical inclusion in elastic matrix.

the displacements in the matrix and the inclusion respectively. Hence

$$\tau = \mu_m\gamma = \mu_m\,\frac{u_m-u_i}{2r} \tag{15}$$

if μ_m is the shear modulus of the matrix. Eq. (15) gives an approximation for the shear stress at the interface; of course eq. (15) is not valid for the matrix, since the shear stress will decrease gradually in the matrix.

The normal force N_i in the inclusion is given by

$$N_i = \pi r^2\sigma_i = \pi r^2\varepsilon_i E_i = \pi r^2 E_i\,\frac{du_i}{dx}\,. \tag{16}$$

Substituting eqs (15) and (16) in eq. (14) yields

$$\pi r^2 E_\mathrm{i} \frac{\mathrm{d}^2 u_\mathrm{i}}{\mathrm{d}x^2} + \frac{u_\mathrm{m} - u_\mathrm{i}}{2r} \cdot 2\pi r \mu_\mathrm{m} = 0 . \tag{17}$$

By noting that $u_\mathrm{m} = \varepsilon_\mathrm{m} x$ and defining

$$\frac{\mu_\mathrm{m}}{E_\mathrm{i} r^2} = \alpha^2 \tag{18}$$

the differential equation (17) reduces to

$$\frac{\mathrm{d}^2 u_\mathrm{i}}{\mathrm{d}x^2} - \alpha^2 u_\mathrm{i} = -\alpha^2 \varepsilon_\mathrm{m} x . \tag{19}$$

Similarly a differential equation for the roll of material in front of the inclusion (fig. 16) can be derived

$$\frac{\mathrm{d}^2 u_\mathrm{r}}{\mathrm{d}y^2} - \beta^2 u_\mathrm{r} = -\beta^2 \varepsilon_\mathrm{m} (y + \lambda) \tag{20}$$

with

$$\frac{\mu_\mathrm{m}}{E_\mathrm{m} r^2} = \beta^2 \tag{21}$$

(the subscript r denotes roll of material in front of inclusion).

Note that

$$\frac{\beta}{\alpha} = \frac{\sqrt{E_\mathrm{i}}}{\sqrt{E_\mathrm{m}}} = q \quad \text{and} \quad \beta = \alpha q . \tag{22}$$

A solution of eqs (19) and (20) by hyperbolic functions is the most attractive:

$$\begin{aligned} u_\mathrm{i} &= A \sinh \alpha x + B \cosh \alpha x + \varepsilon_\mathrm{m} x \\ u_\mathrm{r} &= C \sinh \alpha q y + D \cosh \alpha q y + \varepsilon_\mathrm{m}(y + \lambda) . \end{aligned} \tag{23}$$

The boundary conditions are

$$\begin{aligned} &\text{(a)} \quad u_\mathrm{i} = 0 \ \text{ for } \ x = 0 \ \text{(symmetry)} \\ &\text{(b)} \quad \mathrm{d}u_\mathrm{r}/\mathrm{d}y = \varepsilon_\mathrm{m} \ \text{ for } \ y = \lambda \\ &\text{(c)} \quad u_\mathrm{i} = u_\mathrm{r} \ \text{ for } \ x = \lambda;\ y = 0 \\ &\text{(d)} \quad E_\mathrm{i}\, \mathrm{d}u_\mathrm{i}/\mathrm{d}x = E_\mathrm{m}\, \mathrm{d}u_\mathrm{r}/\mathrm{d}y \ \text{ for } \ x = \lambda;\ y = 0 \end{aligned} \tag{24}$$

Boundary conditions (a) and (b) lead to $B = 0$ and $C = -D \tanh \alpha q \lambda$, and (c) and (d) yield as a final solution

$$u_\mathrm{i} = \varepsilon_\mathrm{m} \left(x + \frac{(E_\mathrm{m} - E_\mathrm{i}) \sinh \alpha x}{\alpha E_\mathrm{i} \cosh \alpha \lambda + \alpha q E_\mathrm{m} \sinh \alpha \lambda \tanh \alpha q \lambda} \right) . \tag{25}$$

The conversion into strains is obtained from $\varepsilon_i = du_i/dx$, giving

$$\varepsilon_i = \varepsilon_m \left[1 - \frac{(E_i - E_m)\cosh \alpha x}{\alpha E_i \cosh \alpha\lambda + \alpha q E_m \sinh x\lambda \tanh \alpha q\lambda}\right]. \tag{26}$$

The maximum strain in the inclusion occurs in its centre at $x=0$, hence

$$\varepsilon_{max} = \varepsilon_m \left(1 - \frac{q^2 - 1}{q^2 \cosh \alpha\lambda + q \sinh \alpha\lambda \tanh \alpha q\lambda}\right). \tag{27}$$

Further note that for $\nu_m \simeq 0.3$

$$\alpha = \sqrt{\frac{\mu_m}{E_i r^2}} = \frac{1}{r}\sqrt{\frac{E_m}{2E_i(1+\nu_m)}} \frac{1}{rq\sqrt{2.6}}.$$

Evidently for values of $q > 1$ (inclusion with higher modulus than the matrix) the inclusion strain will be somewhat lower than the matrix strain, as predicted by eq. (27). The equation can easily be converted for stresses and then it will show $\sigma_{max} > \sigma_m$.

It is now assumed that the inclusion fractures if ε_{max} exceeds a critical value ε_{cr}. This fracture criterion seems sound, because it states that the deformation properties of the inclusion are limited and when these are exhausted fracture of the inclusion will occur. The result is that voids will be initiated at a matrix strain

$$\varepsilon_{void} = \frac{\varepsilon_{cr}}{1 - \dfrac{q^2 - 1}{q^2 \cosh \alpha\lambda + q \sinh \alpha\lambda \tanh \alpha q\lambda}} \tag{28}$$

Eq. (28) implies that the strain at void initiation depends on the ratio E_i/E_m and the length to thickness ratio λ/r of the inclusion. The strain producing void initiation by inclusion fracture has been calculated from eq. (28) as a function of these parameters; the results are plotted in fig. 17, showing that the effect of inclusion stiffness vanishes for very slender inclusions. It should be kept in mind that it is assumed that all inclusions have the same fracture strain.

Of course, void initiation might also occur at the ends of the matrix-particle interface due to the concentration of tensile stress. The tensile stress on the end surface of the inclusion follows from eq. (26) by putting $x=\lambda$. Finally it is theoretically possible for void formation at the interface to occur in the longitudinal direction as a result of shear stress concentration. A condition for such failures can also be obtained from the foregoing analysis. This kind of void formation, however, has not been observed during this investigation and therefore the aforementioned condition is probably irrelevant.

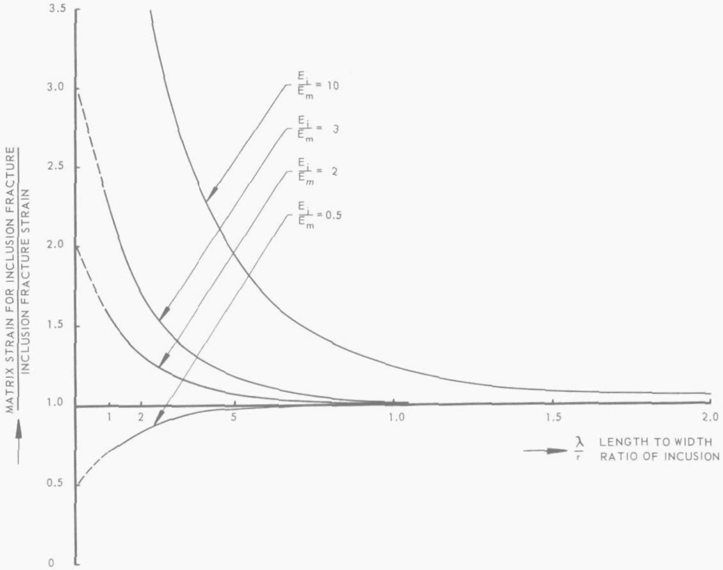

Fig. 17. Matrix strain to fracture a cylindrical inclusion. (Elastic solution of chapter 5).

5.4 *Significance of the equations for void initiation*

In this chapter a variety of equations have been discussed which try to relate void initiation to structural parameters. In most formulae the critical stress or strain is predicted to depend on particle size and shape. It is felt that the formulae which do not predict a dependence on particle shape cannot be of great value. Unfortunately, quantitative data could not be obtained during the present investigation from the particles exemplified by figs 7 and 8. Qualitatively, however, it can be concluded that void initiation depends on particle shape. The observations have shown that large inclusions may break at low strains (fig. 1). The condition developed in eq. (28) predicts that long particles will fracture earlier than particles with low aspect ratio. Evidence of fractured elongated particles (figs 7 and 8) suggests this to be correct.

The question arises whether quantitative data were unobtainable because of shortcomings in the experimental techniques or because void initiation is the critical event in ductile fracture: the latter would mean that some isolated voids may occur, but that void formation in larger numbers rapidly instigates void coalescence. This question will be discussed after consideration of the criteria for void growth and coalescence. It is thought that any comparison with experimental data should be postponed until the picture of the fracture process is completed to the extent presently possible. Therefore void growth and coalescence will be considered first.

5.5 *Condition for coalescence as proposed in the literature*

In a recent review Rosenfield [3] concluded that void coalescence is the most critical and least understood aspect of the fracture process. In this section the criteria for void growth and coalescence as presented in the literature will be discussed. Chapter 6 will give a critical inventory of existing knowledge and reported experimental observations. This too will lead to a model for void growth and coalescence, compatible with the observations. A condition for void coalescence (fracture instability) will also follow from this model.

For a discussion of void growth the relations between particle size, particle distance and volume fraction of particles are required. Various relations are given in the literature, whose differences are merely due to the use of different parameters such as average nearest neighbour distance, average distance, mean free path, etc. An elegant treatment of these problems has been given by Fullman [26]. At this stage the most elementary formula that gives the basic relations between volume fraction f, particle size a and particle distance s will suffice. This relation is derived in the appendix (sect. 10.9) as

$$f = \frac{\pi}{6}\left(\frac{a}{s}\right)^3 . \tag{29}$$

The first model for void coalescence has been proposed by Gurland and Plateau [12]. They consider an idealized ellipsoidal void and they assume a somewhat dubious strain concentration factor k_ε at the equator: namely

$$k_\varepsilon = \frac{\mathrm{d}\varepsilon_{\max}}{\mathrm{d}\varepsilon} = 1 + C\,\frac{a^2}{p^2} . \tag{30}$$

In this equation $\varepsilon_{\max}$ is the strain at the equator, ε the nominal strain in the matrix, C is a constant and a and p are minor and major axes of the void (a is also the diameter of the spherical particle that initiated voids at its poles). Since by the definition of strain $\mathrm{d}\varepsilon_{\max} = \mathrm{d}p/p$ it follows that

$$\frac{\mathrm{d}p}{p} = \left(1 + C\,\frac{a^2}{p^2}\right) \mathrm{d}\varepsilon . \tag{31}$$

In the case of a relatively rigid inclusion, a will not vary and eq. (31) can be integrated to

$$\ln(p^2 + Ca^2) = 2\varepsilon + \text{constant}\,.$$

The boundary condition is that at the initiation of void growth $\varepsilon = \varepsilon_{\text{void}}$ and $p = a$; hence

$$p^2 = -Ca^2 + (1+C)a^2 \, e^{2(\varepsilon - \varepsilon_{\text{void}})}\,. \tag{32}$$

Eq. (32) is different from that obtained by Gurland and Plateau, because they erroneously assumed $p=0$ at $\varepsilon = \varepsilon_{\text{void}}$. If $(1+C)$ is considered to be $\simeq C$, then eq. (32) yields

$$p^2 = Ca^2 \left(e^{2(\varepsilon - \varepsilon_{\text{void}})} - 1\right). \tag{33}$$

This result is identical to the equation of Gurland and Plateau. They then assumed that the void grew in size according to eq. (33), i.e. as a geometrical consequence of tensile strains. In their fracture criterion Gurland and Plateau introduce the particle distance s by stating that internal necking between the voids will occur if the ratio p/s exceeds a critical value. Using this fracture criterion and the relation in eq. (29) gives

$$\varepsilon_{\text{fracture}} = \varepsilon_{\text{void}} + \tfrac{1}{2} \ln\left(\frac{D}{C} f^{-\frac{1}{3}} + 1\right). \tag{34}$$

Since Gurland and Plateau also considered the variation in s due to straining, they obtained a slightly different equation. Relations for $\varepsilon_{\text{void}}$ as obtained in the previous sections could be substituted in eq. (34), but it is considered that eq. (34) is based on a dubious assumption, and it will not be evaluated further.

Another criterion for void coalescence has been proposed by Thomason [27] for the two-dimensional case; he considers the condition for necking of the material between regularly distributed prismatic voids in an element of unit thickness (fig. 18). Thomason assumes that necking occurs if the net section stress σ_n exceeds a critical value. The net section stress is related to the nominal stress σ by the relation $dx = \sigma_n (dx - nw)$, or

$$\sigma = \sigma_n \left(1 - \frac{nw}{dx}\right). \tag{35}$$

This relation is shown diagrammatically in fig. 18.

According to fig. 18 the volume fraction of the cavities is given by $nw \cdot nw/dx \cdot dy = (nw/dx)^2 = f$. Hence the condition for coalescence (necking) is

CHAPTER 6

DEVELOPMENT OF A FRACTURE MODEL

6.1 *Inventory of experimental evidence*

In this section a critical inventory will be made of observations of void growth reported in the literature and in the present investigation. This leads to a description of the fracture process, in phenomenological terms, which set a number of conditions for a fracture model. A model satisfying these requirements will be developed in the next section.

Bluhm and Morressey [31] claimed that they could follow growth and coalescence using a very hard tensile machine and subsequently examining longitudinal sections of their specimens by optical microscopy. They stated that only the final stage was rapid and catastrophic. However, it seems that one can easily be misled when sectioning necked specimens for examination with the optical microscope in the manner of Bluhm and Morressey [31] and, for example, Clausing [32]. In the previous chapters it has become clear that voids are of the sub-micron size, i.e. they are not visible with the optical microscope. Voids may occur at low strain at large particles (fig. 1), but the present experiments have shown that these early voids are irrelevant to the fracture process, although they may be of indirect influence. As fig. 1 shows, straining proceeds long after the initiation of these voids, although the large voids may grow gradually during the straining process (fig. 2). Consequently, so called 'voids' observed with the optical microscope are either of the type shown in fig. 1, or they are cracks rather than voids. The latter suggestion implies that void coalescence must already have taken place to form a small crack, but apparently the tensile machine was so hard that the conditions for void coalescence could not be maintained. Consequently void coalescence can still be considered an unstable process.

Conclusive evidence has been presented in chapter 4 that small particles (of the order of a tenth of a micron) are responsible for ductile fracture. Many of the alloys considered contained particles of even smaller size: most materials were of the precipitation hardening type and were in a condition to contain precipitates of a few hundred Ångstrøms in size (e.g. the 2024, 2014 and 7075 materials). These particles control the yield strength of the material and also to a certain extent the strain hardening characteristics. Apparently the precipitates are not of primary importance for the very occurrence of fracture, although this is sometimes suggested in the literature. In chapter 4 it appeared that particles in the order of 1000 to 3000 Ångstrøms in size are important for ductile fracture. In a specially treated 2024 alloy Broek and Bowles [33] obtained slender θ' precipitate particles of about 3000 Å in size, whereas the alloy also contained spheroidal inclusions of the type shown in figs. 1, 7 and 8, of the same size as the θ' precipitate, but with larger spacing. The resulting dimple size in said material was roughly equal to the inclusion spacing, suggesting that the θ' precipitate played no role in the fracture process.

This example does not exlude the possibility that precipitates (or eventually even GP zones) might initiate voids and fracture (in a later stage) if the inclusions were absent. The fact, however, that GP II and θ' precipitates are coherent or semi-coherent with the matrix, whereas inclusions are non-coherent, will make all the difference.

The available evidence on micro-void initiation and growth will now be considered. As stated before the observations reported bear almost exclusively on materials strengthened with oxide particles. The cohesive forces between the oxide particles and the matrix must be low. As a result of the stress concentration at the poles the decohesion forces are exceeded at relatively low stresses, resulting in cavities at the poles. These were observed at oxide particles by several investigators [7, 8, 9] and also at large spherical inclusions in the present study (fig. 6).

Some information on void initiation might be expected from the experiments in the straining stage of the electron microscope, like in the work of Ruedl on SAP. Fig. 20 shows how the crack passes a practically spherical inclusion. In fig. 20a the crack has approached the boundary of the inclusion and consequently the stresses in the inclusion must be very high. Yet, no cavities have been formed, nor has the particle cracked. In fig. 20d the crack has passed along the interface. The example indicates that coherency forces along the interface are high and the plastic deformation possibilities of the particle are reasonable. Of course, the evidence presented in fig. 20 is subject to some doubt, because it relates to a thin foil in which a triaxial state of stress cannot exist. Cracking is considered to occur as necking to a point (or line), which is supported by the fact that the non-transmitting part of the foil became transparent if the crack passed through it. Fracture is a result of slip plane decohesion. The same is considered to occur three-dimensionally during void growth. (The thin foil can more or less behave as a single crystal, because the dimensions of the grains are large as compared to their thickness).

Micro-voids and void growth were hardly observed in the present in-

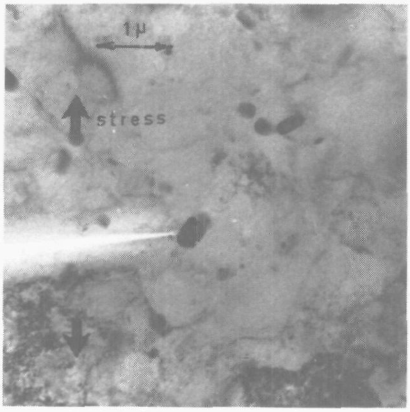

(a) Particle at tip of crack.

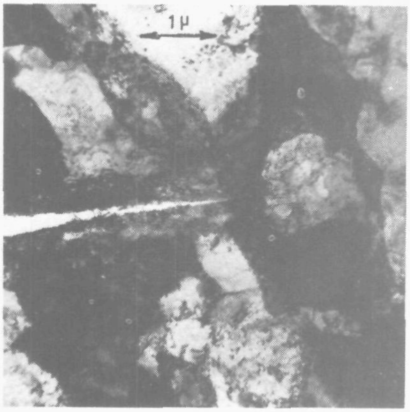

(b) Same crack with dislocations tilted into contrast, showing formation of sub-grain cells.

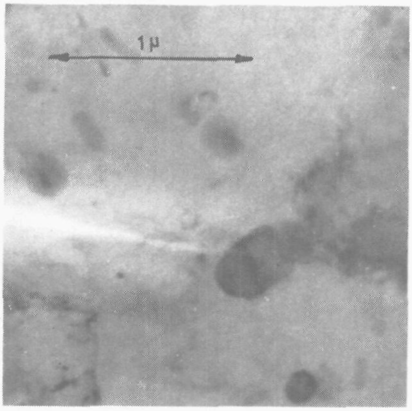

(c) Enlarged picture of (a). Particle at tip of crack.

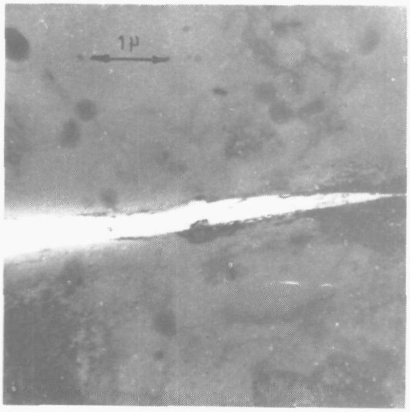

(d) Interface decohesion after passage of crack.

Fig. 20. Passage of crack along inclusion interface in thin foil specimen. 7075 material. Direction of straining from top to bottom.

vestigation. The elongated inclusions seem to fail first prior to fracture, but growth of the so-formed cavities was hardly observed. Similar observations were made by Brindley [34], who studied replicas of sectioned tensile specimens in the electron microscope. In some cases he found cracked particles, but he did not observe void growth.

Further observations are reported in a recent publication of Calhoun and Stoloff [35] on magnesium alloys. However, in accordance with the present results, Calhoun and Stoloff report that the dimple size qualitatively agrees with the distance of small inclusions visible in surface replicas. They also confirm the present observations which indicate that premature cracking of large inclusions is irrelevant for fracture.

Apparently void initiation and growth does not occur until the onset of fracture. Calhoun and Stoloff arrived at the same conclusion, and as a consequence they consider dimples more or less a by-product of ductile fracture. They suggest that if small voids are finally formed, fracture by plastic instability will occur in the weakened section. This fracture will follow a path along the voids and as such will develop the dimples, which then of course can be correlated with inclusions. However, it seems rational to adhere to the alternative, though not altogether contradictory viewpoint that once the voids are initiated in some quantity the conditions for their unstable growth are immediately fulfilled. This requires that a model for void initiation should predict immediate and spontaneous void growth. Therefore void growth has to be considered first.

Where void growth was observed, it occurred primarily in the direction of the tensile stress; the best example is presented by Ruedl [9]. Apparently this type of growth is a normal consequence of longitudinal straining, occurring also under elastic conditions. It is considered that this mode of growth can occur even if voids are initiated well before fracture as for example in fig. 1.

From a physical point of view one would expect that a cavity should spread preferentially in a direction perpendicular to the tensile stress (i.e. like a crack) rather than in the direction of the tensile stress. The latter case would be merely a consequence of matrix deformations. Void growth perpendicular to the tensile stress would occur by a mechanism of slip plane decohesion, as has been proposed for crack growth by McLean [1] and later in greater detail by several others.

There is the following indirect evidence for lateral growth of voids:

(a) The measured dimple profiles in figs 9 and 10 suggest void growth perpendicular to the direction of the tensile stress, since the depth to width ratio of the dimples (as derived from stereoscopic measurements, fig. 9b) is of the order of $\frac{1}{3}$ to $\frac{1}{5}$, a figure that also emerges from the cross sections of replicas, as shown in fig. 9a.

(b) When void coalescence is considered as internal necking of the material between cavities, then according to fig. 21 and the condition for constant volume

$$s^2 a = 2s^2 p - \tfrac{1}{3}\pi p s^2$$
$$p \simeq a$$

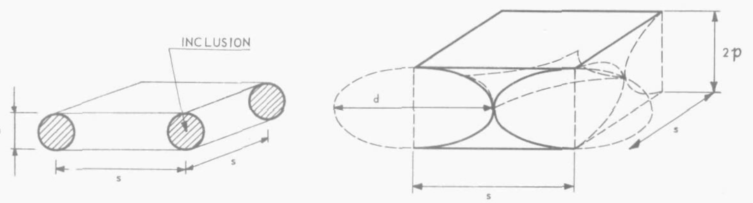

Fig. 21. Void coalescence by internal necking of material between cavities.

which implies that the depth p of the dimples should be of the order of the initial void size. Thus it may also be stated that

$$\frac{s}{a} \simeq \frac{d}{p} \tag{39}$$

or in other words the depth to width ratio of the dimples may be expected to be of the order of the ratio between inclusion size and spacing.

(c) If in practice the voids would generally grow in the tensile direction the position of the inclusion would not be visible in the electron micrographs: i.e., after decohesion the area of previous contact would be drastically deformed and the print of the inclusion would

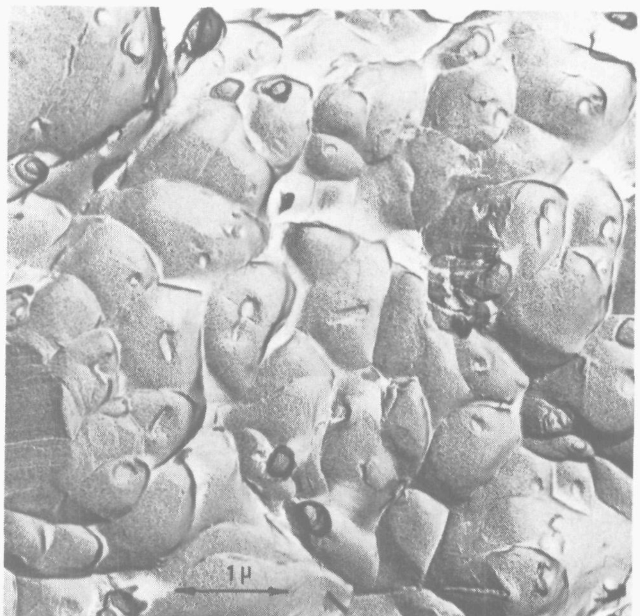

Fig. 22. Inclusions visible in dimples. 7079 material.

be obliterated. The prints of inclusions can be seen, however, in almost any dimple, as is shown convincingly in fig. 22 and also in fig. 3.

(d) Soap bubble rafts prepared according to the method developed by Bragg and Nye [36] were used during a previous investigation [37] to simulate void growth. Similar models were used in this study, details of which are given in the appendix (sect. 10.10). The present results, as well as the previous ones (37), suggest lateral void growth perpendicular to the tensile stress. Examples of successive stages of a growing cavity are shown in fig. 23. The voids in the soap bubble raft appear to grow by a process analogous to slip plane decohesion. The void growth in fig. 24 is also considered to be the result of slip plane decohesion.

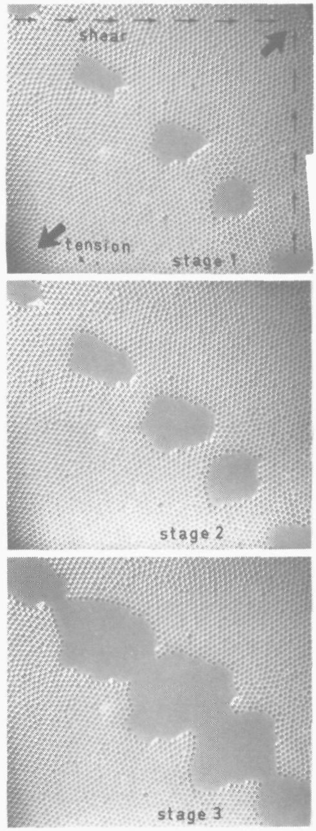

Fig. 23. Void growth in a soap-bubble raft.

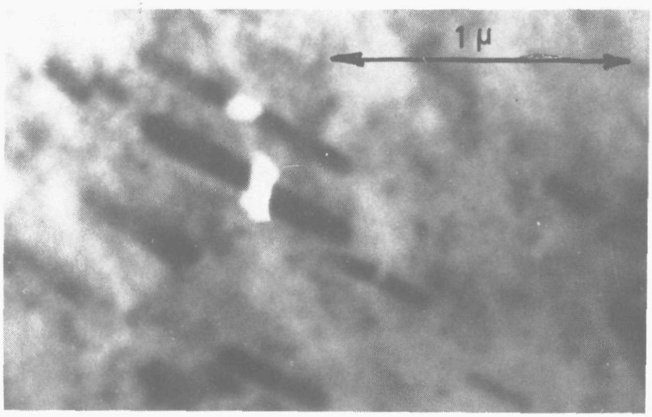

Fig. 24. Extension of void perpendicular to tensile stress. 2024 material.

Summarizing, the inventory of experimental evidence has revealed the following facts:

(a) Large voids at large inclusions, observed with the optical microscope, are not essential to the fracture process.
(b) If voids occur in an early stage, they may grow in the direction of tensile stress as a result of increasing matrix strains; this case, however, is applicable mainly to dispersion in strengthened materials.
(c) Cavities may occur some time before fracture as a result of the failure of elongated particles.
(d) Void initiation before fracture has been observed to take place only on a very limited scale. Void initiation on a large scale probably leads to spontaneous growth and coalescence.
(e) Void growth by slip plane decohesion, i.e. by shear stresses, must occur primarily in a direction perpendicular to the tensile stress, as in fig. 23.

A physical model of fracture by void initiation, growth and coalescence should be compatible with these facts.

6.2. *A model for coalescence*

A model that reasonably satisfies the conditions listed at the end of the previous section is considered to be the following.

During plastic deformation dislocation pile-up groups will form at the particles. These are pile-ups of loops as sketched in fig. 25a; the loops are formed according to the mechanism of fig. 12a. They are repelled by the particle through the action of their image forces. On the other hand, the leading loop will be pushed towards the particle by stresses set up by the pile-up and the applied shear stress. When the back stress on the leading loop exceeds the image force, then this first loop will move towards the matrix-particle interface. When one or a couple of loops are pushed to the interface a decohesion of the interface will ultimately take place along AB in fig. 25c. If this occurs a void is formed. The consequence is that the repelling forces on subsequent loops are drastically reduced and the greater part of the pile-up can empty itself into the newly formed void, as will be shown hereafter. The dislocation sources behind the loops, which became inactive because of the constraint of the pile-ups ahead, can resume action and hence the process may lead to unstable void growth and coalescence as soon as the voids have been initiated (fig. 25c, d). An estimate of the number of dislocations contributing to void growth can be made and it leads to an estimate of the amount of void growth in the following approximate way. When as a result of the mechanism of fig. 12 a number of n dislocations have piled up against a particle n dislocations must have passed it. The average distance travelled by a dislocation will be of the order of the particle distance; also it can be assumed to move in the area enclosed by four particles, i.e. in an area s^2. Consequently the shear strain will be given by

$$\gamma = \frac{\boldsymbol{b}ns}{s^2} = \frac{\boldsymbol{b}n}{s}. \tag{40}$$

The interface decohesion can take place along AB over a vertical distance $a/2$. Any dislocation running into the void will shear the material along the void by an amount $2\boldsymbol{b}/a$ (fig. 25e). This will require a shear stress $\tau = 2\mu\boldsymbol{b}/a$. The back stress on the leading dislocation will be $n\tau_a$ if τ_a is the

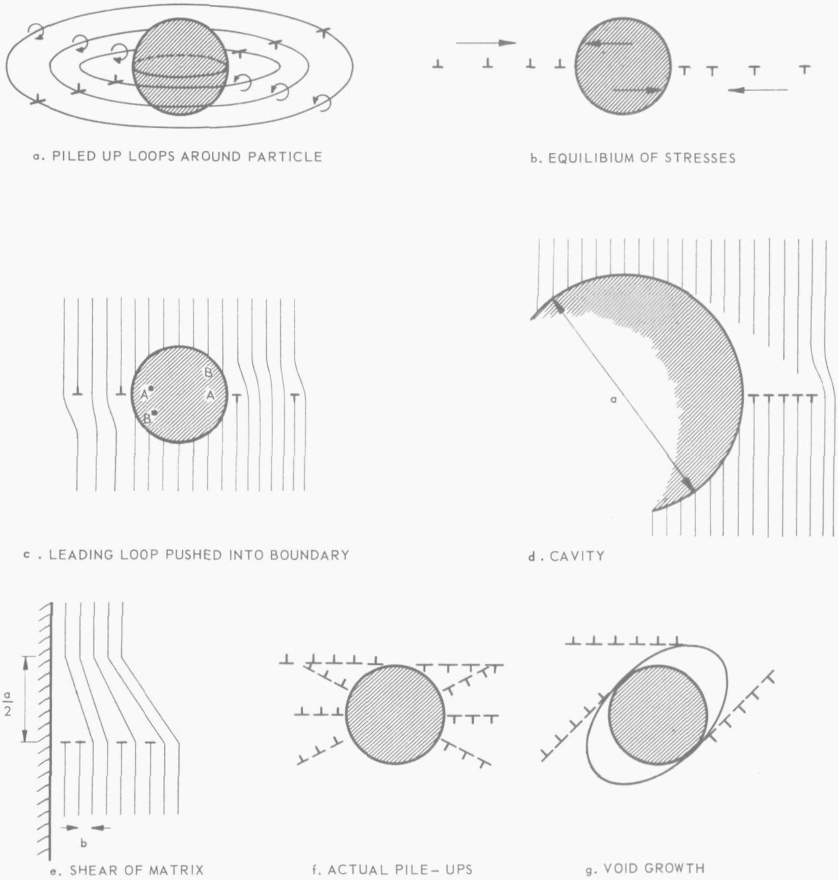

Fig. 25. Model for void initiation and void growth.

applied shear stress. Hence if m dislocations run into the void, the equilibrium of stress requires

$$\frac{2m\mu\boldsymbol{b}}{a} = (n-m)\tau_a \tag{41}$$

where $m\boldsymbol{b}$ is the amount of void growth Δd. When multiplying by $s\boldsymbol{b}$ one can also write

$$\Delta d\left(1+\frac{a\tau_a}{2\mu\boldsymbol{b}}\right) = \frac{a\tau_a s}{2\mu\boldsymbol{b}}\cdot\frac{n\boldsymbol{b}}{s}.$$

Substitution of eq. (40) leads to

$$\frac{\Delta d}{s} = \frac{\gamma}{1+2\mu\boldsymbol{b}/a\tau_a}. \tag{42}$$

Substitution of typical values, $\mu \simeq 3000$ kg/mm^2, $\boldsymbol{b} \simeq 3\cdot10^{-7}$ mm, $a \simeq 10^{-4}$ mm, $\tau_a \simeq 30$ kg/mm^2 and $\gamma \simeq 0.3$ (obtained as a reasonable value from the true strain data in Table 2) gives $\Delta d/s \simeq 0.20$, implying that immediate void growth can occur over 20% of the distance between particles. If the dislocation sources resumed action, such that the number of dislocations in the pile-up remained constant

$$\frac{2m\mu\boldsymbol{b}}{a} = n\tau_a \tag{43}$$

giving

$$\frac{\Delta d}{s} = \frac{a}{2\boldsymbol{b}}\,\frac{\tau_a}{\mu}\,\gamma\,. \tag{44}$$

Substitution of the above values gives $\Delta d/s \simeq 0.5$, which implies immediate coalescence.

In reality, the extreme case of one giant pile-up will not occur. Friedel [38] argues that plastic relaxation of the pile-up stresses begins when the stress exerted by the pile-up group on the secondary sources exceeds the elastic limit. He shows that pile-up groups in face centered cubic crystals should be completely relaxed if they contain about 5 dislocations. This implies that many pile-ups must be formed on different slip planes, as in fig. 25f. Also, this situation will finally lead to interface decohesion when one or more dislocations are pushed into the interface. These newly formed voids can now grow due to dislocations on other slip planes that run into the void (fig. 25g). This growth is shown in fig. 26 in terms of slip displacements.

An evaluation of the model will prove to be extremely complicated, if at all possible. So far, only two-dimensional problems have been treated in the literature. Barnett and Tetelman [39] gave a solution for a pile-up of screw dislocations against a circular cylindrical inclusion of infinite rigidity, the dislocation lines running parallel to the cylinder axes. Their

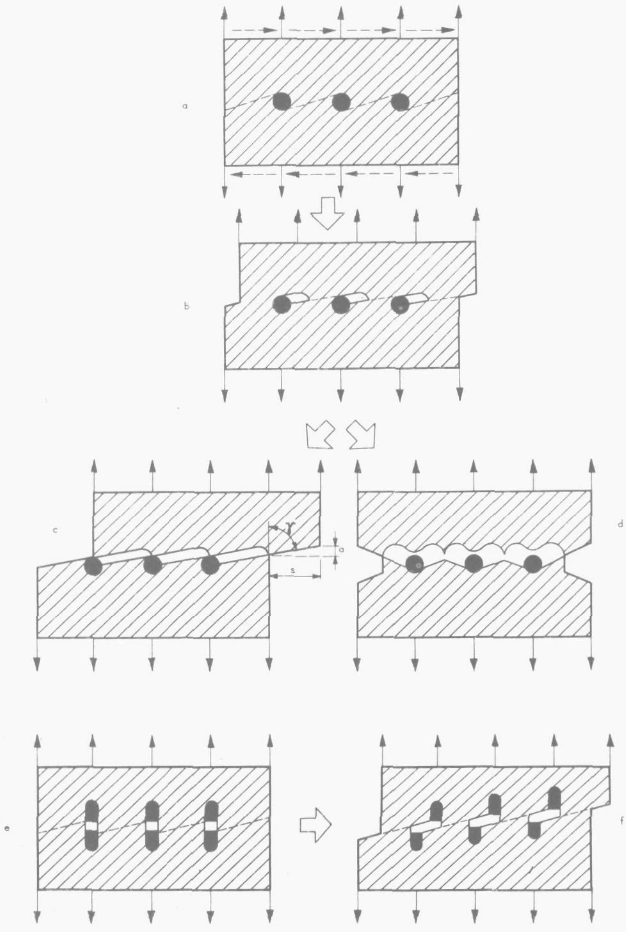

Fig. 26. Void coalescence.

solution was improved by Smith [40]. The interaction of a single edge dislocation with a circular cylindrical inclusion was treated by Dundurs and Mura [41] and by Dundurs and Gangadharan [42]. Weeks *et al.* [43] consider the interaction between a straight dislocation and a spherical particle. The two-dimensional problems are already so complicated that solutions were obtained for special cases only. Generalization is not possible because of the intricate results for each individual situation. According to Dundurs and Gangadharan [42] the knowledge in this field has to come by slow accumulation of results for special cases. A solution for the case under consideration may not be obtained for a long time. However, a rough approximation for the two-dimensional case of a circular cylindrical inclusion of infinite stiffness with a pile-up of screw dislocations is possible. This may be sufficient for a first estimate of the parameters involved and for a check with experimental results.

The image force acting on a screw dislocation at a distance λ from a free surface is

$$F = -\frac{\mu \boldsymbol{b}^2}{4\pi\lambda} \tag{45}$$

where the minus sign indicates an attractive force. The image force on a dislocation at a distance $x=\lambda$ from a straight bimetallic interface positioned at $x=0$ is given by Head [44]. The material in $x<0$ has a modulus μ_p, the material in $x>0$ has a modulus μ_m. It can readily be shown that the dislocation of strength $\boldsymbol{b}$ at $x=\lambda$ will exert a stress in the material μ_p as if there was a dislocation of strength $2\boldsymbol{b}\mu_m/(\mu_m+\mu_p)$ at $x=\lambda$ in an infinite matrix with modulus μ_m. Furthermore, the stress in the material μ_m will be the same as that induced by a dislocation of strength $\boldsymbol{b}$ at $x=\lambda$ and a dislocation $(\mu_p-\mu_m)\boldsymbol{b}/(\mu_p+\mu_m)$ at $x=-\lambda$, both in an infinite matrix with modulus μ_m. The stresses exerted by this set of three dislocations have to be continuous at the interface. Thus

$$\left(\frac{\mu_p-\mu_m}{\mu_p+\mu_m}-1\right)\frac{\boldsymbol{b}\mu_m}{2\pi\lambda} = -\frac{2\mu_m}{\mu_m+\mu_p}\cdot\frac{\boldsymbol{b}\mu_m}{2\pi\lambda}. \tag{46}$$

Hence, the image of $\boldsymbol{b}$ at $x=\lambda$ is $(\mu_p-\mu_m)\boldsymbol{b}/(\mu_p+\mu_m)$ at $x=-\lambda$ and the image force is

$$F = \tau\boldsymbol{b} = \frac{\mu_p-\mu_m}{\mu_p+\mu_m}\mu_m\frac{\boldsymbol{b}^2}{4\pi\lambda} = \kappa\mu_m\frac{\boldsymbol{b}^2}{4\pi\lambda} \tag{47}$$

i.e. the image force equals κ times the image force at a free surface ($\mu_p=0$; $\kappa=-1$); the image force is repulsive if $\mu_p>\mu_m$.

According to Friedel [38] the images of a screw dislocation at a distance λ from the axis of a cylindrical cavity of radius $a/2$ are one dislocation of strength $-\boldsymbol{b}$ in the cylinder axis and one dislocation of strength $\boldsymbol{b}$ at a distance $a^2/4\lambda$ from the cylinder axis, so that the image force becomes

$$F = \tau \boldsymbol{b} = -\frac{\mu \boldsymbol{b}^2}{2\pi}\left(\frac{1}{\lambda - a^2/4\lambda} - \frac{1}{\lambda}\right). \tag{48}$$

In the case of a cylindrical inclusion with modulus μ_p embedded in a matrix with modulus μ_m, the factor $-\mu$ in eq. (48) has to be replaced by $\kappa\mu_m$ as in the case of a straight bimetallic interface.

Barnett and Tetelman [39] solve the problem of a group of n parallel-screw dislocations piling up against a cylindrical inclusion of infinite rigidity $\mu_p \gg \mu_m$, i.e. $\kappa = 1$. The pile-up is pushed against the obstacle by a shear stress τ. Barnett and Tetelman ignored the fact that the stress field resulting from the externally applied stress τ_a is affected by the presence of the inclusion. Smith [40] solved the problem of the pile-up under the action of the correct shear stress by using the same procedure as Barnett and Tetelman [39]. The shear stress τ in the slip plane due to the applied stress depends on the distance x from the center of the inclusion by $\tau = \tau_a\,(1 - a^2/4x^2)$, where a is the diameter of the inclusion. Hence the stress piling-up the dislocations is $\tau = \tau_a\,(1 - a^2/4x^2) - \tau_i$, where τ_a is the externally applied shear stress and τ_i the lattice friction stress opposing the movement of the dislocations.

The equilibrium of stresses in the slip plane ($y = 0$) along the X-axis (with $x = 0$ at the inclusion center) is given by

$$\frac{\mu_m \boldsymbol{b}}{2\pi}\left[-\frac{n}{x} + \sum_{i=1}^{n} \frac{1}{x - a^2/4\lambda_i} + \sum_{i=1}^{n} \frac{1}{x - \lambda_i}\right] =$$

$$= \tau_a\left(1 - \frac{a^2}{4x^2}\right) - \tau_i \tag{49}$$

where λ_i is the position of each individual dislocation on the X-axis. The third term in eq. (49) represents the stress due to the n real dislocations, the second term represents the stress due to the n image dislocations at postions $a^2/4\lambda_i$ (see also eq. (48)) and the first term gives the stress exerted by n image dislocations at the center of the inclusion (one resulting from each real dislocation).

The solution of eq. (48) is obtained by replacing the discrete dislocations by a continuously distributed array, which allows the equation to be written in integral form. After a complicated mathematical treatment Smith [40] arrives at

$$\frac{\mu \boldsymbol{b} n}{2L\tau_a} = \frac{\pi}{2}\,\frac{2L/a}{1+2L/a} +$$

$$-\frac{\tau_i}{\tau_a}\left\{\left(\frac{1}{1+2L/a}\right)^{\frac{1}{2}} + \frac{2L/a}{2(1+2L/a)}\left[\frac{\pi}{2} + \arcsin\frac{2L/a}{2+2L/a}\right]\right\} \quad (50)$$

in which L is the length of the pile-up.

Eq. (50) can be applied to the present problem. It may be assumed that the pile-up length L will be of the order of half the particle spacing, i.e. $2L=s$. Substitution of this and of eq. (40) in eq. (50) leads to

$$\frac{\mu\gamma}{\tau_a} = \frac{\pi}{2}\,\frac{s/a}{1+s/a} +$$

$$-\frac{\tau_i}{\tau_a}\left\{\left(\frac{1}{1+s/a}\right)^{\frac{1}{2}} + \frac{s/a}{2(1+s/a)}\left[\frac{\pi}{2} + \arcsin\frac{s/a}{2+s/a}\right]\right\}. \quad (51)$$

The number of dislocations in the pile-up depends upon the shear stress τ_a, and the process of void growth can start if either τ_a or n exceeds a critical value to push sufficient dislocations into the interface to initiate the void. Hence γ in eq. (50) is the fracture strain γ_f if τ_a equals the fracture stress τ_f. In the more realistic case that the inclusion has finite rigidity the factor $\kappa=(\mu_p-\mu_m)/(\mu_p+\mu_m)$ enters in the expression. On the basis of calculations by Chou [45] and Barnett [46] for a pile-up at a straight bimetallic interface it will be assumed as a first estimate that it only affects the factor μ in the preceding equations; this factor can then be accounted for by adding a constant factor. Consequently, the fracture condition in terms of true tensile stress and true tensile strain at fracture will be

$$\frac{\varepsilon_f}{\sigma_f} = \frac{C}{\mu}\left[f_1\left(\frac{s}{a}\right) - \frac{\sigma_i}{\sigma_f} f_2\left(\frac{s}{a}\right)\right] \quad \text{or} \quad \varepsilon_f^{1-m} = C\frac{\sigma_0}{\mu}\left[f_1\left(\frac{s}{a}\right) - \frac{\sigma_i}{\sigma_f} f_2\left(\frac{s}{a}\right)\right]$$

with (52)

$$f_1\left(\frac{s}{a}\right) - \frac{\sigma_i}{\sigma_f} f_2\left(\frac{s}{a}\right) =$$

$$= \frac{\pi}{2}\,\frac{s/a}{1+s/a} - \frac{\sigma_i}{\sigma_f}\left\{\left(\frac{1}{1+s/a}\right)^{\frac{1}{2}} + \frac{s/a}{2(1+s/a)}\left[\frac{\pi}{2} + \arcsin\frac{s/a}{2+s/a}\right]\right\}.$$

It should be noted that according to eq. (29):

$$\frac{s}{a} = \left(\frac{\pi}{6f}\right)^{\frac{1}{3}}$$

implying that

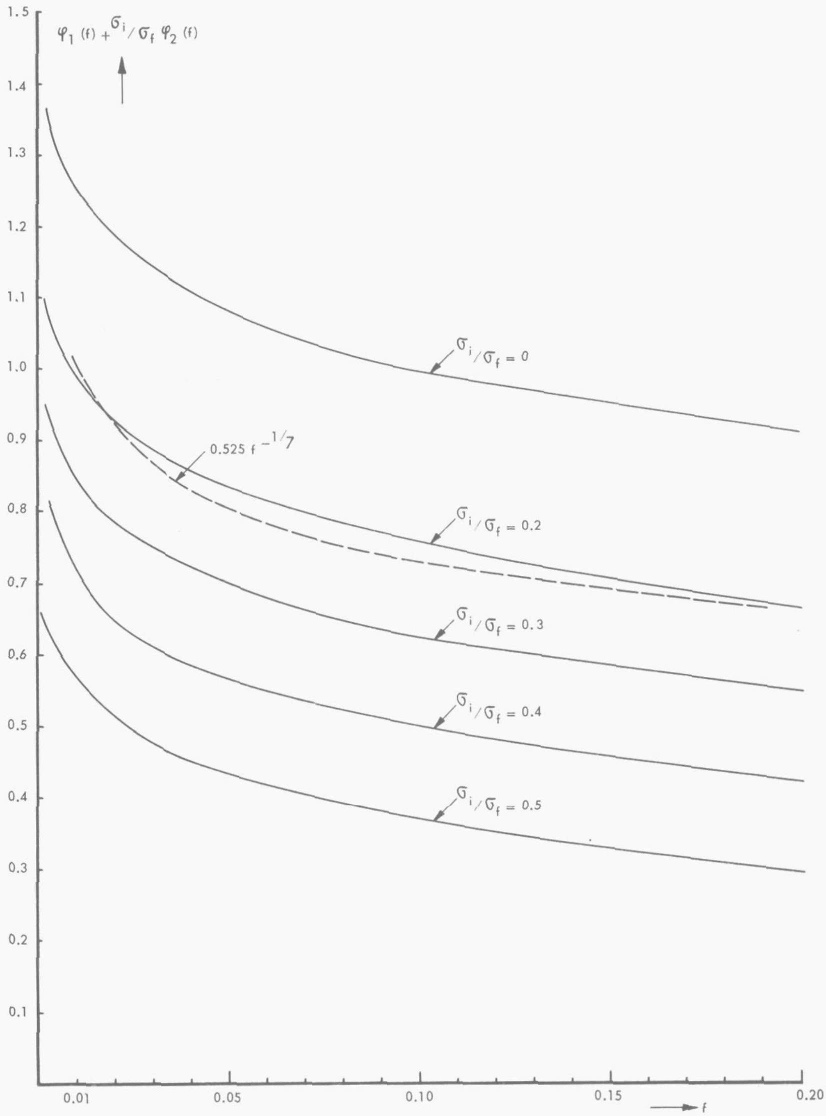

Fig. 27. $\varphi_1(f) - \sigma_i/\sigma_f\,\varphi_2(f)$ *versus* volume fraction f for different values of σ_i/σ_f. (For dashed line see Chapter 8)

$$\frac{\varepsilon_f}{\sigma_f} = \frac{C}{\mu}\left[\varphi_1(f) - \frac{\sigma_i}{\sigma_f}\,\varphi_2(f)\right]. \tag{53}$$

As far as structural parameters affect the fracture properties, eq. (53) predicts that the fracture strain depends uniquely upon the particle volume fraction, as in the formulae given by Gurland and Plateau, Thomason, and McClintock. The expression $\varphi_1(f)-\sigma_i\cdot\varphi_2(f)/\sigma_f$ has been calculated according to eqs (29) and (52) for various values of σ_i/σ_f and f. The result is shown in fig. 27, indicating that a smaller volume fraction of particles will give a higher fracture strain.

The main objection to eq. (53) is that it has been derived for the two-dimensional case. An extension to the three-dimensional case would introduce additional difficulties, apart from the mathematical complications. In the first place the dislocation lines would be circles (fig. 25) trying to contract. The contraction stress would enter into eq. (49). Secondly, the radius of curvature of the dislocation loops would enter into the equations, as may be assumed on the basis of the work of Leibfried [47], who studied the inverse case of expanding loops piling-up against a circular barrier outside the pile-up. Thirdly, the dislocations would be partly of the edge-type; according to Dundurs and Mura [41] this would result in a strong dependency on the difference between the Poisson's ratios of the matrix and the inclusion. Of course, many other objections can be raised against eq. [53], two of which are a possible volume misfit of the inclusion as a result of solidification and differences in thermal expansion; both will induce new stresses. For the time being, however, the two-dimensional solution used here is considered suitable for an evaluation of the parameters involved in the proposed model.

6.3 *Verification with experimental data*

The model developed in the previous section assumes that dislocation loops pile up around the particles. Dislocation pile-ups have been observed by several investigators in electron microscope specimens; good examples are given by Friedel [38]. In the present investigation regular pile-up groups of loops were not observed: fig. 28a shows the dislocation configuration in a material before straining. Nevertheless, the particles do affect the dislocations, all dislocations being pinned at the particles. The dislocation distribution after fracture is shown in fig. 28b; no loops can be observed. Several reasons to explain this are given in the following paragraph.

Large segments of pile-up loops must have disappeared during foil preparation, because the foil thickness is of the order of the particle size.

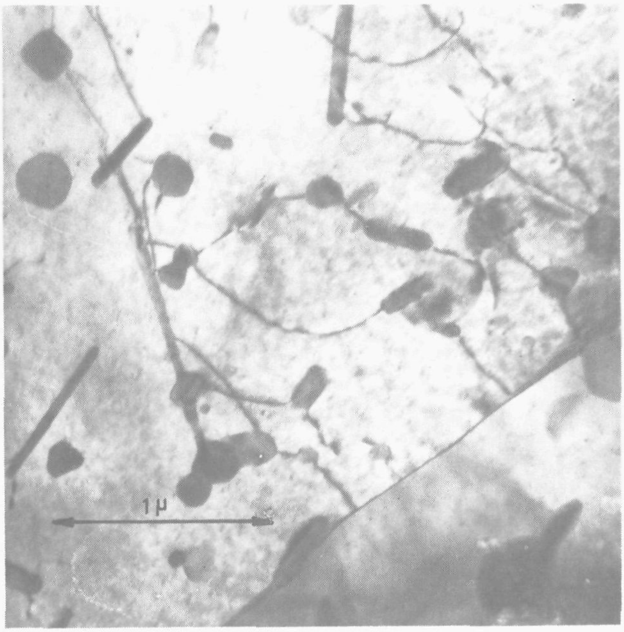

(a) Dislocation configuration before straining 7079 material.

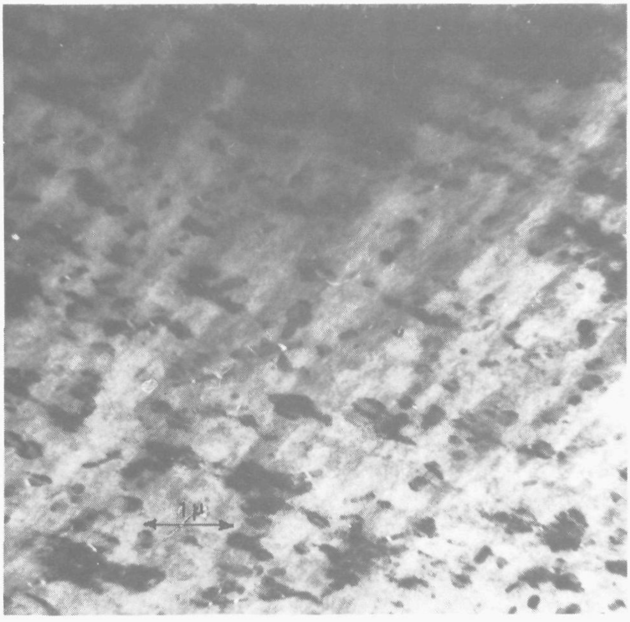

(b) Dislocation distribution after straining 7079 material.

Fig. 28. Dislocations before and after straining.

Remaining loops may have been pushed so close to the particles that their contrast cannot be resolved. Relaxation of pile-ups must have taken place to a large extent by the formation of pile-up groups in secondary slip systems, as explained in the previous section. Pile-ups in secondary systems must be relatively easy in aluminium alloys, because of the large number of slip systems available. Because of the high stacking fault energy,

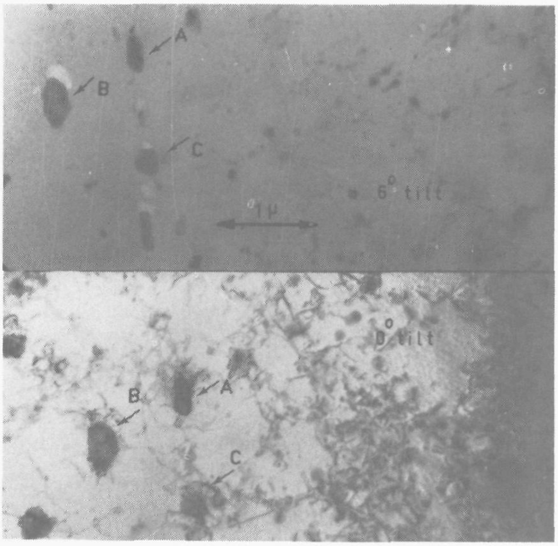

(a) 6061 material in two tilt positions. (Note similar inclusions at arrows A, B, C)

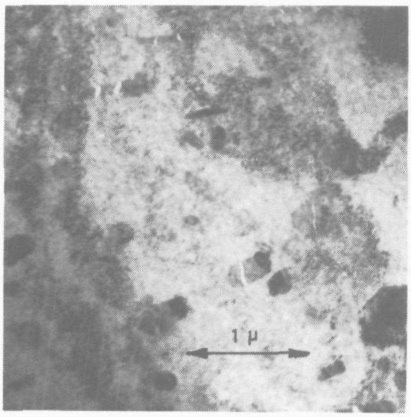

(b) 7079 material

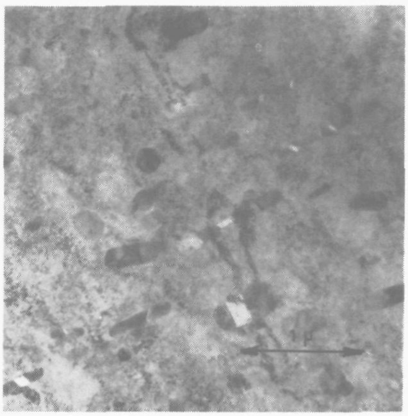

(c) 7079 material

Fig. 29. Dislocation clusters and pile-ups at inclusions.

TABLE 2. Relation between stress and strain and inclusion parameters

Material	$\sigma_{0.2}$ (kg/mm^2)	σ_u (kg/mm^2)	m	σ_f (kg/mm^2)	ε_f	a (microns)	s (microns)	f
2014	43.2	47.9	0.060	61.5	0.25	0.087	0.209	0.038
2024(Pb, Bi)	30.5	37.4	0.077	55.2	0.39	0.205	0.635	0.018
2024 Clean	34.2	46.6	0.221	70.9	0.42	0.196	0.323	0.116
2024(1)	37.1	48.5	0.100	73.8	0.42	0.199	0.213	0.053
2024(2)	29.8	43.3	0.124	64.6	0.40	0.126	0.290	0.044
2024(3)	36.0	49.3	0.109	60.2	0.20	0.138	0.359	0.030
3003	15.5	16.5	0.036	33.2	0.70	0.086	0.405	0.005
6061	17.8	26.1	0.249	41.3	0.46	0.076	0.320	0.007
6151	26.8	30.9	0.058	51.4	0.51	0.036	0.357	0.001
7075(1)	50.0	54.7	0.058	80.0	0.38	0.124	0.185	0.158
7075(2)	9.3	21.1	0.226	28.2	0.29	0.133	0.229	0.102
7075(3)	50.9	56.4	0.051	71.0	0.23	0.095	0.190	0.065
7079	29.8	47.4	0.148	63.6	0.29	0.124	0.225	0.088
SAP 895	21.0	32.6	0.140		0.12			0.090

cross slip is easily possible in aluminium alloys and consequently relaxation can occur by cross slip also. As a result of plastic relaxation no large pile-up will be formed in one slip plane and an irregular distribution of dislocations must be expected in the way shown schematically in fig. 25f. As support for this argument clusters of dislocations around particles can be observed in fig. 29.

None of the equations for void coalescence may be expected to give reliable quantitative predictions. Therefore, the test results will only be checked to see whether they follow the trends predicted by the equations. A quantitative check can be carried out by using the results of the tensile tests. The ratio between the moduli of the particles and the matrix then plays a role. Different materials with various kinds of particles of unknown moduli have to be considered, but there is no other choice than to assume that the particles have the same average modulus in all materials. Probably this is not a real shortcoming since the modulus effect is obscured if the material contains various constituents. Besides, all materials contained more or less the same alloying elements, though in different amounts.

The theories can be appraised by checking the relation between ε_f (true fracture strain), σ_f (true fracture stress) and a, s and f. The particle size a, the particle distance s and the volume fraction f were determined from the electron micrographs of the foils by applying the relations derived in the appendix (sect. 10, 9).

The results are given in Table 2. It appears from these data that neither

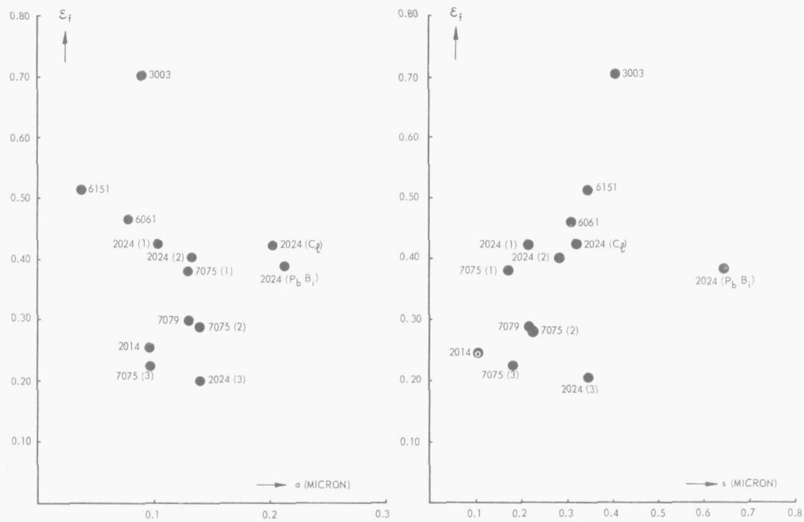

Fig. 30. Plots of fracture strain *versus* particle size and particle spacing.

fracture stress nor fracture strain depends solely on particle size or particle distance. This is also shown in fig. 30, where the fracture strain is plotted *versus* particle size and particle distance. Table 2 also indicates that an unambiguous correlation between the volume fraction of particles and the fracture stress, as predicted by Thomason, does not exist. On the other hand the values of ε_f plotted *versus* f in fig. 31 indicate that there seems to be a relation between the fracture strain and the volume fraction. This gives some support to the formula presented by Gurland and Plateau. Eq. (38) as given by McClintock predicts that $\varepsilon_f/(1-m)$ should be a function of the volume fraction. This relation is plotted in fig. 32, showing that it is reasonably satisfied by the test results.

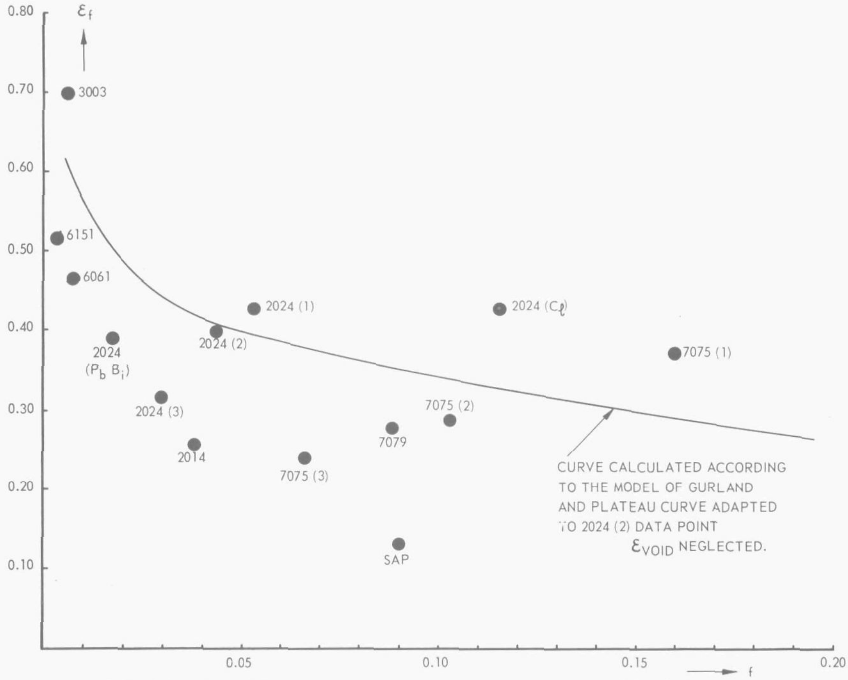

Fig. 31. Plot of fracture strain *versus* volume fraction of inclusions.

In order to check eq. (53), the result of the present model, the value of σ_i/σ_f has to be estimated first. The stress σ_i is the stress to move a dislocation in a single crystal. According to Friedel [38] this stress is roughly equal to one third of the yield stress of a polycrystal. When using this approximation the value of σ_i/σ_f for the present materials fall roughly into two groups (with one exception). For one group $\sigma_i/\sigma_f \simeq 0.22$, for the other one $\sigma_i/\sigma_f \simeq 0.16$. The measured values of ε_f/σ_f are plotted *versus* f

in fig. 33. Two curves are drawn giving the relation predicted by eq. (53) for the two values of σ_i/σ_f. (The constant C in eq. (53) was found by using one of the data points).

Fig. 33 shows that the present model is reasonably obeyed by test results. A rigourous agreement might not be expected because:

1. The model could be evaluated for the two-dimensional case with screw dislocations only.
2. The effect of different moduli of particles could not be accounted for.
3. The effect of particle shape could not be accounted for.

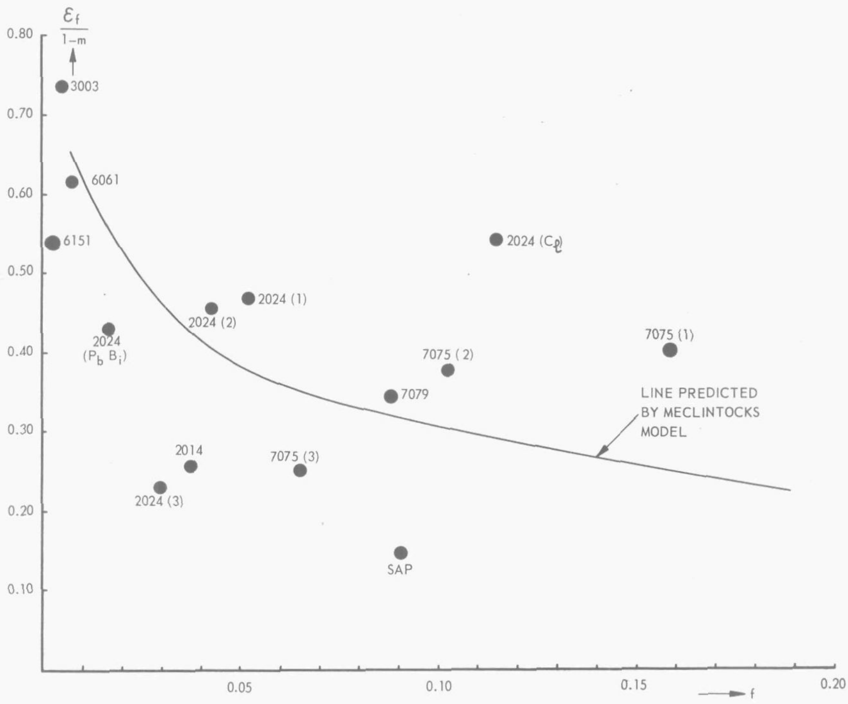

Fig. 32. Check of McClintocks model.

4. The error in determination of the volume fraction of particles may be rather large.
5. As pointed out already in sect. 6.1 premature fracture of large inclusions is not essential for fracture, but a cracked inclusion will give rise to a strain concentration and hence affect the macroscopic fracture strain. The macroscopic fracture strain had to be used in fig. 33 because the microscopic strain is unknown.

In conclusion it can be stated that the test results are in satisfactory agreement with the present fracture model.

The data point of SAP 895 in the previous figures pertains to a dispersion hardened material with flake-like dispersed particles. The different appearance of this material can be seen in fig. 34a, b. Edelson and Baldwin [48] have extensively studied the ductility of dispersion hardened copper alloys. They observed that fracture strain is a function of volume fraction

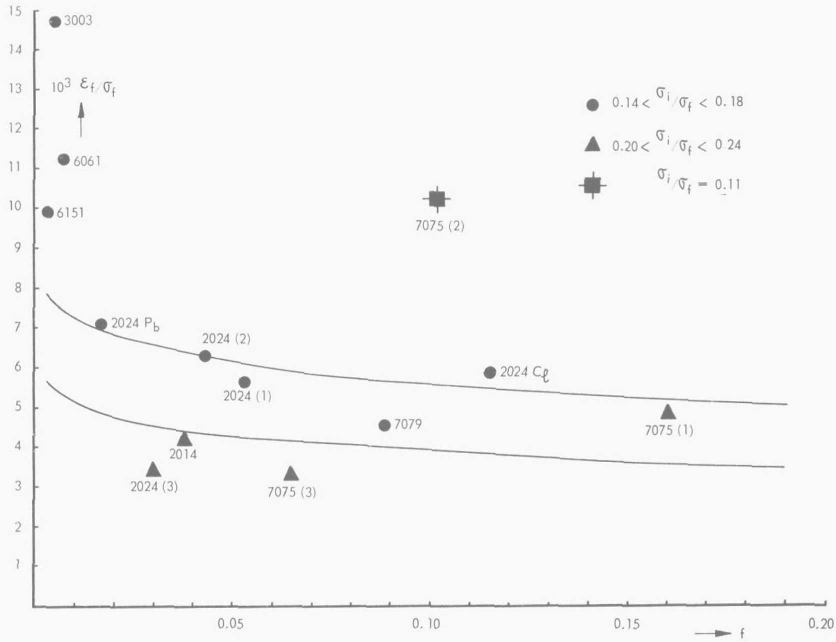

Fig. 33. Fracture properties as compared with curves predicted by the present fracture model.

solely. Their results are presented here in fig. 34c. Contrary to the precipitation hardened materials presently studied, the dispersion hardened materials investigated by Edelson and Baldwin show an effect of particles on the strain hardening exponent and the yield strength. Edelson and Baldwin showed that, indeed, the yield strength was controlled by the mean free path between the particles, in agreement with the theory for dispersion hardening put forward by Orowan [49]. They further observed the strain hardening exponent to depend upon f solely.

As has been noted earlier one may expect a different behaviour of dispersion hardened alloys, where voids might be initiated rather early at the poles of the particles instead of the equator and where void coalescence then becomes the critical condition. The results of Edelson and Baldwin fit the model of McClintock, which is likely for dispersion hardened alloys.

Other literature data useful for the present purpose are very scarce. Schiller and Schneiders [50] report an increased fracture strain, primarily resulting from smaller particles, but again for a dispersion hardened SAP

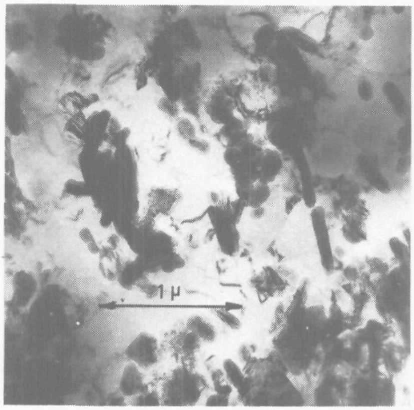

(a) Oxide particles in SAP.

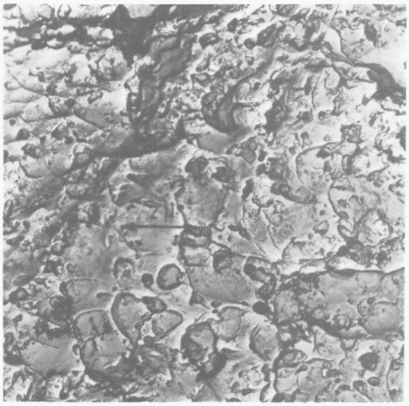

(b) Dimples in fracture of SAP.

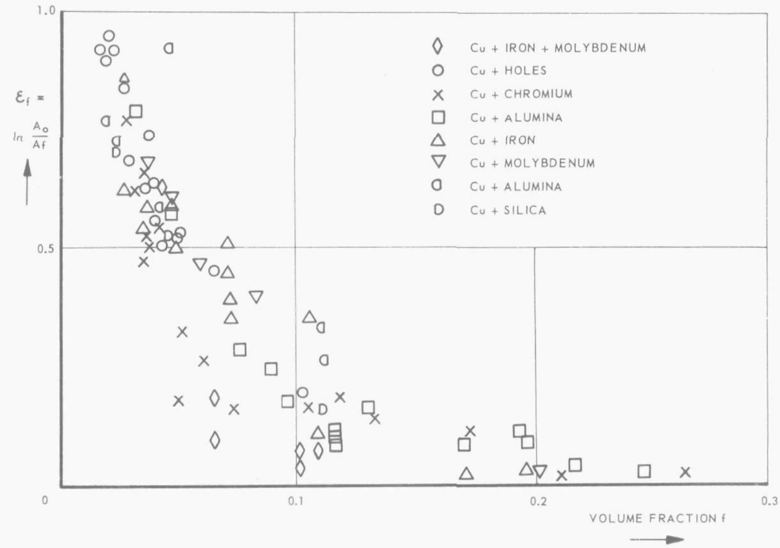

(c) Test results of Edelson and Baldwin [48] on dispersion strengthened copper.

Fig. 34. Results of dispersion strengthened materials.

TABLE 3. Results of tests on brass specimens with randomly distributed holes

Type of specimen	Number of holes	Hole size a (mm)	Hole distance s (mm)	$s-a$ (mm)	Volume fraction	Nominal stresses (holes ignored)		$\varepsilon_{f\,\mathrm{true}}=n(1+\varepsilon_{\mathrm{eng}})^{\star}=$	$\sigma_f=\sigma_u(1+\varepsilon_{\mathrm{eng}})$
						$\sigma_{0.2}$ kg/mm^2	σ_u kg/mm^2	$\ln\left(1+\dfrac{a-a_0}{a_0}\right)$	
A	50	11	4.5	3.5	0.0393	25.1	29.7	0.53	50.4
		1.5		3	0.0885	18.5	22.4	0.32	30.7
		2		2.5	0.1572	14.3	17.5	0.28	23.1
B	25	1	6.3	5.3	0.0196	27.0	33.8	0.62	62.5
		1.5		4.8	0.0442	23.2	28.7	0.32	39.3
		2		4.3	0.0784	18.9	23.5	0.32	32.4
C	37	1	5.2	4.2	0.0292	25.7	32.5	0.44	50.4
		1.5		3.7	0.0725	22.3	27.8	0.41	40.9
		2		3.2	0.1168	18.6	22.6	0.37	32.7
D	18	1.5	7.4	5.9	0.0354	24.1	30.1	0.34	42.1
		2		5.4	0.0564	21.6	26.4	0.20	32.2
		2.5		4.9	0.0885	17.7	22.1	0.39	32.2
E	No holes	0		0	0	31.2	41.2	0.50	68.0

* The fracture strain was practically indeterminable. Therefore the test was stopped as the first crack occurred. The $\varepsilon_{\mathrm{eng}}$ was determined as the instantaneous hole diameter at the crack minus original diameter devided by original diameter.

alloy. The results of Birkle *et al.* (51) seem to indicate an increasing fracture strain with decreasing sulphur content of a low-alloyed steel; in that case, however, it should be kept in mind that steel contains also carbide particles and probably many other constituents.

The results of the present tests on brass specimens with randomly distributed holes have still to be considered, although they are of limited

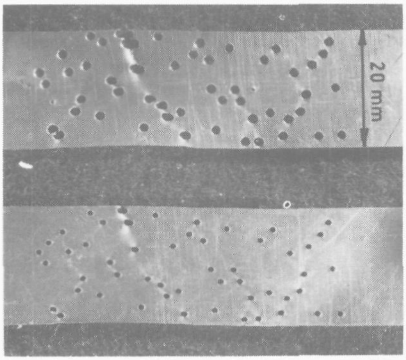

(a) Specimens just prior to fracture.

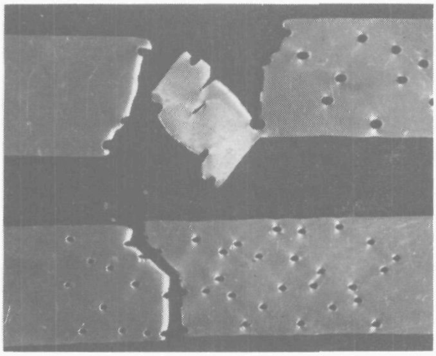

(b) Specimens after fracture.

Fig. 35. Examples of perforated brass specimens prior and after fracture. (Note hole rotation and hole closure).

value for the present discussion. Experimental details are presented in the appendix. Fig. 35 shows some specimens just prior to fracture. At some places rotation of the holes can be observed in accordance with the model of McClintock, but generally void rotation did not occur because of the action of two shear bands perpendicular to each other. The test results are collected in Table 3. The fracture properties are plotted as a function

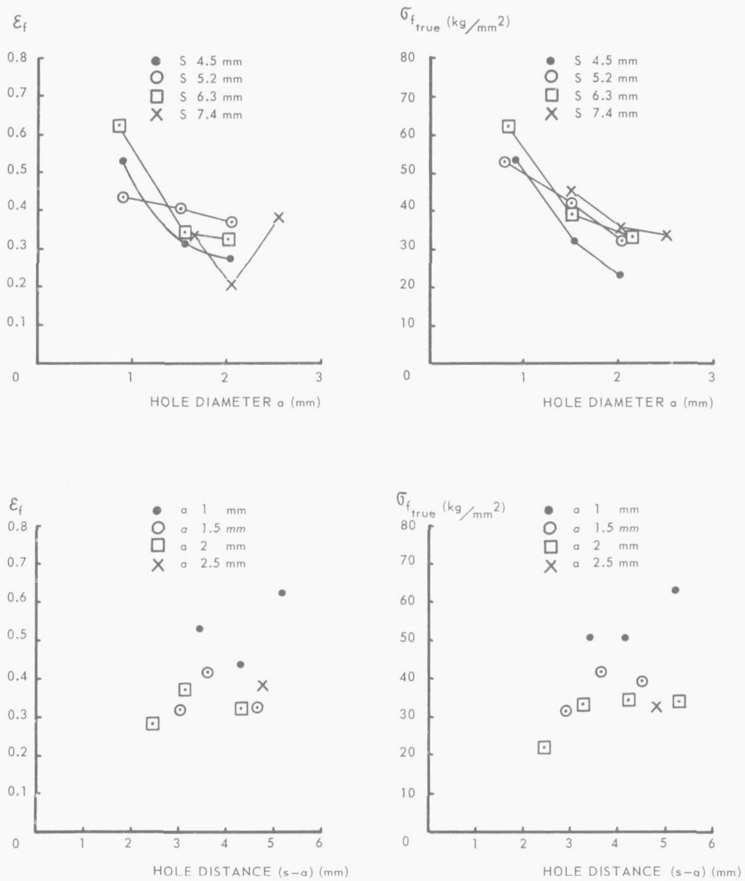

Fig. 36. Variation of fracture properties with hole size and spacing. (Brass specimens with randomly distributed holes).

of hole diameter and hole spacing in fig. 36, showing that fracture is not controlled by one of these parameters. However, fig. 37 suggests that the fracture properties depend only on the hole fraction. The results are more interesting for dispersion hardened metals than for precipitation hardened metals, because the holes are pre-existing voids instead of semi-coherent inclusions.

6.4 *Ductility and the fracture condition*

From the foregoing discussion and test results it may be concluded that either void initiation or void coalescence may be the critical event in fracture. In case of dispersion hardened materials, which are supposed

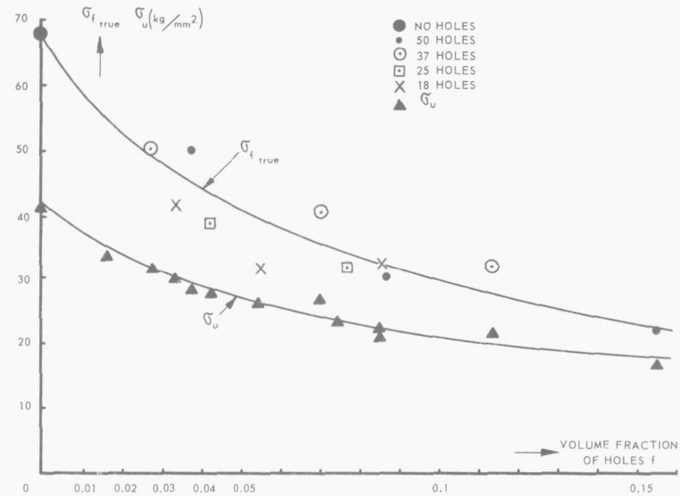

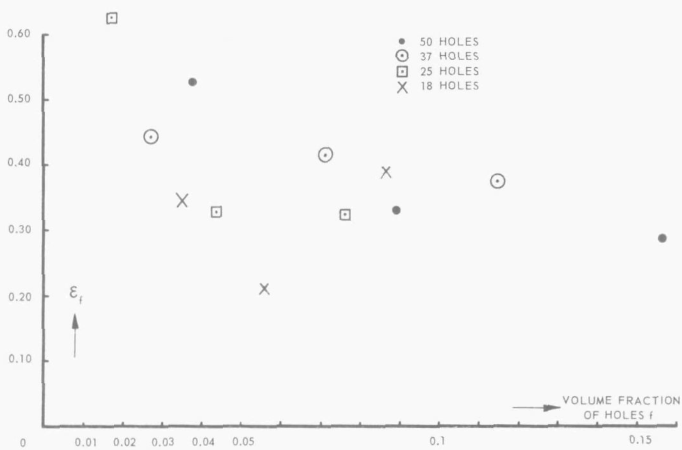

Fig. 37. Variation of fracture properties with volume fraction of holes.

to exhibit a relatively low degree of cohesion with the foreign particles, it is believed that void coalescence is the critical event. At a certain strain voids can be initiated at the pole of the particle as a result of the high stress concentration, while fracture is still remote. This is very similar to the initiation of voids at large inclusions at low strains as shown in fig. 1. Straining can go on until finally the condition for coalescence is fulfilled and fracture occurs. This mechanism is compatible with the models of McClintock and Thomason and it is supported by the experimental evidence of void initiation and growth at these particles.

In the more common materials the particles that must initiate voids are intermetallic constituents, which are supposed to possess some ductility and to possess large bonding forces with the matrix. In some cases premature voids may be initiated as a result of the fracture of elongated particles. Generally, however, voids are supposed to occur at the equator of a particle as a result of dislocations piling up against the particle. This void initiation is followed by spontaneous void growth, i.e. void initiation is the critical event in fracture of these materials. Such a model predicts fracture to depend solely on the volume fraction f of the particles, which is in agreement with test results. There are many indirect indications that voids are initiated at these particles, so that the lack of evidence of actual voids is compatible with the concept of spontaneous void growth. The mechanism of fracture on a microscale is progressive slip, as shown for the two-dimensional case in fig. 26. This implies that void coalescence is an unstable process. However, at a sharp decrease of the active stress, which may occur in a very hard tensile machine, the process can apparently be stopped, as indicated by the experiments of Bluhm and Morressey [31] and many others.

The question now arises: what determines the ductility and the strength of a material? An increase of the yield strength of a material generally implies an increase of the tensile strength. It has become clear from the present discussion that a certain amount of straining is required before fracture by void initiation and coalescence can occur. Consequently, straining is terminated by the initiation of voids.

The strength of a material from an engineering point of view is the ultimate tensile strength σ_u, i.e. the stress at maximum load. The major amount of straining occurs during necking after the maximum load is reached. If severe necking can develop, the difference between fracture stress and ultimate tensile strength will be very large. In the literature it is often assumed that necking will commence at the moment voids are initiated. This cannot be true for the following reasons:

(a) Voids at large inclusions can be initiated long before necking.

(b) In extremely pure material necking is generally very pronounced.

(c) Under hydrostatic pressure necking is more pronounced.

Necking must be governed by stresses and strains rather than by structural parameters. Although in some cases unusual stress-strain curves have been observed [52, 53], necking must be considered as a plastic instability, which has nothing to do with voids. The failure to detect voids in foils made from severely necked specimens supports this point of view.

During necking, straining will be concentrated in a small region and will progressively proceed until at ε_f void initiation and coalescence occurs. This implies that ductility is controlled by the volume fraction of the inclusions. On the other hand, the engineering strength is determined by maximum load. Maximum load can easily be shown to occur at $\varepsilon_{true} = m$. Further, there are the relations $\varepsilon_{true} = \ln(1 + \varepsilon_{eng})$ and $\sigma_{true} = \sigma_{eng} e^{\varepsilon_{true}}$, the subscript eng. meaning engineering. Hence, at maximum load

$$\sigma_{true} = \frac{P_{max}}{A_o} \frac{A_o}{A} = \sigma_u e^m \tag{54}$$

or with

$$\sigma_{true} = \sigma_0 \varepsilon_{true}^m \quad \text{and} \quad \varepsilon_{true} = m\,, \tag{55}$$

$$\sigma_u = \sigma_0 m^m e^{-m} = \sigma_{0.2} \cdot 0.002^m m^m e^{-m}\,. \tag{56}$$

if it is assumed that the relation $\sigma = \sigma_0 \varepsilon^m$ still holds in the region of very low plastic strains. Apart from this it is clear, however, that σ_0 and the yield stress will be governed by the same parameters.

According to eq. (56) the engineering strength depends on the yield strength and on m. Both $\sigma_{0.2}$ and m are governed by the state of precipitation rather than by inclusions, implying that the engineering strength is not affected by the inclusions.

Further complicating factors are strain rate and hydrostatic stresses. The effect of hydrostatic tension can be appreciated from the model of McClintock, using eq. (38). Thomason has also incorporated the effect of hydrostatic stresses in his model.

CHAPTER 7

FRACTURE SURFACE TOPOGRAPHY

The results on the micro-topography of ductile fracture surfaces revealed some interesting points, which deserve discussion because they are relevant to the fracture process.

Plenty of evidence can be presented to prove that dimples are initiated at tiny inclusions, the prints of which are often visible in the dimples (figs 3, 10, 22). It has been proposed that for the material studied in this investigation void growth occurs primarily perpendicular to the tensile stress, rather than in the direction of the tensile stress. Experimental evidence for this is twofold: (1) the dimples are very shallow holes and (2) no imprint of the inclusion would be visible in the dimple if the void had grown in the direction of the tensile stress, because deformations would have annihilated this print.

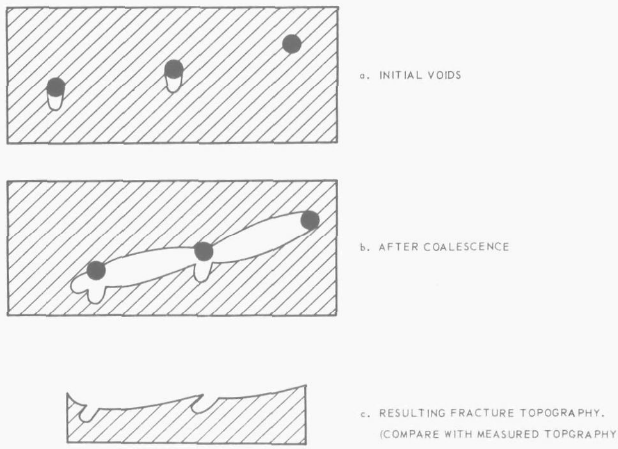

Fig. 38. Explanation of formation of tips at dimples.

On the other hand, it was stated that voids sometimes occur at the poles of spherical particles and then grow a little in the direction of tensile stress before coalescence occurs perpendicular to this growth. This mechanism is shown schematically in fig. 38, indicating that the initial void would leave a kind of elongated tip at the dimple. It is thought that the tips visible at the dimples in fig. 39 are examples of this phenomenon. Due to

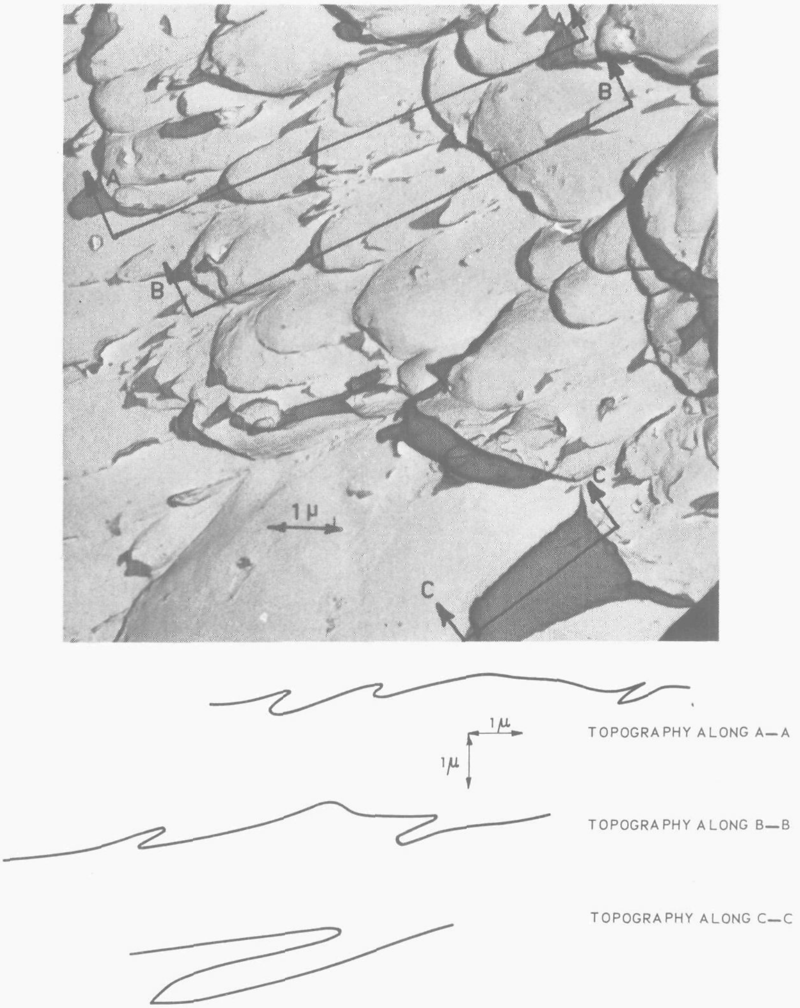

Fig. 41. Topography of tips of dimples. 6061 material.

cracking of large inclusions (figs 1, 2) where large voids will attract the fracture path and induce appreciable deviations from the fracture plane. Topographic measurements on matching fracture surfaces give a good impression of the fracture surface roughness on a larger scale. This is demonstrated in fig. 42.

Fig. 42 deserves some further attention. The big inclusion A in the middle has fractured by cleavage and has introduced a rather large dimple. As satellites around this big dimple there are four middle-size dimples B, C,

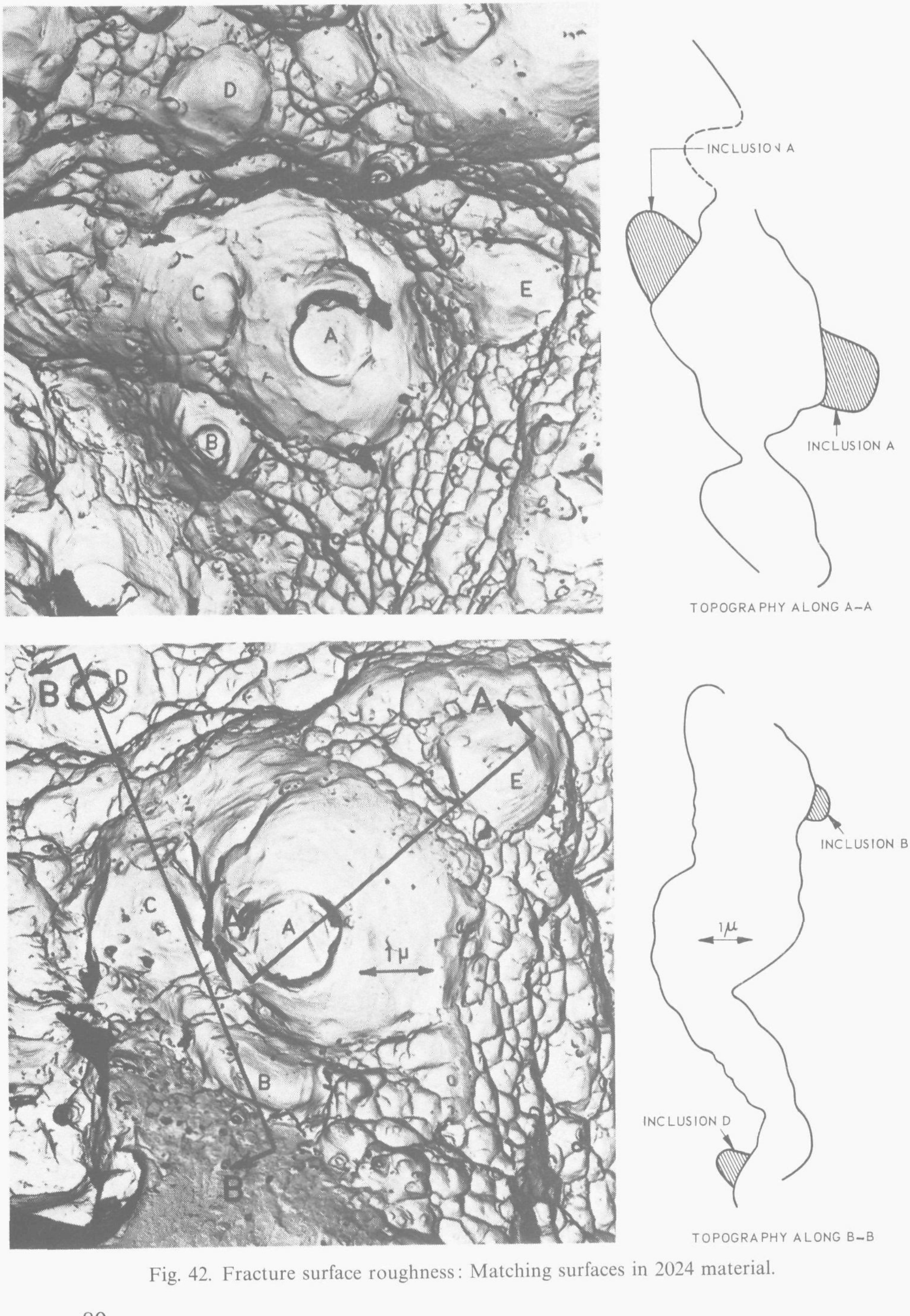

Fig. 42. Fracture surface roughness: Matching surfaces in 2024 material.

D, E. Two of them, B and D, show the print of an inclusion on one fracture surface and not on the other. It is felt that this is caused by an interface failure along the inclusion, the particle stayed in one fracture surface and is still visible there, whereas the imprint in the matching dimple has been extinguished by plastic deformations.

The topographic measurement and such examples as fig. 39 have shown how essential it is to tilt the replicas in the electron microscope. Quick tilting during observation (possible if the tilt axis exactly intersects the optical axis, so that the image does not move) gives the observer an immediate three-dimensional impression of the fracture surface. Tilting also reveals the difference between the various kinds of dimples, namely: shear dimples, tear dimples and tensile (or equi-axed) dimples. These dimples are illustrated schematically in fig. 43. The model of their forma-

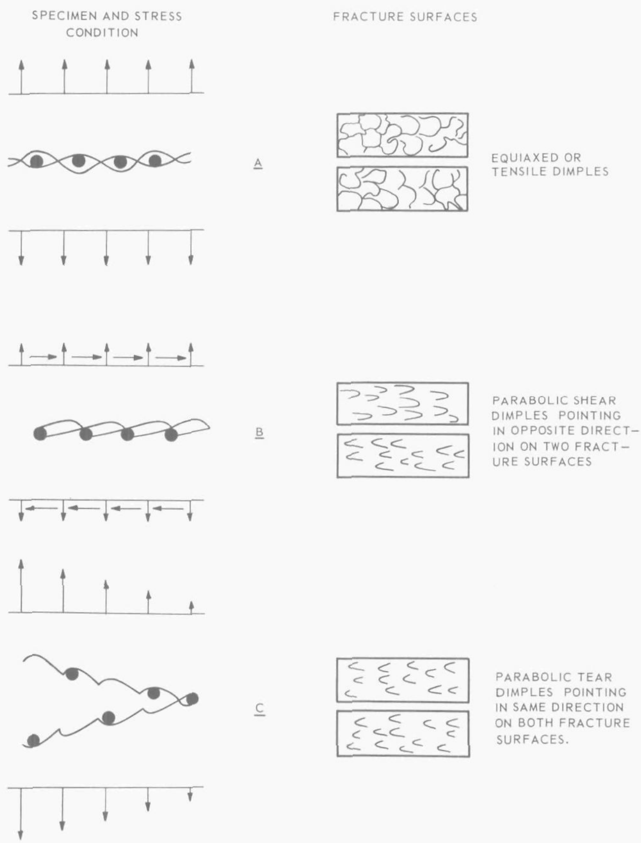

Fig. 43. Equi-axed, shear and tear dimples.

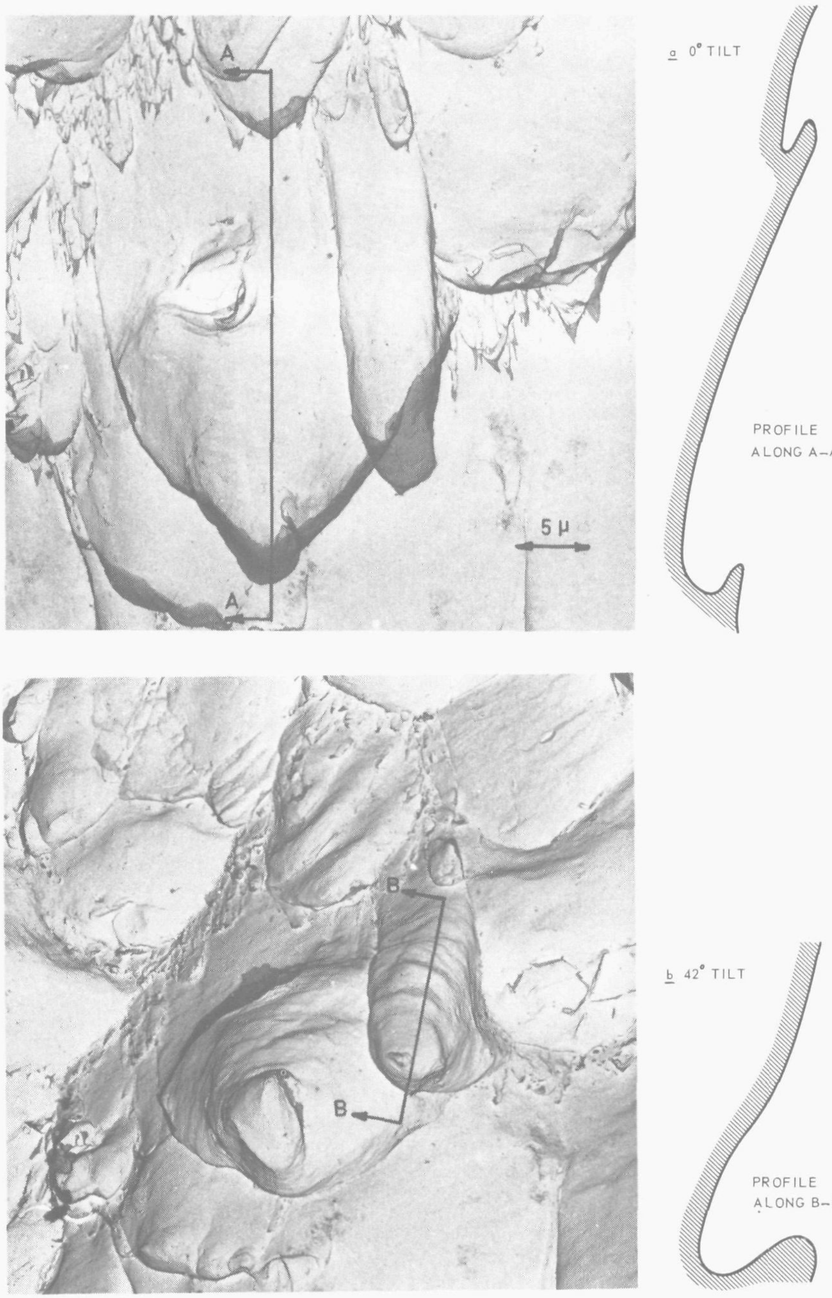

Fig. 44. Change of shear dimples into equi-axed dimples after tilting. 6061 material, shear fracture.

tion was first proposed by Rogers [5] and later by Crussard *et al.* [6] and Beachem [54]. The tilting experiments of Broek [55] have thrown a new light on this subject. At certain tilt angles shear dimples will look like equi-axed dimples, as in fig. 44, and *vice versa*, as in fig. 45.

The examples shown in figs 44 and 45 indicate a possible source of confusion. The topography of a replica may be such that parts under observation are at a large angle with the optical axis; this may result in a misinterpretation of dimple types. Tilting is required before a distinction can be made. Besides, dimples of various types can exist close to each

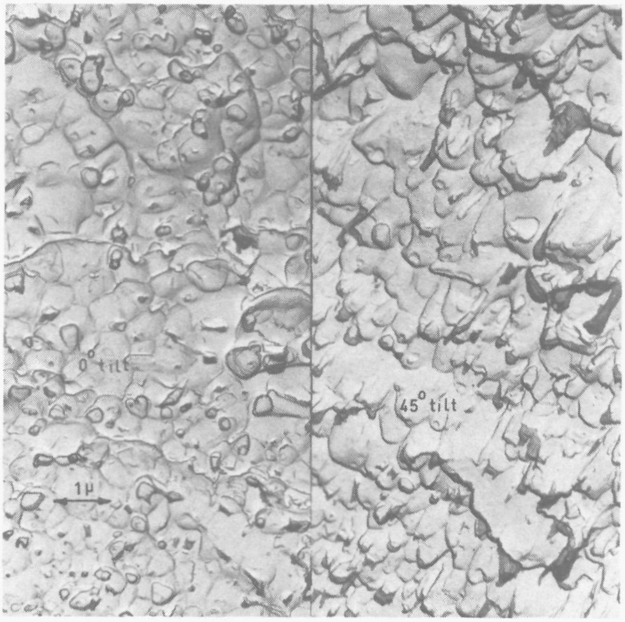

Fig. 45. Equi-axed dimples changing into shear dimples after tilting. Tensile fracture mode in 7079 material.

other. Also the size of the dimples may locally vary as was shown already in fig. 3 and now, for example, in fig. 44. This is a result of the irregular distribution of the inclusions in the material, as can be seen in the micrographs in fig. 46. Thus it may be misleading to illustrate differences in fracture surfaces of various materials with one micrograph of each condition, as sometimes happens in the literature. Apparently more images taken at various tilt angles are required.

The tilt experiments have restored faith in carbon replicas, which were subject to doubt. Besides, it was shown previously [55] that successive

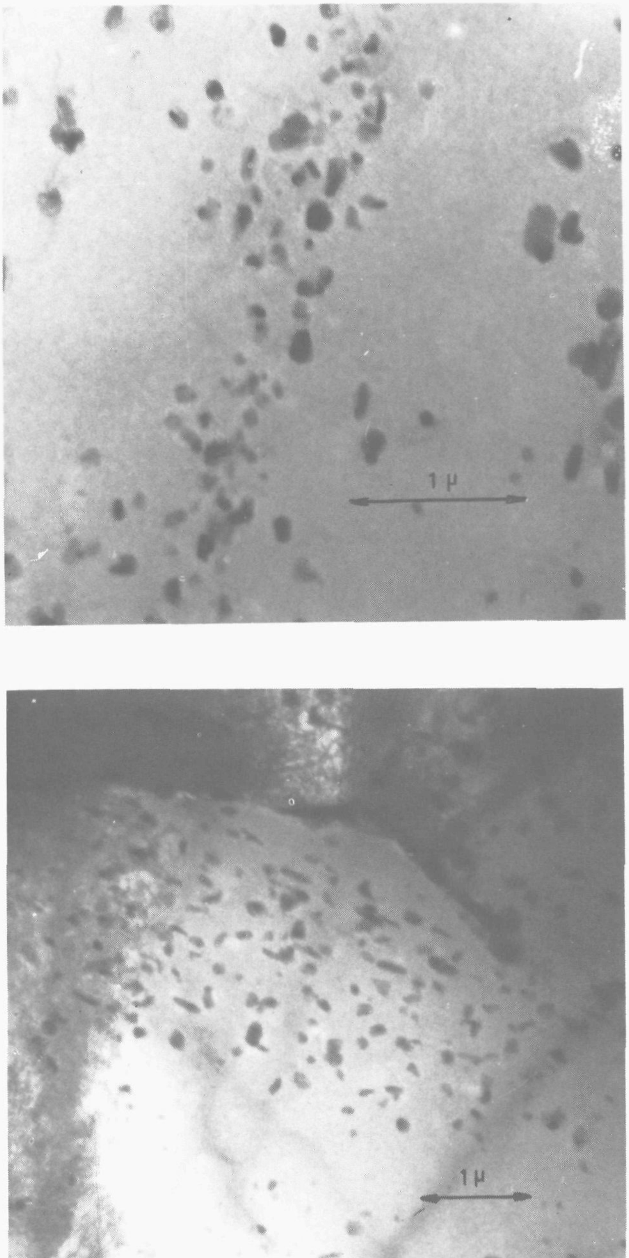

Fig. 46. Irregular distribution of inclusions. 7079 material.

CHAPTER 8

APPLICATION TO FRACTURE TOUGHNESS PROBLEMS

8.1 *Relation between fracture toughness and inclusions*

Several investigators have tried to derive a relation between the fracture toughness and other mechanical properties of the material, e.g. Rosenfield and Hahn [56], Krafft [57, 58], Williams and Turner [59] and Malkin and Tetelman [60]. Such relations may be illuminating, but they are of little practical importance,since it is more realistic to carry out fracture toughness tests to obtain a fracture toughness value, than to perform a normal tensile test and compute the fracture toughness value. If on the other hand fracture toughness could be correlated with the microstructure the result would be of importance, because it would show the metallurgist how to improve the toughness.

A correlation with micro-structural properties was achieved by Malkin and Tetelman [60] for the cleavage type of fracture, which occurs at a critical stress. The present discussion will be restricted to ductile dimple fracture, which occurs at a critical strain. Rosenfield and Hahn [56] used the relation for crack opening displacement c_o in following an analysis by Dugdale [61]: c_o is given by

$$c_o = \frac{2\sigma_y l}{\pi E} \ln \sec \frac{\pi\sigma}{2\sigma_y} \tag{57}$$

where σ_y is the yield stress, σ the nominal applied stress and l the semi-crack length. At low stress levels, i.e. $\sigma/\sigma_y < 0.7$, the factor ln sec $\pi\sigma/2\sigma_y$ can be approximated by $\pi^2\sigma^2/8\sigma_y^2$. With the stress intensity factor K $(=\sigma\sqrt{\pi l})$ eq. (72) then changes into

$$c_o = \frac{\sigma_y}{4E}\left(\frac{K}{\sigma_y}\right)^2 . \tag{58}$$

Rosenfield and Hahn further note that the regions of shear at the crack tip overlap, the width of the overlap being denoted by λ, as in fig. 48. Hence, the shear strain at the crack tip can be approximated by $\gamma = c_o/2\lambda$ (fig. 46). The average tensile strain in the region of overlap is $\bar{\varepsilon} = \beta c_o/\lambda$, and the maximum strain is

$$\varepsilon_{max} = \alpha \cdot c_o/\lambda . \tag{59}$$

Rosenfield and Hahn assume fracture to take place when the maximum

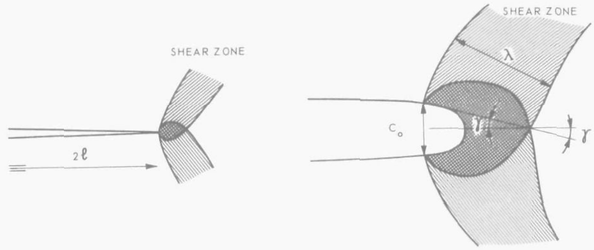

Fig. 48. Shear zones at crack tip before and after crack opening (according to Rosenfield and Hahn). Compare with shear zones in fig. 53.

strain at the crack tip exceeds the true fracture strain as measured in a tensile test. Then combination of eqs (58) and (59) gives

$$K_{Ic} = (4\alpha\lambda\varepsilon_{\text{true}} E\sigma_y)^{\frac{1}{2}} . \qquad (60)$$

Rosenfield and Hahn argue that $\alpha \simeq \frac{1}{6}$. From measurements of λ they decide that λ is proportional to m^2 (strain hardening exponent).

Consequently,

$$K_{Ic} = (\tfrac{2}{3}\varepsilon_{\text{true}} m^2 E\sigma_y)^{\frac{1}{2}} . \qquad (61)$$

Rosenfield and Hahn showed that their expression was accurate within about 30% for eleven different materials (Al-alloys, Ti-alloys and steels). Krafft [57, 58] assumes that the elastic strain distribution is valid near the crack tip, i.e.

$$\varepsilon_y = \frac{\sigma}{E}\sqrt{\frac{l}{2r}} = \frac{K}{E\sqrt{2\pi r}}$$

where r is the distance from the crack tip. If there is an inclusion at a distance s from the crack tip, the crack will proceed to the inclusion if the strain at a distance s equals the critical strain for necking. This strain can easily be shown to be $\varepsilon_{\text{true}} = m$. This means that fracture occurs if $\varepsilon_y = m = K_{Ic}/E\sqrt{2\pi s}$, or

$$K_{Ic} = E(2\pi m^2 s)^{\frac{1}{2}} . \qquad (63)$$

This equation is very similar to eq. (61). The equation derived by Williams and Turner [59] is also of this form. Actually, Krafft did not use the inclusion distance but what he calls ligament spacing d_T, where d_T is the width of an element ahead of the crack tip in which necking instability occurs.

The present investigation gives a possibility to derive a relation between fracture toughness and structural parameters. The analysis must be confined to plane strain fracture toughness, because plane stress presents many additional problems, as has become clear from previous work [62, 63]. The model developed in chapter 6 for void coalescence predicts a fracture strain of (if m is neglected in comparison to 1)

$$\varepsilon_f = C \frac{\sigma_o}{\mu} \left\{ \varphi_1(f) - \frac{\sigma_i}{\sigma_f} \varphi_2(f) \right\}.$$

The strain at a distance r from the crack tip is given by

$$\varepsilon(r) = \frac{\sigma}{E} \sqrt{\frac{\pi l}{2\pi r}} = \frac{K}{E} \frac{1}{\sqrt{2\pi r}},$$

if it is assumed (as in the model by Krafft) that the strain distribution can still be reasonably predicted by the elastic solution, despite plastic deformation. The first inclusion will be at a distance s from the crack tip; hence fracture may be expected to occur if the strain $\varepsilon(r=s)$ exceeds ε_f, i.e.

$$\frac{K}{E} \frac{1}{\sqrt{2\pi s}} = C \frac{\sigma_o}{\mu} \left\{ \varphi_1(f) - \frac{\sigma_i}{\sigma_f} \varphi_2(f) \right\}$$

or

$$K_{Ic} = 2(1+\nu)\,\sigma_o \sqrt{2\pi s} \left\{ \varphi_1(f) - \frac{\sigma_i}{\sigma_f} \varphi_2(f) \right\}. \tag{64}$$

Eq. (64) can be simplified a little by noting that for the aluminium alloys considered σ_i/σ_f is always close to 0.2. According to fig. 27, for $\sigma_i/\sigma_f = 0.2$ the following relation holds within a few percent:

$$\varphi_1(f) - 0.2\varphi_2(f) = 0.525 f^{-\frac{1}{3}}. \tag{65}$$

Substitution of eq. (65) in eq. (64) results in

$$K_{Ic} = \alpha f^{-\frac{1}{3}} \sigma_o \sqrt{s}. \tag{66}$$

Further refinements of the derivation could be obtained by applying the corrected expression for the stress intensity factor, as derived by Tamate [64]. Tamate analysed the effect of a circular inclusion ahead of the crack tip on the stress intensity factor. If the crack is large with respect to the inclusion the effect is small, as might be expected.

Eq. (66) predicts that the fracture toughness does not depend only on volume fraction of particles, but also on the particle spacing. It implies that for a particular value of f the material with the largest particles will show the highest toughness.

It would be worthwhile to carry out an experimental check of eq. (66)

by determining the fracture toughness of various materials together with the inclusion distribution. Such a check cannot yet be made; fracture toughness values could not be determined for most of the present materials, because heavy sections are required for fracture toughness tests, whereas most materials were sheet or bar. Fracture toughness specimens could only be made of two materials, namely 2024(3) and 7075(3), which were both in the form of thick plate. Fracture toughness specimens of the single-edge-cracked type were made. They had a thickness of 30 mm, a width of 120 mm and a length of 400 mm. They were fatigue cracked until the crack had a length of about 40 mm. The results of the tests are given in the table below.

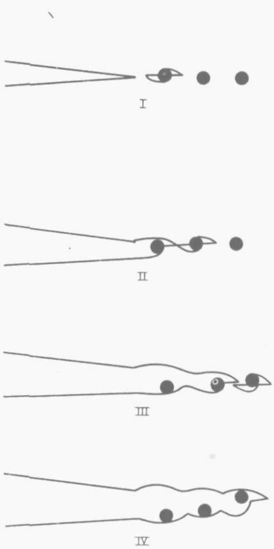

(a)

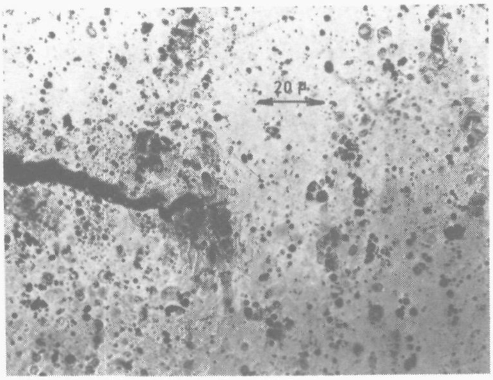

(b) Slowly propagating crack.

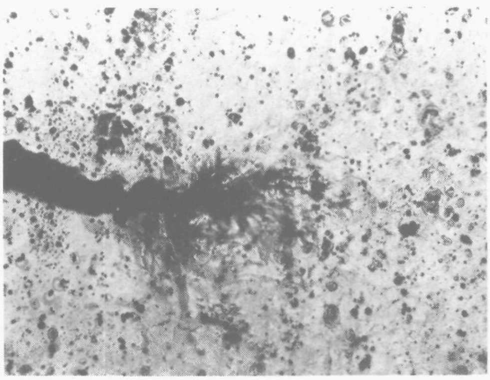

(c) As figure (b), but later stage.

Fig. 49. Crack propagation by void initiation and coalescence.

7075 (3) $K_{Ic} = 104$ kg/mm$^{\frac{3}{2}}$ $K_{Ic}/\alpha = 45.7$ kg/mm$^{\frac{3}{2}}$, calculated
108 kg/mm$^{\frac{3}{2}}$ with eq. (66)
2024 (3) $K_{Ic} = 183$ kg/mm$^{\frac{3}{2}}$ $K_{Ic}/\alpha = 59.3$ kg/mm$^{\frac{3}{2}}$, calculated
166 kg/mm$^{\frac{3}{2}}$ with eq. (66)
173 kg/mm$^{\frac{3}{2}}$

The data indicate that for $\alpha = 2.32$ the right value would be predicted for 7075(3) and $K_{Ic} = 137$ kg/mm$^{\frac{3}{2}}$ for 2024(3); i.e. eq. (66) predicts the right tendency of a higher toughness for the aluminium–copper–magnesium alloy, but the predicted ratio between the values for 7075 (3) and 2024 (3) is lower than in reality. However, it might be argued that the specimen dimensions were somewhat too small for a valid K_{Ic} test in the case of the 2024 material, implying that the real fracture toughness of this material may be somewhat lower than that reported here.

8.2 *Crack propagation*

The mechanism of crack propagation by void initiation and coalescence in front of the crack tip is sketched in fig. 49. Since void initiation and coalescence has been found to be a result of slip, it may be expected that fracture occurs in planes of maximum shear stress. This conclusion can be of help in explaining the fracture mode transition, which is the subject of a recent publication [37].

In thin sheets the fracture is entirely of the so called shear type, making an angle of 45° with the sheet surface. Fractures in thicker sheets have a part at mid-thickness which is perpendicular to the sheet surface; the thicker the sheet, the larger the flat tensile part. This is illustrated in fig. 50,

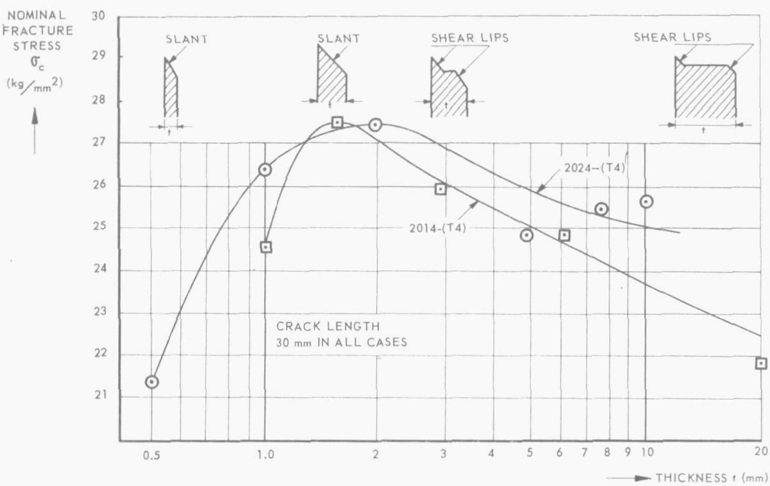

Fig. 50. Fracture mode transition in connection with plate thickness [37].

showing that the fracture mode transition is accompanied by a drop in fracture strength until in very thick plates the real plane strain fracture toughness is attained.

The mode of fracture is related to the state of stress. In plane stress a

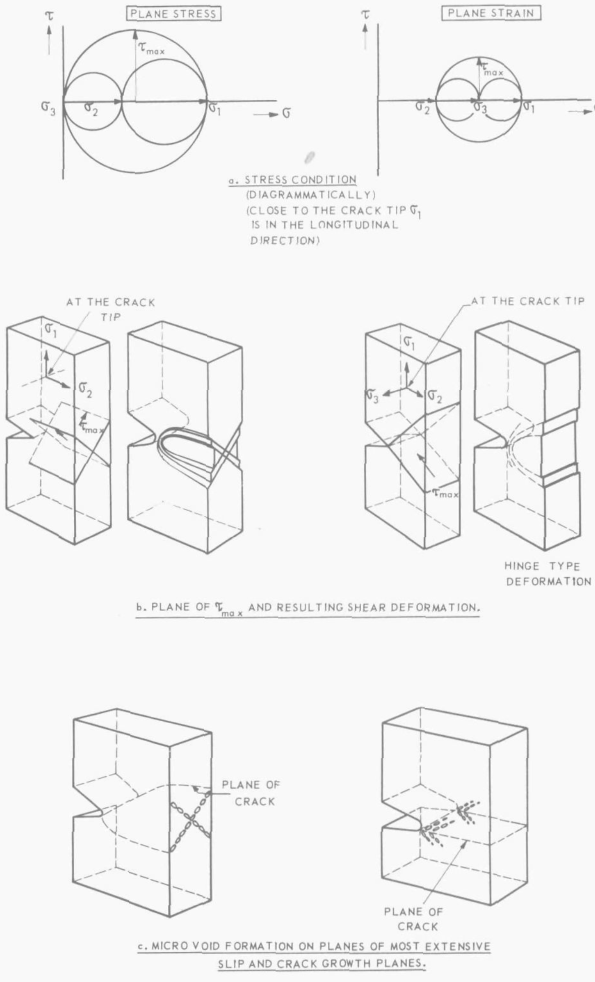

Fig. 51. Slant and square fractures as a result of the state of stress.

slant fracture will occur while in plane strain the fracture is square. In a thick plate yielding in the thickness direction is constrained by the surrounding material. As a result a tensile stress in the thickness direction is built up, giving rise to a triaxial state of stress, which ultimately becomes plane strain. At the sheet surface there is always plane stress because the third principal stress (perpendicular to the surface) cannot exist. Therefore a square fracture always has small slant portions (the shear lips) at the plate surface.

The relation between the fracture mode and the state of stress can be explained as follows. In plane stress the maximum shear stress occurs on planes making angles of 45° with both the sheet surface and the loading direction. In the case of plane strain the planes of maximum shear stress are perpendicular to the sheet surface and make an angle with the crack. This angle is about 70° in the elastic case, as shown by Schijve [65]. This situation is illustrated in fig. 51a, b. Since shear stresses are responsible for the voids, they will lead to void concentrations on different planes in the two cases (fig. 51c), resulting in a square fracture in plane strain and a slant fracture in plane stress. This model has already been discussed previously [37], together with a possible explanation for the higher toughness in plane stress.

8.3 *Crack opening displacement and stretching*

It has been observed earlier [66] that a so called stretched zone is formed at the crack tip in a fracture toughness specimen before final fracture occurs. The stretched region is visible on the electron micrographs of the transition from the fatigue crack to the ductile dimpled fracture surface. The stretched region between the striations and the dimples consists of wavy slip lines, as can be seen from fig. 52. Recently there has been some speculation in the literature as to the significance of these stretched zones. Spitzig [67] proposes that the stretched region is a measure for the process zone or ligament spacing in the model of Krafft, as discussed in section 1 of this chapter. He also concludes that the critical crack opening displacement is equal to the width of the stretched zone and to the ligament spacing. Gerberich and Hemmings [68] decide that this is probably incorrect.

It is considered that the stretched zone is a result of crack blunting, as explained already in ref. 66. The same opinion has been expressed recently in a more complicated way by Griffis and Spretnak [69]. Fig. 53 shows how a fatigue crack blunts before crack extension occurs. A good impression of the shape of the stretched zone can be obtained from the present work: a precisely matching area of the stretched region in fig. 47 was obtained, and by making stereographic measurements the profile of this zone could be determined. The result is shown in fig. 54.

It is clear from the previous discussion that a critical strain is required

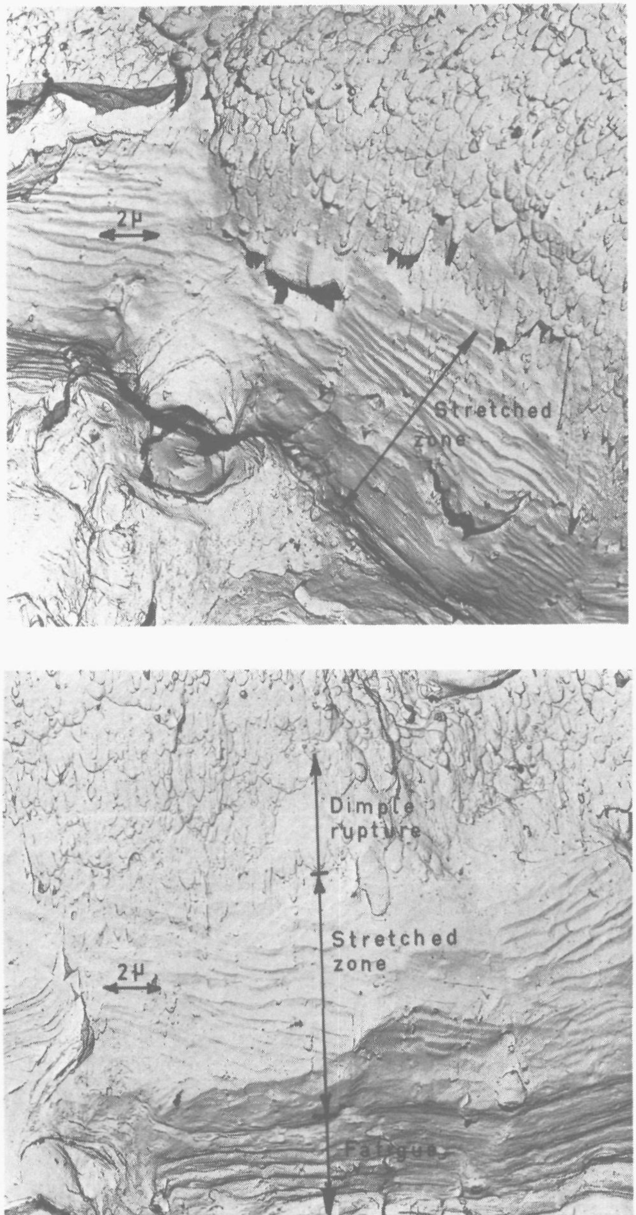

Fig. 52. Stretched regions formed before final failure (region with wavy slip between fatigue striations and dimples). 2024 material.

for void initiation and coalescence. This strain is not reached at the tip of a fatigue crack, otherwise fatigue striations would not be formed. When the critical strain at the crack tip is exceeded, the crack will grow by void coalescence. Due to this straining the crack tip will be opened to c_0 as shown in figs 53 and 54. This implies that crack growth occurs when the crack opening displacement exceeds a critical value, a criterion which is

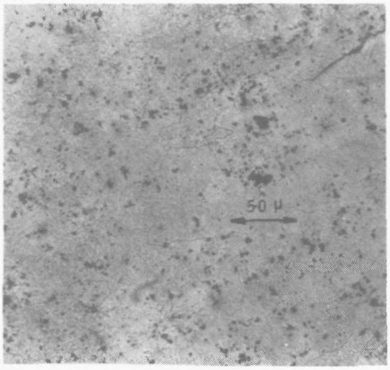

(a) Fatigue crack.

(b) At the onset of crack growth (Note zones of heavy shear deformations).

Fig. 53. Origin of stretched region. 2024 material.

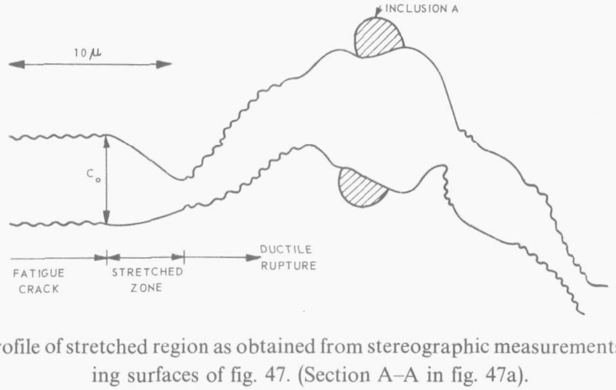

Fig. 54. Profile of stretched region as obtained from stereographic measurements on matching surfaces of fig. 47. (Section A–A in fig. 47a).

already amply used in the practice of fracture toughness testing [70, 71].

In giving an expression for the crack opening displacement eq. (58) also indicates that C_{oIc} must be a constant if K_{Ic} is a material constant. The crack opening displacements measured in figs 53 and 54 and substituted in eq. (58) lead to K values of 90–170 kg/mm$^{\frac{3}{2}}$ for crack initiation, which are the right order of magnitude for 2024-T3 material [37, 62].

CHAPTER 9

PROGRESS MADE IN THE PRESENT INVESTIGATION

At the beginning of this investigation the following picture of ductile static fracture was available. The fracture process starts by the initiation of voids at inclusions and these voids grow until they coalesce. This model was based on the observation of cracked inclusions and voids in sectioned tensile specimens by Puttick [4], Rogers [5] and many others, and on the fact that the fracture surface shows dimples, which were thought to be the halves of the coalesced voids. Later, some evidence was obtained of void initiation at dispersed particles by Palmer and Smith [7], Ansell [8] and Ruedl [9].

From the present investigation it has become clear that fracture of large inclusions visible with the optical microscope, is not essential for the process of ductile fracture. It has been established that voids are indeed initiated at inclusions, but the particles responsible for fracture are of the order of magnitude of a tenth of a micron, i.e. they are not visible with the optical microscope. It was shown that the average dimple size is about the same as the average spacing of these small particles. For the first time void initiation at these small particles was made visible in common aluminium in transmission electron micrographs. Voids resulting from interface decohesion between the matrix and the inclusions and voids induced by the fracture of elongated particles were both observed.

Voids did not occur abundantly, even in regions very close to the fracture surface and in extensively strained materials. This leads to the conclusion that in common materials, with a strong bond between matrix and intermetallic constituent, void initiation is the critical event in fracture. As soon as voids are initiated in any quantity, the condition for coalescence will be fulfilled, leading to immediate fracture. In dispersion strengthened materials void coalescence may be critical and voids may be initiated and grow before fracture.

A dislocation model was developed compatible with this point of view. Dislocation loops pile up against a particle and are repelled by their image force. When the back stress exerted by the pile-up exceeds the repulsive image force, the first loops will be pushed into the interface. If this leads to interface decohesion the pile-up will empty itself into the void, resulting in spontaneous void growth. This model implies that voids are initiated at the equators of the particles rather than at the poles, and that dimples must be shallow holes. The latter suggestion is supported by ample evidence collected in the present investigation.

The dislocation model for fracture was quantitatively evaluated in an approximate way. It predicts that the fracture strain depends on the volume fraction of the particles responsible for fracture. Relations derived on the basis of other fracture models by Thomason [27] and McClintock *et al.* [28] gave similar results. The model was confirmed qualitatively by the present test results. The fracture condition has also led to a relation between the plane strain fracture toughness and the structural parameters (inclusions). Although the ductility turned out to depend only on volume fraction of inclusions, it appeared that fracture toughness depends both on volume fraction and spacing of inclusions. This shows that the fracture toughness can be improved by a greater ductility, but only if the particle distribution can be kept under control.

It has been mentioned previously that the engineering strength of materials is not controlled by fracture. The fracture event, however, sets a limitation to the ductility. The engineering strength is governed by the yield strength and the strain hardening exponent. Ductility depends on inclusion density, and so does fracture toughness. The investigation led to a more detailed picture of the fracture phenomenon. The information obtained about fracture surface topography can be of help for subsequent studies.

In the present work the volume of particles could be determined from transmission electron micrographs. In practice it would be valuable if this parameter could be derived from the chemical composition of an alloy. This may be a possibility for dispersion strengthened alloys, but for other materials it is impossible to estimate the amount of alloying elements dissolved in the matrix or present in small particles. Thus, an important question emerging from this discussion is how to determine the volume fraction of particles. Also, the nature and composition of the particles is of interest. It seems that this opens a field of study for the chemical analysis of small particles by means of X-ray spectrometry in the electron microscope. A start has been made already for Al–Zn–Mg alloys by Thackery [72] and for Al–Mg–Si alloys by Herker and Schaaber [73]. Further, it would be a great challenge to metallurgists to develop heat treatments which control the inclusion distribution and volume fraction without altering the required precipitates effect on yield strength and strain hardening. This task would be facilitated if the nature and morphology of the particles were known.

CHAPTER 10

APPENDIX: EXPERIMENTAL TECHNIQUES AND CALCULATION METHODS

Order of discussion

10.1 Replicas.
10.2 Cross sections of replicas and interpretation of results.
10.3 Matching surfaces.
10.4 Thin foils for transmission electron microscopy.
10.5 Tensile specimens for straining in the electron microscope.
10.6 Tensile specimens for testing under the optical microscope.
10.7 Tensile specimens with randomly distributed holes.
10.8 Stereoscopic measuring technique.
10.9 Determination of dimple size, particle distance and volume fraction.
10.10 Soap bubble rafts.

10.1 *Replicas.*

The replicas were two-stage carbon replicas. The first stage involved the preparation of a two-component plastic replica of substantial thickness so as to have sufficient strength and stiffness. In the second stage the plastic was shadowed with palladium or 80–20% platinum-palladium over which a 500–1000 Ångstrøm thick carbon film was deposited. The plastic replica was dissolved in acetone.

10.2 *Cross sections of replicas and interpretation of results.*

First stage plastic replicas, described in sect. 10.1, were provided with a carbon film on which a layer of two-component plastic was deposited, such that the carbon replica was sandwiched between two layers of plastic. The resulting sandwich was placed in an empty gelatine capsule, which was then filled with plastic. After hardening of the plastic the gelatine was removed and the pellets so obtained were cut perpendicular to the carbon layer by means of an ultra-microtome. Slices of 600 Ångstrøms thick were retained on a normal 200 mesh grid and were then ready for observation with the electron microscope. This method is described in ref. (10).

In order to determine the average dimple size from the cross sections, the following analysis has been applied. The dimple, with an average surface area $\bar{A}$, has an irregular form as in fig. 55a. When a cut is made through the dimple, the traverse length y (visible in the cross section) is

$$\text{Probability}\ \{\text{traverse length} = y\} = \frac{\mathrm{d}x}{\bar{c}}\,. \tag{67}$$

The average traverse length d^* as measured on the micrographs is given by

$$d^* = \int_0^{\bar{c}} y\,\frac{\mathrm{d}x}{\bar{c}} = \frac{A}{\bar{c}} = \frac{\alpha d^2}{\beta d} \tag{68}$$

where d is the characteristic length dimension of the dimple.

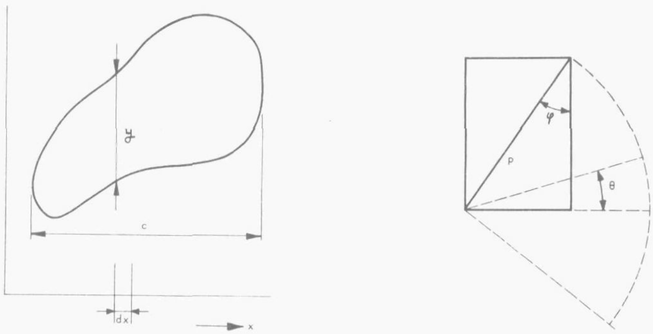

(a) Irregular dimple. (b) Rectangular dimple.

Fig. 55. Cross section of dimple.

From eq. (68),

$$d = \frac{\beta d^*}{\alpha} \quad \text{and} \quad \bar{A} = \alpha d^2 = \frac{\beta^2}{\alpha}\, d^{*2}\,. \tag{69}$$

If the voids are circles, $\bar{c} = d$ and $A = \frac{1}{4}\pi d^2$; hence $\beta = 1$ and $\alpha = \frac{1}{4}\pi$. Then the average dimple area can be determined from

$$\bar{A} = \frac{4}{\pi}\, d^{*2} \quad \text{and} \quad d^* = \frac{\pi}{4}\, \bar{d}\,. \tag{70}$$

Fullman [26] has also derived eq. (70), but by considering only the specific case of circular elements. The present more general treatment, however, allows the evaluation of other cases as well. For the case of rectangles (fig. 55b)

$$A = \alpha p^2 = p^2 \sin\varphi \cos\varphi \quad \text{or} \quad \alpha = \sin\varphi \cos\varphi\,. \tag{71}$$

Further, the mean projected length $\bar{c}$ of the rectangle is $\bar{c} = \beta d$, with

$$\beta = \int_{-\varphi}^{\frac{1}{2}\pi-\varphi} \cos\theta \frac{d\theta}{2/\pi} = \frac{2}{\pi}(\cos\varphi + \sin\varphi)\,. \tag{72}$$

Hence

$$\bar{A} = \frac{4}{\pi^2} d^{*2}\left(2 + \frac{2}{2\sin 2\varphi}\right). \tag{73}$$

For the special case of squares ($\varphi = 45°$)

$$\bar{A} = \frac{16}{\pi^2} d^{*2} = d^2 \quad \text{and} \quad d^* = \frac{4}{\pi}\bar{d}\,. \tag{74}$$

Eq. (74) apparently gives an upper limit of $16/\pi^2 \simeq 1.6$ for the coefficient, since according to eq. (73) it will always be smaller than 1.6 if $\varphi < 45°$. For the case of circles the coefficient is $4/\pi$, but circles are a less realistic case, since they cannot cover an area completely.

When considering the depth of the dimples, however, the most reasonable assumption is that the dimples are hemispheres. Then the previously given treatment for the circles holds, and hence

$$p^* = \frac{\pi}{4} p \tag{75}$$

where p is the dimple depth and p^* the apparent depth in the section. Combination of eq. (75) with (70) leads to the triviality:

$$\frac{q^*}{d^*} = \frac{q}{d}\,. \tag{76}$$

This means that the average depth to width ratio in the cross section is roughly equal to the real average depth to width ratio of the dimples; this relationship is thought to hold approximately for irregularly shaped dimples.

10.3 *Matching surfaces*

Obtaining micrographs of precisely matching areas of two opposing and mating fracture surfaces is a difficult task; it can be appreciated from fig. 47 that only a serious study of a pair of micrographs will reveal them to match. After some unsuccessful attempts to find the matching part of a micrograph in replicas of the mating fracture surface, it was decided that some landmark on the two fracture surfaces was required to find a matching place. Landmarks applied after fracture (e.g. by a scratch or a micro-hardness indenter) are not satisfactory, because they cannot be placed accurately enough on both surfaces. Hence, the landmark should be provided by the fracture process itself. This was accomplished in the following way.

A fatigue crack was grown to a predetermined length in a sheet specimen. A low stress amplitude was applied to keep the crack propagation rate low enough to ensure fatigue crack growth by striation formation: in a later, more rapid stage many dimples are formed during fatigue crack growth, as discussed earlier [74]. Then the specimen was fractured in a tensile machine. The transition from fatigue striations to dimples was the required matching landmark on both fracture surfaces.

Five replicas were made of the matching fracture surfaces and it was ensured that each replica contained the transition from fatigue to static fracture. This transition could easily be found in the electron microscope. The replicas were placed on grids with wide openings and in all ten replicas every part of the transition line (length 2 mm, since the specimen was 2 mm thick) not hidden by the grid was photographed at low magnification. This procedure guaranteed a high probability of having recorded the whole transition line. Careful comparison of the 150 micrographs so obtained finally revealed one set in which certainty of matching existed. The areas could be found again in the replicas concerned, and they were extensively photographed at higher magnification and various tilt angles, since tilting may be of great help in revealing hidden details, as discussed earlier [55].

10.4 *Thin foils for electron microscopy.*

In order to avoid the introduction of any additional deformation producing dislocations or eventually voids or broken inclusions, all necessary cutting was performed by spark machining under kerosene. By using a copper tube as a cutting tool a cylinder of 3 mm diameter was spark-cut from the sheet. With a tungsten wire the cylinder was cut into slices of about 0.4 mm thickness. By means of a steel pin with a hemispherical end, cusps were machined in both flat surfaces of these slices, leaving a rim of 0.4 mm thickness around an area of about 0.2 mm thickness.

Further thinning until penetration was performed by electropolishing at a current density of 0.5 mA/mm^2 in a solution of 20% perchloric acid in ethyl alcohol, which was kept at 0° C. For the aluminium–copper alloys an additional treatment was required. After penetration the specimen was electropolished for a few seconds at 15 Volts in a mixture of 15.6 grams chromic oxide, 72 cc phosphoric acid, 13.4 cc sulphuric acid and 14 cc distilled water, the mixture being kept at 70° C. Finally the specimen was rinsed in a solution of 100 grams chromic oxide and 175 cc phosphoric acid in 420 cc distilled water.

During electropolishing, the rims of the specimens were protected with lacquer; hence the final specimens were safely surrounded by a stiff ring, which facilitated handling and prevented deformations.

10.5 *Tensile specimens for straining in the electron microscope.*

These specimens were made by spark machining to fit the straining stage of the Philips EM-300 electron microscope. They had a thickness of 0.3 mm. Cusps were spark-machined in the middle of both surfaces and thinning until penetration completed by electropolishing (see sect. 10.4).

Straining was activated electrically and cracking could be followed if it took place (it seldom occurred) in the area under observation. Later the crack could also be followed in the part that originally did not transmit the electron beam, because necking was so severe that the specimen thinned sufficiently to allow electron transmission in a limited area at either side of the crack.

10.6 *Tensile specimens for testing under the optical microscope.*

The sheet material used was ground to a thickness of 0.5 mm. The specimens had a width of 3 mm (in the prismatic part) and a length of 25 mm. The specimen was finally ground on wet 600 grit paper and mechanically polished with 3, 1 and $\frac{1}{4}$ micron diamond paste successively. Then the specimens were provided with two fine scribe lines at 100 microns distance, made with the Knoop diamond on a Vickers-microhardness tester. The elongation of this 100 mm gauge length could easily be measured under the optical microscope at 200 ×. After predetermined increments of strain, micrographs were made of the same area, so that cracking of inclusions and void formation could be followed from successive micrographs.

The tensile tester consisted of a screw driven head, activated by hand via a worm drive of ratio 60 : 1. The whole device fitted with a dovetail on the cross-feed table of the optical microscope.

10.7 *Tensile specimens with randomly distributed holes.*

The specimens were made of brass sheet of 1 mm thickness; the gauge length was 50 mm, the width of the prismatic part 20 mm. They were provided with randomly distributed holes of various sizes to simulate a material containing voids. Brass sheet was chosen, because it was originally planned to fill the holes with steel balls, the ratio between the moduli of steel and brass is of the order of 2, a value which is probably reasonable for inclusions in aluminium alloys. The idea of steel balls was discarded later, because there appeared to be no satisfactory method to provide a proper bond between the balls and the specimen. All specimens were stress relieved for 30 minutes at 250°C after drilling of the holes.

The largest number of holes drilled in one specimen was 50. The gauge length of 50 mm of the specimen was divided into 50 horizontal bands of 1 mm width and 20 mm length (=specimen width). It was decided to stipulate that in the case of 50 holes each horizontal band contained 1 hole. In order to obtain a reasonably random distribution of the holes 20 positions on each band were chosen (1 position is $1 \times 1\ \mathrm{mm}^2$), and the position of the hole in each band was chosen at random from the 20 positions available. The distribution of holes so obtained was the basic distribution and it was kept the same for specimens with different hole diameters. It was kept the same also for specimens containing fewer holes, except that in every second or third horizontal band the hole was omitted.

In an area of 50×20 mm there are $N_a/1000$ holes of diameter a per unit area. Hence the (volume) fraction of holes is given by

$$f = \frac{\pi a^2 N_a}{4.1000} \quad \text{or} \quad N_a = \frac{4000f}{\pi a^2}. \tag{77}$$

The volume of material containing just one hole is given by $V = 1/N_a$. The average centre-to-centre particle spacing is given by $s \simeq \sqrt{V}$; hence, with eq. (77)

$$s^2 = \frac{4}{\pi}\frac{a^2}{f} \quad \text{and} \quad \frac{s^2}{a^2} = \frac{4}{\pi}\frac{1}{f}. \tag{78}$$

10.8 *Stereoscopic measuring technique.*

The technique and possible errors in the measurement of height differences in microscope samples by stereo photography has been extensively described by Garrod and Nankivell [75], Wells [76] and Nankivell [77, 78]. The discussion here will be limited to specialities that were introduced.

From fig. 6 it appears that in stereo pictures taken at tilt angles $\pm\theta$ the points A and B are imaged in A′, B′ and A″, B″ respectively, provided the microscope is long enough for the beams to be considered parallel. The lengths A′B′ and A″B″ can be measured from the stereo pair. The difference $A'B' - A''B'' = p$ is called the parallax and can be measured directly with a parallax bar. According to fig. 56a

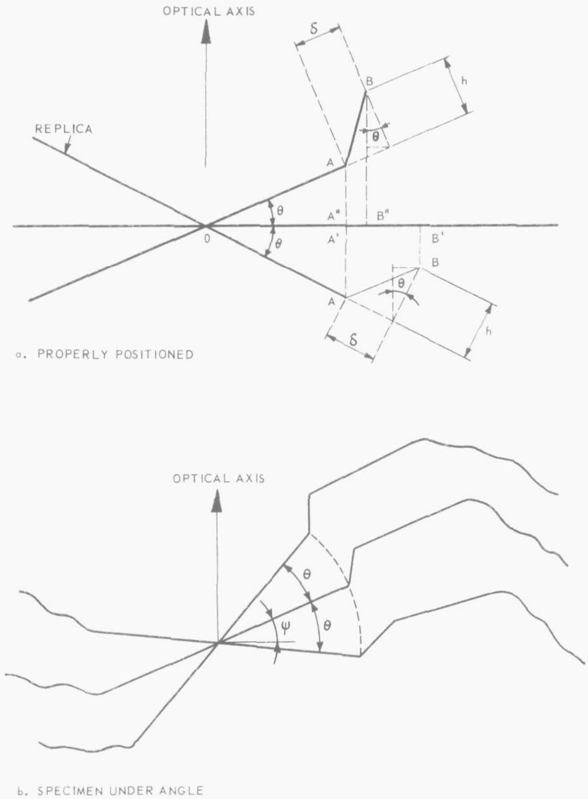

Fig. 56. Stereoscopic pictures.

$$A'B' - A''B'' = p = \delta \cos \theta + h \sin \theta - (\delta \cos \theta - h \sin \theta)$$

or

$$h = p/(2 \sin \theta) \,. \tag{79}$$

Hence the height difference on the scale of the micrograph is found directly from the measured parallax. The actual height difference is

$$h = p/(2M \sin \theta) \tag{80}$$

where M is the magnification.

If the tilt axis does not exactly intersect the optical axis of the microscope (fig. 56a) a tilt error is introduced. In the Philips EM 300 electron microscope the tilt axis can be adjusted very accurately to the optical axis, so the tilt error can be neglected. Because AB is closer to the objective lens at $-\theta$ than at $+\theta$, there is also a perspective error. Correction factors

If a line is passed through the cube the number N_l of particles intersected will be N_v times the probability that the line cuts a single particle. Since only $(\frac{1}{4}\pi a^2 : 1)$ positions would lead to an intersection,

$$N_l = N_v \cdot p = N_v \cdot \frac{\pi}{4} a^2 . \tag{87}$$

Eqs (86) and (87) are given by Fullman [26]. They can be treated to give all required quantities.

Combination of eqs (86) and (87) leads to:

$$a = \frac{4}{\pi} \frac{N_l}{N_a} . \tag{88}$$

Hence, the average particle size can be obtained from counts only; namely the number of particles per unit area and the number of particles per unit length of traverse.

If eq. (86) is squared and combined with (87),

$$N_v = \frac{\pi}{4} \frac{N_a^2}{N_l} \tag{89}$$

which means that the counts previously made also lead to the number of particles per unit volume. The volume fraction f is given by eq. (84). Substitution of eqs (88) and (89) in eq. (84) yields

$$f = \frac{8}{3\pi} \frac{N_l^2}{N_a} \tag{90}$$

which gives f, again from the same counts.

Eq. (85) gives in combination with eqs (88) and (90)

$$s^3 = \frac{4}{\pi} \frac{N_l}{N_a^2} \tag{91}$$

which finally gives the interparticle spacing s from the same counts of N_l and N_a that gave f.

When a thin foil specimen is examined in the electron microscope all particles in the foil are visible and not only those emanating at the surface. Consider again the unit cell with N_v particles. A foil of unit length and width and of thickness δ will contain δN_v particles. Hence, when looking through these foils one determines an apparent N_a which equals

$$N_a = \delta N_v . \tag{92}$$

When on the electron micrograph of the foil a straight line of unit length is drawn it will intersect a particular particle in $(a:1)$ positions, hence

$$N_l = aN_a = a\delta N_v \,. \tag{93}$$

Then it follows that

$$a = \frac{N_l}{\delta N_v} = \frac{N_l}{N_a} \tag{94}$$

and

$$f = \frac{\pi}{6} a^3 N_v = \frac{\pi}{6\delta} \frac{N_l^3}{N_a^2} \tag{95}$$

and

$$s^3 = \frac{\pi}{6} \frac{a^3}{f} = \frac{\delta}{N_a} \,. \tag{96}$$

For the case that $\delta \simeq a$, these equations become

$$a = \frac{N_l}{N_a}, \quad f = \frac{\pi}{6} \frac{N_l^2}{N_a} \quad \text{and} \quad s^3 = \frac{N_l}{N_a^2} \tag{97}$$

which can be compared with the equations for the cross sections.

In order to apply eqs (94), (95) and (96) the foil thickness δ has to be known for all places that have been photographed. This is not feasible and therefore δ was assumed to be 1000 Ångstrøms as an average. This approximation is not considered a serious limitation, since the results will only be used to give a rough appraisal of the trends.

Other shortcomings, of a physical nature, set more serious limitations to the validity of the data, as has been discussed in chapter 6.

10.10 *Soap bubble rafts.*

The two-dimensional bubble raft was prepared according to the method developed by Bragg and Nye [36]. A square of brass sheet with hinges at the corners was placed in the model. Two diagonally opposite corners of the square were pulled away from each other, thus deforming the square into a diamond. Voids were initiated along the other diagonal by breaking some bubbles with a hot piece of metal. The raft was filmed during deformation.

REFERENCES

[1] McClean, D., Mechanical properties of metals, p. 224. John Wiley, New York, 1962.

[2] Low, J. R., Effects of microstructure on fracture toughness of high strength alloys, Engineering Fracture Mechanics 1, 1968, pp. 47–53.

[3] Rosenfield, A. R., Criteria for ductile fracture of two-phase alloys, Metals and Materials and Metallurgical Review, April 1968, pp. 29–40.

[4] Puttick, K. E., Ductile fracture in metals, Philosophical Magazine 4 (1959), pp. 964–969.

[5] Rogers, H. C., The tensile fracture of ductile metals, AIME trans. 218, June 1960, pp. 498–506.

[6] Crussard, C. *et al.*, Fracture (edited by B. L. Averbach *et al.*), p. 524, John Wiley, New York, 1959.

[7] Palmer, G. and Smith, G. C., Some aspects of ductile fracture in metals. Physical bases of yield and fracture, pp. 53–59. Inst. of Phys. 8 Phys. Soc. Conf. series 1, Oxford, 1966.

[8] Olsen, R. J., The strength differential in two phase alloys, ASM Trans. Quarterly, 62, 1969 pp. 711–719.

[9] Ruedl, E., Void formation at the interface between particles and matrix in deformed $Al–Al_2O_3$ foils, Journal of Materials Science 4 (1969) pp. 814, 815.

[10] Broek, D. and Bowles, C. Q., The study of fracture surface profiles in the electron microscope. Int. J. Fract. Mech., 6 (1970) pp. 321–322.

[11] Goodier, J. N., Concentration of stress around spherical and cilindrical inclusions and flaws, Journal Applied Mechanics 1, 2 (1933) pp. 39–44.

[12] Gurland, J. and Plateau, J., The mechanism of ductile rupture of metals containing inclusions, Trans. ASM 56 (1963) pp. 442–454.

[13] Ashby, M. F., Work hardening of dispersion-hardened crystals, Philosophical Magazine 14 (1966) pp. 1157–1178.

[14] Barnes, R. S. and Mazey, D. J., Stress-generated prismatic dislocation loops in quenched copper, Acta Metallurgica 11, 4 (April 1963) pp. 281–286.

[15] Hirsch, P. B., The interpretation of the slip pattern in terms of dislocation movements, Journal Institute of Metals 86 (1957) pp. 13–14.

[16] Ashby, M. F. The hardening of metals by non-deforming particles. Zeitschrift für Metallkunde, 55 (1964) pp. 5–17.

[17] Gleiter, H., Theorie der prismatischen Quergleitung von Versetzungen in der Umgebung von Ausscheidungen, Acta Metallurgica 15 (1967) pp. 1213–1228.

[18] Gurland, J., The fracture strength of sintered WC–Co alloys in relation to composition and particle spacing, AIME trans. 227 (Oct. 1963) pp. 1146–1150.

[19] Barnby, J. T., The initiation of ductile failure by fractured carbides in an austenitic stainless steel, Acta Metallurgica, 15, 5 (May 1967) pp. 903–909.

[20] Chao, H. C. and van Vlack, L. H., Fracturing of oriented MnS inclusions in steel, ASM trans. 58, 1965, pp. 335–340.

[21] Oates, G. and Griffith, J. R., Mechanisms of cleavage-fracture initiation in notched and smooth specimens of 3 % silicon iron, Metal Science Journal 3 (1969) pp. 111–115.

[22] Bucher, J. H., The effect of inclusions on the brittle fracture of hot rolled steel, Journal of Materials 2, 2 (June 1967) pp. 432–444.

[23] Wood, L. E. and van Vlack, L. H., Fracture and deformation of sulfide inclusions in steel, ASM trans. 56 (1963) pp. 770–772.

[24] Östberg, G., Crack propagation in hydrided zircaloy, Int. Journal of Fracture Mechanics 4, 2 (June 1968) pp. 95–98.
[25] Koreida, A. and Shimizu, K., Dislocations in cementite, Philosophical Magazine (1968) pp. 1083–1086.
[26] Fullman, R. L., Measurement of particle sizes in opaque bodies, Journal of Metals 5 (1953) pp. 447–452.
[27] Thomason, P. F., A theory for ductile fracture by internal necking of cavities, Journal Inst. of Metals 96 (1968) pp. 360–365.
[28] McClintock, F. A., *et al.*, Ductile fracture by hole growth in shear bands. Int. Journal of Fracture Mechanics 2 (1966) pp. 614–627.
[29] Rosenfield, A. R. and Hahn, G. T., Numerical descriptions of the ambient low-temperature and high strain rate flow and fracture behaviour of plane carbon steel. ASM Trans. 59 (1966) pp. 962–980.
[30] Rice, J. R. and Tracey, D. M., On the ductile enlargement of voids in triaxial stress fields. Journal Mech. Phys. Solids 17, 3 (June 1969) pp. 201–217.
[31] Bluhm, J. E. and Morressey, R. J., Fracture in a tensile specimen, Proc. 1st ICF Conf. Sendai, Japan, 1966, pp. 1739–1781.
[32] Clausing, D. P., The development of fibrous fracture in a mild steel. ASM Trans. Quart. 60, 1967, pp. 504–515.
[33] Broek, D. and Bowles, C. Q., The effect of cold deformation between quenching and ageing on static and dynamic crack propagation in an Al–Cu alloy. NLR Report TR 69048, July 1969, To be published partly in J. Inst. Metals.
[34] Brindley, B. J. The mechanism of ductile fracture in a chromium steel, Acta Metallurgica 16, 4 (April 1968) pp. 587–595.
[35] Calhoun, C. D. and Stoloff, N. S., The effects of particles on fracture processes in magnesium alloys. Metallurgical Transactions 1, 1970, pp. 997–1006.
[36] Bragg, L. and Nye, J. F., A dynamical model of a crystal structure., Proc. Roy. Soc. A190 (1948), pp. 474–481.
[37] Broek, D., The effect of sheet thickness on the fracture toughness of cracked sheet, NLR Techn. Report M.2160, 1966.
[38] Friedel, J., Dislocations, Pergamon-Addison Wesley, 1964.
[39] Barett, D. M. and Tetelman, A. S., The stress distribution produced by screw dislocation pile ups at rigid circular cylindrical inclusions, J. Mech. Phys. Solids 14, 6 (1966) pp. 329–348.
[40] Smith, E., The piling up of screw dislocations against a circular cylindrical rigid inclusion, J. Mech. Phys. Solids 16 (1968) pp. 163–167.
[41] Dundurs, J. and Mura, T., Interaction between an edge dislocation and a circular inclusion, Journal Mech. Phys. Solids 12 (1964) pp. 177–178.
[42] Dundurs, J. and Gangadharan, A. C., Edge dislocations near an inclusion with a slipping interface, J. Mech. Phys. Solids 17 (1969) pp. 459–471.
[43] Weeks, R. W. *et al.*, The elastic interaction between a straight dislocation and a bubble or a particle, Acta Metallurgica 17 (1969) pp. 1403–1410.
[44] Head, A. K., The interaction of dislocations and boundaries, Phil. Mag. (1953) pp. 92–94.
[45] Chou, Y. T., Linear dislocation arrays in heterogeneous materials, Acta Metallurgica 13 (1965) pp. 779–783.
[46] Barnett, D. M., The effect of shear modulus on the stress distribution produced by a planar array of screw dislocations near a bimetallic interface, Acta Metallurgica 15 (1967) pp. 589–594.

[47] Leibfried, G., Versetzungsverteilung in kleinen plastisch verformten Bereichen, Zeitschrift für Angew. Physik 6 (1954) pp. 251–252.

[48] Edelson, B. I. and Baldwin, W. M., The effect of second phases on the mechanical properties of alloys, ASM Trans. 55 (1962) pp. 230–250.

[49] Orowan, E., Symposium on internal stresses, p. 451, Inst. of Metals, London, 1947.

[50] Schiller, P. and Schneiders, A., On the ductility of SAP alloys, Journal of Nuclear Materials 27 (1968) pp. 115–117.

[51] Birkle, A. J. *et al.*, Analysis of plane-strain fracture in a series of low alloy steels with different sulfur contents, ASM Trans. 59, 4 (Dec. 1966) p. 951.

[52] Keeler, J. H., The tensile characteristics of unalloyed zirconium at low and moderate temperatures, ASM Trans. 47 (1955) pp. 147–191.

[53] Keeler, J. H., Tensile properties of Zr–Cr alloys, ASM Trans. 48 (1956) pp. 825–842.

[54] Beachem, C. D., Electron fractographic studies of mechanical fracture processes in metals. ASTM Trans. 87 D, 2, 1965.

[55] Broek, D., A critical note on electron fractography, Eng. Fracture Mechanics 1, 4, (1969), Philips Bulletin 79, 177/EM 39.

[56] Rosenfield, A. R. and Hahn, G. T., Sources of fracture toughness. Presented at the ASTM Symposium on titanium, Los Angeles April 1967.

[57] Krafft, J. M., Correlation of plane strain crack toughness with strain hardening characteristics of steels, Applied Materials Research 3, 1964, pp. 88–101.

[58] Krafft, J. M., Dynamic mechanical behavior of metal at the tip of a plane strain crack. Presented at S. W. Institute Symposium on dynamic loading, San Antonio, Sept. 1967.

[59] Williams, J. G. and Turner, C. E., The plastic instability viewpoint of crack propagation, Applied Materials Research 3, 1963, pp. 144–147.

[60] Malkin, J. and Tetelman, A. S., Relation between K_{Ic} and microscopic strength for low alloy steels, Defense Documentation Center, U.S. Dept. of Defense DAH-04-68-C-008, TR 1, Report 69-58 (1969).

[61] Dugdale, D. S., Yielding of steel sheets containing slits, Journal Mechanics Physics Solids 8, 1960, p. 100.

[62] Broek, D., The residual strength of cracked sheet and structures, Aerospace Proceedings 1966, pp. 811–831, McMillan 1967.

[63] Broek, D., The effect of finite specimen width on the residual strength of light alloy sheet, NLR Tech. Report M.2152, Sept. 1965.

[64] Tamate, O., The effect of a circular inclusion on the stresses around a line crack in a sheet under tension. Int. Journal Fracture Mechanics 4, 3 (1968) pp. 257–265.

[65] Schijve, J., Analysis of the fatigue phenomenon in aluminium alloys, NLR Report M.2122 (1964).

[66] Broek, D., Some considerations on slow crack growth, Int. Journal Fracture Mechanics 4, 1 (1968) pp. 19–34.

[67] Spitzig, W. A., A fractographic feature of plane strain fracture, ASM Trans. Quarterly 61, 1968, pp. 344–349.

[68] Gerberich, W. W. and Hemmings, P. L., Fractographic observations of stretched regions in front of fatigue cracks, ASM Trans. Quarterly 62, 1969, pp. 540–543.

[69] Griffis, G. A. and Spretnak, J. W., A suggestion on the nature of the plastic stretch zone. Metallurgical Trans. 1 (1970) pp. 550–551.

[70] Kanazawa, T. *et al.*, A study of the crack opening displacement for brittle fracture initiation, Fracture 1969, pp. 1–14, Chapman and Hall, London 1969.

[71] Arthur, P. F. and Blackburn, W. S., The effect of the shape of the plastic zone on

plastic zone size and crack opening displacement. Fracture 1969, pp. 15–23, Chapman and Hall, London 1969.

[72] Thackery, P. A., The nature and morphology of precipitate in Al–Zn–Mg alloys, Journal Institute of Metals 96, 1968, pp. 228–235.

[73] Herker, D. and Schaaber, O., Elektronenstrahlmikroanalysator Untersuchungen – Veränderung der Einschlüsse im Gussmaterial durch Wärmebehandlung, Härterei-Techn. Mitt. 24 (1969) pp. 92–99.

[74] Broek, D., The effect of intermetallic particles on fatigue crack propagation in aluminium alloys, Fracture 1969, pp. 754–764, McMillan, London, 1969.

[75] Garrod, R. I. and Nankivell, J. F., Sources of error in electron stereo-micrography, British Journal Applied Physics 9 (1958), pp. 214–218.

[76] Wells, O. C., Correction of errors in electron stereomicroscopy, British Journal Applied Physics 11 (1960) pp. 199–201.

[77] Nankivell, J. F., Minimum differences in height detectable in electron stereomicroscopy, British Journal Applied Physics 13 (1962) pp. 126–128.

[78] Nankivell, J. F., Stereoscopic viewing of metal foils in the electron microscope, British Journal Applied Physics 13 (1962) pp. 129–130.

SAMENVATTING IN HET NEDERLANDS

Het verschijnsel van de taaie statische breuk heeft in het verleden weinig aandacht gekregen, in tegenstelling tot onderwerpen als plastische deformatie, vermoeiing, brosse breuk en precipitatie. Een herleving van de belangstelling voor de taaie breuk gedurende het laatste decennium werd geïnstigeerd door de opkomst van het 'fracture toughness' onderzoek.

De bestaande voorstelling over de toedracht van de statische breuk hield in

a) het ontstaan van kleine holten bij insluitsels en tweede-fase deeltjes;
b) de samengroei van deze holten, waarmee de breuk zich voltrekt.

Dit fenomenologische model berustte op

- waarneming door middel van optische microscopie van holten in doorsneden van het ingesnoerde deel van trekproefstukken.
- elektronen-microscopisch onderzoek van breukvlakken, waarbij bleek dat het breukvlak bestaat uit kleine kuiltjes waarin veelal een klein tweede-fase deeltje zichtbaar is; deze kuiltjes worden beschouwd als de helften van aaneengegroeide holten.

De holten zichtbaar met het optisch-microscoop verschillen enkele orden van grootte met de kuiltjes waargenomen met het elektronen-microscoop. Uit de literatuur blijkt dat weliswaar kleinere holten zijn waargenomen bij elektronen-transmissie onderzoek van dispersie-geharde materialen maar niet in andere constructiematerialen.

Het hier beschreven onderzoek beoogde meer informatie te verzamelen over het breukgedrag van aluminium-legeringen en te bepalen door welke parameters de taaie breuk wordt beheerst. De structuur en de breukvlakken van trekproefstukken van dertien verschillende aluminium legeringen werden onderzocht met behulp van het elektronen-microscoop.

Aangetoond kon worden dat de gemiddelde grootte van de kuiltjes in de breukvlakken nagenoeg overeen kwam met de gemiddelde afstand van kleine tweede-fase deeltjes, ter grootte van enkele tienden van microns. Dit geldt voor alle onderzochte materialen. Op deze indirecte wijze kon worden vastgesteld welke soort deeltjes verantwoordelijk is voor de holtevorming. Een directe waarneming van deze holtes bleek mogelijk bij transmissie-onderzoek van sterk gedeformeerd materiaal; de holtevorming kon evenwel slechts incidenteel worden aangetoond. Trekproeven uitgevoerd onder het optisch microscoop leerden dat grote deeltjes (5 micron en groter) reeds breken bij rekken in de orde van 3 tot 10%.

De proefresultaten leiden tot de conclusie dat breuk optreedt zodra holtes ontstaan bij kleine deeltjes. De breuk bij lage rek van grote insluitsels introduceert weliswaar een rekconcentratie en kan daardoor de macroscopische breukrek van het materiaal beïnvloeden, maar deze gebroken insluitsels zijn op zichzelf niet essentieel voor de uiteindelijke taaie breuk. Volgens de literatuur kunnen in dispersiegeharde materialen de micro-holten blijkbaar al in een vroeg stadium ontstaan en geleidelijk aaneengroeien. In de onderzochte aluminiumlegeringen bestaat evenwel een sterke binding tussen de tweede-fase deeltjes en de matrix, waardoor een hoge rek is vereist voor de holtevorming. Zodra de holten eenmaal ontstaan, is ook meteen voldaan aan de condities voor hun groei: het ontstaan van holten is hier kritiek.

Een dislocatie-model werd ontwikkeld dat deze vorm van statische breuk kan verklaren. Tijdens plastische deformatie worden dislocatieringen opgestapeld rond de deeltjes. De binnenste ringen worden door de werkzame schuifspanning en door de buitenste dislocaties naar het scheidingsvlak geduwd. Indien enkele ringen tot in het scheidingsvlak doordringen, kan dit aanleiding geven tot decohesie. Als op deze wijze een holte is gevormd kunnen de achterliggende dislocaties in de holte glijden waardoor de holte groeit.

De uitwerking van een twee-dimensionale versie van het dislocatiemodel leidt tot een relatie tussen de breukrek en de volume-fractie der tweede-fase deeltjes. Met behulp van de gevonden relatie kan aannemelijk worden gemaakt dat de scheurweerstand K_{Ic} afhankelijk is, zowel van de volume-fractie als van de afstand van de beschouwde deeltjes.

De taaiheid van aluminiumlegeringen wordt blijkbaar beheerst door kleine tweede-fase deeltjes. Taaiheid en scheurweerstand kunnen derhalve worden verbeterd door de volume-fractie en afstand van de deeltjes op gunstige wijze te beïnvloeden. Hiertoe zullen speciale warmtebehandelingen en legeringtechnieken ontwikkeld moeten worden; dit kan eerst geschieden als karakter en samenstelling van de desbetreffende deeltjes zijn bepaald door middel van spectrometrische methoden.